Chapter 2
Propagation Modeling

The design of spectrally efficient wireless communication systems requires a thorough understanding of the radio propagation channel. The characteristics of the radio channel will vary greatly with the operating frequency, and the propagation environment, for example, line-of-sight (LoS) versus non-line-of-sight (NLoS), stationary versus mobile transmitters and receivers, and other factors. This chapter emphasizes land mobile radio channels, including those found in cellular land mobile radio systems and mobile ad hoc networks. However, many of the concepts are of a fundamental nature and will apply to other types of radio channels as well.

A typical cellular land mobile radio system consists of a collection of fixed base stations (BSs) that define radio coverage areas known as cells. The height and placement of the BS antennas affect the proximity of local scatterers at the BSs. In a macrocellular environment where the cell radii are large, the BS antennas are well elevated above the local terrain and are free of local scatterers. Mobile stations (MSs), on the other hand, tend to be surrounded by local scatterers due to their low elevation antennas. Sometimes an LoS condition will exist between a BS and an MS, for example in a rural (or open) environment. However, in an urban environment, an NLoS condition typically exists between the BSs and MSs. As a consequence, the radio waves must propagate between the BSs and MSs via reflections, diffraction, and scattering. Due to the typically large distance between the BSs and MSs in macrocellular systems, radio propagation is often assumed to occur in a two-dimensional (2D) plane. As shown in Fig. 2.1, multiple plane waves will arrive at the MS (or BS) receiver antenna(s) from different directions, with each having a distinct polarization, amplitude, phase, and delay. This phenomenon is called multipath propagation. The multiple plane waves combine vectorially at each MS (or BS) receiver antenna to produce a composite received signal.

Commercial cellular land mobile radio systems operate at UHF frequencies in bands located at 700/800/900 MHz and 1,800/1,900 MHz. At these frequencies, the carrier wavelength, λ_c, is approximately 15 cm and 30 cm, respectively, using the relationship $c = f_c \lambda_c$, where f_c is the carrier frequency and c is the speed of light. Therefore, small changes in the propagation delays of the individual multipath components due to MS mobility on the order of a few centimeters will cause a large
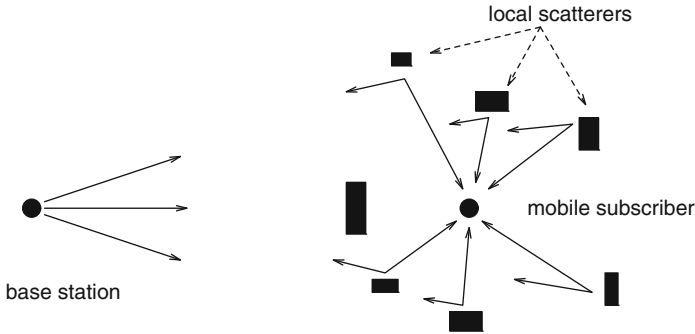
43

Fig. 2.1 Typical macrocellular radio propagation environment

change in the relative phases of the plane wave components arriving at the MS (or BS) receiver antennas. Hence, when the arriving plane waves combine vectorially at the receiver antenna(s), they will experience constructive and destructive addition depending on the physical location of the MS. If the MS is moving or there are changes in the location of the scatterers, then these spatial variations will manifest themselves as time variations in the amplitude and phase of the composite signal received at each MS (or BS) antenna, a phenomenon known as envelope fading. If the propagation environment is such that no individual multipath component is dominant, such as when NLoS conditions exist between the BS and MS, then the composite received envelope under narrowband propagation conditions is often modeled as being Rayleigh distributed at any time. Such a channel is said to exhibit Rayleigh fading. However, if a dominant multipath component exists, such as when an LoS or specular condition exists between the BS and MS, then the envelope is often modeled as being Ricean distributed at any time. Such a channel is said to exhibit Ricean fading.

Radio channels are reciprocal in the sense that if a propagation path exists, it carries energy equally well in both directions. However, the spatial distribution of arriving plane waves may be significantly different in each direction. An MS in a typical NLoS macrocellular environment is usually surrounded by local scatterers, so that the plane waves will arrive at the MS antenna from many different directions, as shown in Fig. 2.1. Two-dimensional (2D) isotropic scattering, where the plane waves arrive from all azimuth directions with equal probability and with equal strength, is a very commonly used reference model to describe the signals received at an MS in this case. The BSs, on the other hand, are relatively free from local scatterers. Hence, plane waves tend to arrive at a BS with a small azimuth angle of arrival (AoA) spread as shown in Fig. 2.1. We will see later in this chapter that these differences in the scattering environment for the forward and reverse links will cause significant and important differences in the spatial correlation properties of the respective faded envelopes at the MSs and BSs.

Some types of land mobile radio systems, such as mobile ad hoc networks, consist of vehicle-to-vehicle (or mobile-to-mobile) and vehicle-to-infrastructure
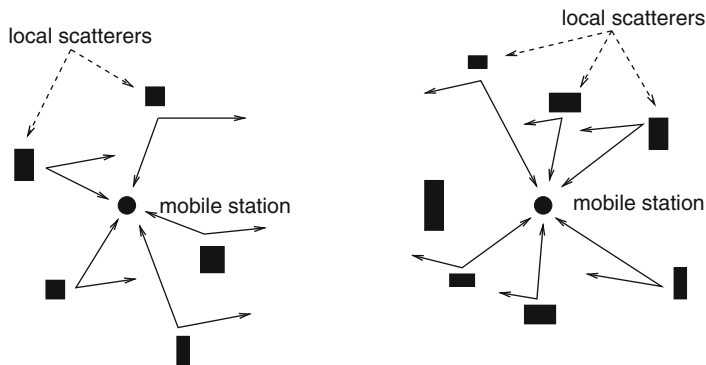
Fig. 2.2 Typical mobile-to-mobile radio propagation environment

links. In this book, we refer to vehicle-to-vehicle links as mobile-to-mobile links, because the user terminals are not necessarily vehicular mounted. A typical mobile-to-mobile radio propagation environment is depicted in Fig. 2.2. Such mobile-to-mobile communication systems differ from conventional cellular radio systems where one end of the link (the BS) is stationary and free of scattering, and only the MS is moving. Although the received signal envelope of mobile-to-mobile links is still Rayleigh faded under NLoS narrowband propagation conditions, the mobility of both the transmitters and receivers, and scattering at both ends of the links, causes these links to exhibit much different statistical properties than cellular land mobile radio channels.

If the received envelope or squared envelope is averaged over a spatial distance of 20–30 wavelengths, an estimated mean envelope or mean-squared envelope can be obtained. Sometimes, this quantity is called the local mean because it corresponds to a particular locality. The local mean will experience slow variations over distances of several tens of wavelengths due to the presence of large terrain features such as buildings, hills, and valleys. This phenomenon is known as shadow fading or shadowing. Experimental observations have confirmed that the local mean signal strength follows a log-normal distribution. This log-normal distribution applies to both macrocellular [134, 151] and microcellular environments [119, 179, 181].

If the local mean is averaged over a sufficiently large spatial distance (to average over the shadows), the area mean is obtained. The area mean is the average signal strength that is received to/from an MS over locations that lie at the same distance from the BS. The area mean is inversely proportional to the path loss, which describes how the area mean decreases with the distance between the BS and MS. Early studies by Okumura [197] and Hata [129] yielded an empirical path loss model for macrocellular radio systems operating in urban, suburban, and rural areas. The Okumura–Hata model is accurate to within 1 dB for distances ranging from 1 to 20 km and carrier frequencies between 150 and 1,000 MHz, and was adopted in the COST207 study [63]. The Okumura–Hata model is only valid for carrier frequencies less than 1,000 MHz. Consequently, when additional spectrum was made available

in the 1990s for cellular systems operating in the 1,800/1,900 MHz band, new path loss models were needed. The COST231 study [66] resulted in the COST231–Hata model that extended the Okumura–Hata model to the 1,800/1,900 MHz band, and provided the Walfish–Ikegami model for path loss prediction in LoS and NLoS urban microcells.

The remainder of this chapter presents the fundamentals of radio propagation modeling, analysis, and simulation. Section 2.1 considers conventional narrowband F-to-M channels, and various properties of the faded envelope are considered. Section 2.2 considers mobile-to-mobile channels. Section 2.3 considers multiple-input multiple-output (MIMO) channels that are created by having multiple antennas at both the transmitter and receiver. Section 2.4 treats the statistical characterization of wide-band multipath-fading channels. Simulation models for fading channels are covered in Sect. 2.5. Shadowing models and simulation techniques are discussed in Sect. 2.6. Finally, Sect. 2.7 treats theoretical and empirical models for path loss in macrocellular and microcellular systems.

2.1 Fixed-to-Mobile Channels

For land mobile radio applications, the signals from the BSs are usually transmitted with vertical polarization, meaning that the electric field is perpendicular to the Earth's surface. At VHF frequencies, vertical polarization produces a higher field strength close to the ground than horizontal polarization. Likewise, the MS antennas are also vertically polarized, although tilting of the MS antenna will result in a polarization mismatch. Even if the signals are transmitted with vertical polarization, reflections and diffractions from objects will cause the signals to undergo depolarization. This effect can be exploited using polarization diverse antennas. For example, cross-polarized antennas, where two antennas having $+45°$ and $-45°$ polarizations from vertical, are sometimes used at the BSs. Although it is important to account for polarization effects, we will assume in this chapter that the transmitted and received signals are vertically polarized.

In cellular land mobile radio systems, the radio signals will propagate in three dimensions. However, if the distance between the BS and MS is sufficiently large, the radio propagation environment is often modeled as occurring in a 2D plane. Figure 2.3 depicts a horizontal x–y plane, where an MS is moving in the direction of the positive x-axis with velocity v. The BS is assumed stationary. With vertical polarization, the electric field vector is aligned with the z-axis. The nth plane wave arrives at the MS antenna with an angle of incidence θ_n. The MS movement introduces a Doppler shift, or frequency shift, into the incident plane wave. The Doppler shift is given by

$$f_{\mathrm{D},n} = f_{\mathrm{m}} \cos(\theta_n) \text{ Hz}, \tag{2.1}$$

Fig. 2.3 A typical plane
wave incident on a MS
receiver
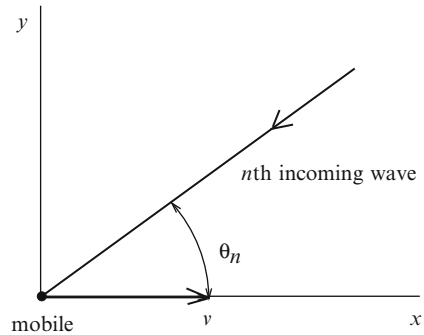
where $f_m = v/\lambda_c$ and λ_c is the wavelength of the arriving plane wave, and f_m is the maximum Doppler frequency occurring when $\theta_n = 0$. Plane waves arriving from the right half plane will experience a positive Doppler shift, while those arriving from the left half plane will experience a negative Doppler shift.

Consider the transmission of the band-pass signal

$$s(t) = \text{Re}\left\{\tilde{s}(t)e^{j2\pi f_c t}\right\}. \tag{2.2}$$

where $\tilde{s}(t)$ is the complex envelope of the band-pass signal, f_c is the carrier frequency, and $\text{Re}\{z\}$ denotes the real part of z. If the channel is comprised of N propagation paths, then the noiseless received band-pass waveform is

$$r(t) = \text{Re}\left\{\sum_{n=1}^{N} C_n e^{j\phi_n - j2\pi c\tau_n/\lambda_c + j2\pi(f_c + f_{D,n})t}\tilde{s}(t - \tau_n)\right\}, \tag{2.3}$$

where C_n, ϕ_n, $f_{D,n}$, and τ_n are the amplitude, phase, Doppler shift, and time delay, respectively, associated with the nth propagation path, and c is the speed of light. The magnitude C_n depends on the cross-sectional area of the nth reflecting surface or the length of the nth diffracting edge. The phase ϕ_n is randomly introduced by the nth scatterer and can be assumed to be uniformly distributed on $[-\pi, \pi)$. The delay $\tau_n = d_n/c$ is the propagation delay associated with the nth propagation path, where d_n is the length of the path. The path lengths, d_n, will depend on the physical scattering geometry which we have not specified at this point. The Doppler shift $f_{D,n}$ is as discussed previously.

Similar to (2.2), the received band-pass signal $r(t)$ has the form

$$r(t) = \text{Re}\left\{\tilde{r}(t)e^{j2\pi f_c t}\right\}, \tag{2.4}$$

where the received complex envelope is

$$\tilde{r}(t) = \sum_{n=1}^{N} C_n e^{j\phi_n(t)}\tilde{s}(t - \tau_n) \tag{2.5}$$

and

$$\phi_n(t) = \phi_n - 2\pi c\tau_n/\lambda_c + 2\pi f_{D,n}t \tag{2.6}$$

is the time-variant phase associated with the nth path. From (2.5) and the fact that $\tilde{r}(t) = g(t, \tau) * \tilde{s}(t)$ with $*$ denoting the operation of convolution, the channel can be modeled by a linear time-variant filter having the complex low-pass impulse response

$$g(t, \tau) = \sum_{n=1}^{N} C_n e^{j\phi_n(t)}\delta(\tau - \tau_n), \tag{2.7}$$

where $g(t, \tau)$ is the channel response at time t due to an impulse applied at time $t - \tau$, and $\delta(\cdot)$ is the Dirac delta function or unit impulse function.

From (2.5) and (2.6), several interesting observations can be made. Since the carrier wavelength λ_c is small (approximately 30 cm at 1 GHz), even small changes in the path delays $d_n = c\tau_n$ will cause large changes in the phases $\phi_n(t)$, due to the term $2\pi c\tau_n/\lambda_c = 2\pi d_n/\lambda_c$. Also, due to the Doppler frequency $f_{D,n}$, the phases $\phi_n(t)$ vary with time. Hence, at any given point in space–time, the phases $\phi_n(t)$ will result in the constructive or destructive addition of the N multipath components, a phenomenon known as fading.

If the differential path delays $\tau_i - \tau_j$ for all i, j are very small compared to the modulation symbol period, T, then the τ_n that appear in the argument of Dirac delta function in (2.7) can be approximated by their average value $\bar{\tau}$, that is, $\tau_n \approx \bar{\tau}$. In this case, the channel impulse response has the form

$$g(t, \tau) = g(t)\delta(\tau - \hat{\tau}), \tag{2.8}$$

where

$$g(t) = \sum_{n=1}^{N} C_n e^{j\phi_n(t)}. \tag{2.9}$$

It is important to note that $\phi_n(t)$ remains as defined with the τ_n in (2.6), since we *cannot* make the approximation $f_c\tau_n \approx f_c\bar{\tau}$ when f_c is large. Therefore, the received complex envelope is

$$\tilde{r}(t) = g(t)\tilde{s}(t - \hat{\tau}), \tag{2.10}$$

which experiences fading due to the time-varying complex channel gain $g(t)$. In the frequency-domain, the received complex envelope is

$$\tilde{R}(f) = G(f) * \left(\tilde{S}(f)e^{-j2\pi f\hat{\tau}}\right). \tag{2.11}$$

Since the channel changes with time, $G(f)$ has a finite nonzero width in the frequency-domain. Due to the convolution operation, the output spectrum $\tilde{R}(f)$ will be larger than the input spectrum $\tilde{S}(f)$. This broadening of the transmitted signal spectrum is caused by the channel time variations and is called frequency spreading.
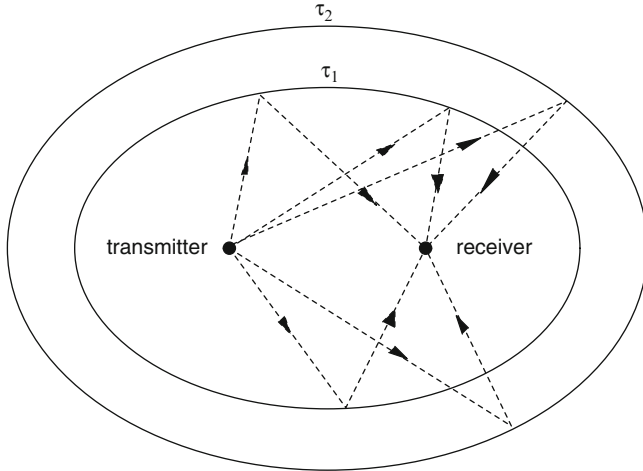
Fig. 2.4 Concentric ellipses model for frequency-selective fading channels

The time-variant channel transfer function can be obtained by taking the Fourier transform of (2.8) with respect to the τ variable, giving

$$T(f,t) = \mathscr{F}\{g(t,\tau)\} = g(t)\mathrm{e}^{-\mathrm{j}2\pi f \hat{\tau}}. \tag{2.12}$$

The time-variant channel magnitude response is $|T(f,t)| = |g(t)|$. Note that all frequency components in the received signal are scaled by the same time-variant magnitude $|g(t)|$. In this case, the received signal is said to exhibit frequency flat fading, because the magnitude of the time-variant channel transfer function is constant (or flat) with respect to frequency variable f.

If the differential path delays $\tau_i - \tau_j$ for some i, j are sufficiently large compared to the modulation symbol period T, then the magnitude response $|T(f,t)|$ is no longer flat and the channel exhibits frequency-selective fading. Sometimes frequency-selective fading channels are called wide-band channels. A simplified concentric-ellipses model for frequency-selective fading channels is depicted in Fig. 2.4, where the transmitter and receiver are located at the foci of the ellipses. Considering only single bounce reflections between the transmitter and receiver, all paths that are associated with scatterers on the nth elliptical contour will have the same propagation delay τ_n. Frequency-selective channels have strong scatterers that are located on several ellipses such that the corresponding differential path delays $\tau_i - \tau_j$ for some i, j are significant compared to the modulation symbol period T.

2.1.1 Envelope Correlation

A flat fading channel can be characterized by assuming the transmission of an unmodulated carrier, because the channel magnitude response is flat. Assuming

$\tilde{s}(t) = 1$ in (2.5), the received band-pass signal in (2.4) can be expressed in the quadrature form

$$r(t) = g_I(t)\cos(2\pi f_c t) - g_Q(t)\sin(2\pi f_c t), \tag{2.13}$$

where

$$g_I(t) = \sum_{n=1}^{N} C_n \cos(\phi_n(t)), \tag{2.14}$$

$$g_Q(t) = \sum_{n=1}^{N} C_n \sin(\phi_n(t)) \tag{2.15}$$

are the in-phase and quadrature components of the received band-pass signal. Assuming that the band-pass process $r(t)$ is wide-sense stationary (WSS), the autocorrelation function of $r(t)$ is

$$\phi_{rr}(\tau) = E[r(t)r(t+\tau)]$$

$$= \phi_{g_I g_I}(\tau)\cos(2\pi f_c \tau) - \phi_{g_I g_Q}(\tau)\sin(2\pi f_c \tau), \tag{2.16}$$

where $E[\,\cdot\,]$ is the ensemble average operator, and

$$\phi_{g_I g_I}(\tau) \triangleq E[g_I(t)g_I(t+\tau)], \tag{2.17}$$

$$\phi_{g_I g_Q}(\tau) \triangleq E[g_I(t)g_Q(t+\tau)]. \tag{2.18}$$

Note that the wide-sense stationarity of $r(t)$ imposes the condition

$$\phi_{g_I g_I}(\tau) = \phi_{g_Q g_Q}(\tau), \tag{2.19}$$

$$\phi_{g_I g_Q}(\tau) = -\phi_{g_Q g_I}(\tau). \tag{2.20}$$

We now proceed to evaluate the expectations in (2.17) and (2.18).

It is safe to assume that the phases $\phi_n(t)$ are statistically independent random variables at any time t, since the path delays τ_n are all independent due to the random placement of scatterers and the phases ϕ_n are also independent. Furthermore, the phases $\phi_n(t)$ at any time t can be treated as being uniformly distributed over the interval $[-\pi, \pi)$. The azimuth angles of arrival, θ_n are all independent due to the random placement of scatterers. In the limit as $N \to \infty$, the central limit theorem can be invoked, and $g_I(t)$ and $g_Q(t)$ can be treated as Gaussian random processes. Also, in the limit as $N \to \infty$, the discrete azimuth angles of arrival θ_n can be replaced by a continuous random variable θ having the probability density function $p(\theta)$. Using

these statistical properties, the autocorrelation function $\phi_{g_I g_I}(\tau)$ can be obtained from (2.1), (2.14), and (2.6) as follows:

$$\phi_{g_I g_I}(\tau) = \lim_{N \to \infty} \mathrm{E}_{\tau, \theta}[g_I(t) g_I(t + \tau)]$$

$$= \frac{\Omega_p}{2} \mathrm{E}_{\theta_n}[\cos(2\pi f_m \tau \cos(\theta_n))], \qquad (2.21)$$

where

$$\tau = (\tau_1, \tau_2, \ldots, \tau_N), \qquad (2.22)$$

$$\theta = (\theta_1, \theta_2, \ldots, \theta_N), \qquad (2.23)$$

$$\Omega_p = \mathrm{E}[|g(t)|^2] = \mathrm{E}[g_I^2(t)] + \mathrm{E}[g_Q^2(t)] = \sum_{n=1}^{N} C_n^2 \qquad (2.24)$$

and Ω_p can be interpreted as the received envelope power. Likewise, the cross-correlation function $\phi_{g_I g_Q}(\tau)$ can be derived as follows:

$$\phi_{g_I g_Q}(\tau) = \lim_{N \to \infty} \mathrm{E}_{\tau, \theta}[g_I(t) g_Q(t + \tau)]$$

$$= \frac{\Omega_p}{2} \mathrm{E}_{\theta_n}[\sin(2\pi f_m \tau \cos(\theta_n))]. \qquad (2.25)$$

Evaluation of the expectations in (2.21) and (2.25) requires the azimuth distribution of arriving plane waves $p(\theta)$, and the antenna azimuth gain pattern $G(\theta)$, as a function of the azimuth angle θ. One simple and commonly used model assumes that the plane waves arrive at the receiver antenna from all azimuth directions with equal probability, that is, $p(\theta) = 1/(2\pi), \theta \in [-\pi, \pi)$. This model was first suggested by Clarke [60] and is commonly referred to as Clarke's 2D isotropic scattering model. With 2D isotropic scattering and an isotropic receiver antenna with gain $G(\theta) = 1, \theta \in [-\pi, \pi)$, the expectation in (2.21) becomes

$$\phi_{g_I g_I}(\tau) = \frac{\Omega_p}{2} \int_{-\pi}^{\pi} \cos(2\pi f_m \tau \cos(\theta)) \, p(\theta) G(\theta) \mathrm{d}\theta$$

$$= \frac{\Omega_p}{2} \frac{1}{\pi} \int_{0}^{\pi} \cos(2\pi f_m \tau \sin(\theta)) \, \mathrm{d}\theta$$

$$= \frac{\Omega_p}{2} J_0(2\pi f_m \tau), \qquad (2.26)$$

where

$$J_0(x) = \frac{1}{\pi} \int_{0}^{\pi} \cos(x \sin(\theta)) \, \mathrm{d}\theta \qquad (2.27)$$

is the zero-order Bessel function of the first kind. The normalized autocorrelation function $\phi_{g_I g_I}(\tau)/(\Omega_p/2)$ in (2.26) is plotted against the normalized time delay $f_m \tau$ in Fig. 2.5.
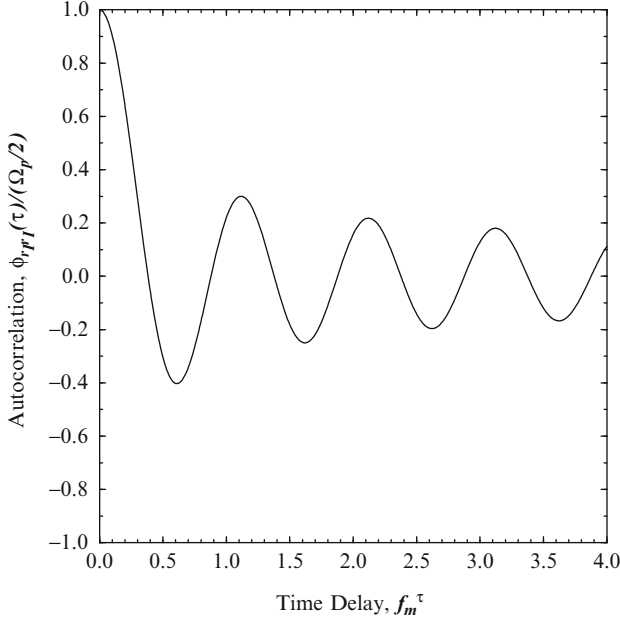
Fig. 2.5 Normalized autocorrelation function of the quadrature components of the received complex envelope with 2D isotropic scattering and an isotropic receiver antenna

Likewise, for 2D isotropic scattering and an isotropic receiver antenna, the cross-correlation function in (2.25) becomes

$$\phi_{g_I g_Q}(\tau) = \frac{\Omega_p}{2\pi} \int_{-\pi}^{\pi} \sin\left(2\pi f_m \tau \cos(\theta)\right) d\theta = 0. \tag{2.28}$$

A cross-correlation of zero means that $g_I(t)$ and $g_Q(t)$ are uncorrelated and, since they are Gaussian, independent random processes. The fact that $g_I(t)$ and $g_Q(t)$ are independent is a consequence of the symmetry of the 2D isotropic scattering environment and the isotropic receiver antenna. In general, $g_I(t)$ and $g_Q(t)$ are correlated random processes for non-isotropic scattering environments and/or a non-isotropic receiver antenna.

2.1.2 Doppler Spectrum

The autocorrelation of the received complex envelope $g(t) = g_I(t) + j g_Q(t)$ is

$$\phi_{gg}(\tau) = \frac{1}{2} E[g^*(t) g(t+\tau)]$$
$$= \phi_{g_I g_I}(\tau) + j \phi_{g_I g_Q}(\tau). \tag{2.29}$$

The Doppler Spectrum and time autocorrelation function are Fourier transform pairs, that is,

$$S_{gg}(f) = \int_{-\infty}^{\infty} \phi_{gg}(\tau) e^{-j2\pi f \tau} d\tau,$$

$$\phi_{gg}(\tau) = \int_{-\infty}^{\infty} S_{gg}(\tau) e^{j2\pi f \tau} d\tau,$$

where,

$$S_{gg}(f) = S_{g_I g_I}(f) + j S_{g_I g_Q}(f) \tag{2.30}$$

and $S_{gg}(f)$ is the Doppler spectrum. For the autocorrelation function in (2.26), the corresponding psd is [118, 6.671.7]

$$S_{g_I g_I}(f) = \mathscr{F}[\phi_{g_I g_I}(\tau)]$$

$$= \begin{cases} \dfrac{\Omega_p}{2\pi f_m} \dfrac{1}{\sqrt{1-(f/f_m)^2}} & |f| \le f_m \\ 0 & \text{otherwise} \end{cases} . \tag{2.31}$$

For the case of 2D isotropic scattering and an isotropic receiver antenna, $S_{g_I g_Q}(f) = 0$, so that $S_{gg}(f) = S_{g_I g_I}(f)$. We can also relate the power spectrum of the complex envelope $g(t)$ to that of the band-pass process $r(t)$. From (2.16), we have

$$\phi_{rr}(\tau) = \text{Re}\left\{ \phi_{gg}(\tau) e^{j2\pi f_c \tau} \right\}. \tag{2.32}$$

Using the identity

$$\text{Re}\{z\} = \frac{z + z^*}{2} \tag{2.33}$$

and the property $\phi_{gg}(\tau) = \phi_{gg}^*(-\tau)$, it follows that the band-pass Doppler spectrum is

$$S_{rr}(f) = \frac{1}{2} \left(S_{gg}(f - f_c) + S_{gg}(-f - f_c) \right). \tag{2.34}$$

Since $\phi_{gg}(\tau) = \phi_{gg}^*(-\tau)$, the Doppler spectrum $S_{gg}(f)$ is always a real-valued function of frequency, but not necessarily even. However, the band-pass Doppler spectrum $S_{rr}(f)$ is always real-valued and even.

The Doppler spectrum can be derived using a different approach that is sometimes very useful because it can avoid the need to evaluate integrals. As mentioned earlier, the incident power on the receiver antenna as a function of the azimuth angle θ has the distribution $p(\theta)$. The fraction of the total incoming power that arrives between angles θ and $\theta + d\theta$ is $p(\theta) d\theta$. If the antenna has an azimuth gain of $G(\theta)$,

then the power received between angles θ and $\theta + \mathrm{d}\theta$ is $G(\theta)p(\theta)\mathrm{d}\theta$. Therefore, the Doppler spectrum can be expressed as [134]

$$S_{gg}(f)|\mathrm{d}f| = \frac{\Omega_\mathrm{p}}{2}\Big(G(\theta)p(\theta) + G(-\theta)p(-\theta)\Big)|\mathrm{d}\theta|. \tag{2.35}$$

From Fig. 2.3, the Doppler frequency associated with the incident plane wave arriving at angle θ is

$$f = f_\mathrm{m}\cos(\theta), \tag{2.36}$$

and, hence,

$$|\mathrm{d}f| = f_\mathrm{m}| - \sin(\theta)\mathrm{d}\theta| = \sqrt{f_\mathrm{m}^2 - f^2}\,|\mathrm{d}\theta|. \tag{2.37}$$

Therefore,

$$S_{gg}(f) = \frac{\Omega_\mathrm{p}/2}{\sqrt{f_\mathrm{m}^2 - f^2}}\Big(G(\theta)p(\theta) + G(-\theta)p(-\theta)\Big), \tag{2.38}$$

where

$$\theta = \cos^{-1}(f/f_\mathrm{m}). \tag{2.39}$$

Hence, if $p(\theta)$ and $G(\theta)$ are known, the Doppler spectrum can be easily calculated. Once again, for 2D isotropic scattering and an isotropic antenna $G(\theta)p(\theta) = 1/(2\pi)$, so that

$$S_{gg}(f) = \begin{cases} \frac{\Omega_\mathrm{p}}{2\pi f_\mathrm{m}}\frac{1}{\sqrt{1-(f/f_\mathrm{m})^2}} & |f| \leq f_\mathrm{m} \\ 0 & \text{otherwise} \end{cases}. \tag{2.40}$$

The same result can be obtained from the autocorrelation function, but it requires the solution of a Fourier transform integral.

The normalized Doppler spectrum $S_{gg}(f)/(\Omega_\mathrm{p}/2\pi f_\mathrm{m})$ in (2.40) is plotted against the normalized Doppler frequency f/f_m in Fig. 2.6. Notice that $S_{gg}(f)$ is limited to the range of frequencies $0 \leq |f| \leq f_\mathrm{m}$ and $S_{gg}(f) = \infty$ at $f = \pm f_\mathrm{m}$. In reality, the Doppler spectrum is bounded, and the singular behavior at $f = \pm f_\mathrm{m}$ is due to the assumption of 2D plane wave propagation. Aulin [16] modified Clarke's 2D model to yield a 3D model that accounts for both azimuth and elevation angles of arrival. The resulting Doppler spectrum has the general same U-shape as Fig. 2.6, but it is bounded at frequencies $f = \pm f_\mathrm{m}$.

In some cases, it is appropriate to model the received signal as consisting of a strong specular or LoS component plus a scatter component. In this case, the azimuth distribution $p(\theta)$ might have the form

$$p(\theta) = \frac{1}{K+1}\hat{p}(\theta) + \frac{K}{K+1}\delta(\theta - \theta_0), \tag{2.41}$$
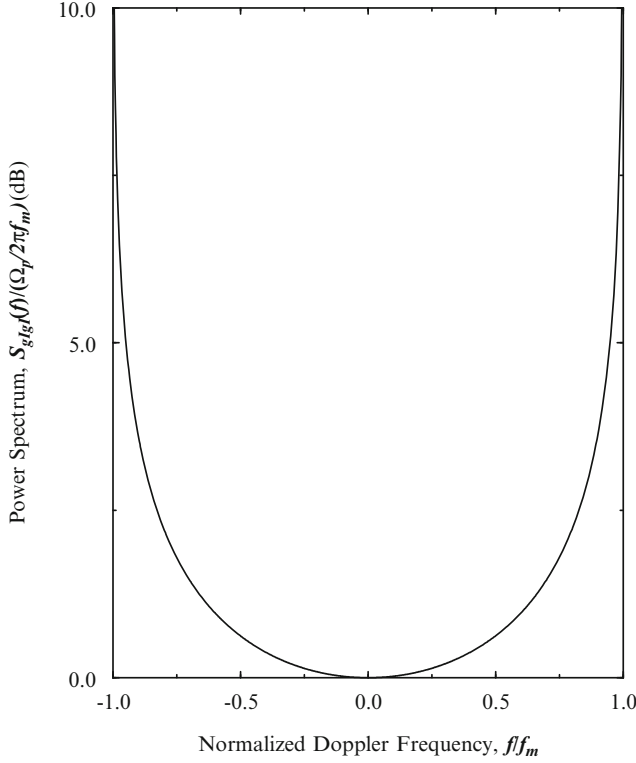
Fig. 2.6 Normalized psd of the quadrature components of the received complex envelope with 2D isotropic scattering channel and an isotropic receiver antenna

where $\hat{p}(\theta)$ is the continuous distribution of the *scatter* component, θ_0 is the AoA of the specular or LoS component, and K is the ratio of the received specular to scattered power. Figure 2.7 shows a plot of $p(\theta)$ for one such scattering environment, where the scatter component is characterized by 2D isotropic scattering, that is, $\hat{p}(\theta) = 1/(2\pi), \theta \in [-\pi, \pi)$. The correlation functions $\phi_{g_Ig_I}(\tau)$ and $\phi_{g_Ig_Q}(\tau)$ corresponding to (2.41) can be readily obtained from (2.21) and (2.25) as

$$\phi_{g_Ig_I}(\tau) = \frac{1}{K+1}\frac{\Omega_p}{2}J_0(2\pi f_m\tau) + \frac{K}{K+1}\frac{\Omega_p}{2}\cos(2\pi f_m\tau\cos(\theta_0)), \quad (2.42)$$

$$\phi_{g_Ig_Q}(\tau) = \frac{K}{K+1}\frac{\Omega_p}{2}\sin(2\pi f_m\tau\cos(\theta_0)). \quad (2.43)$$

The azimuth distribution in (2.41) yields a complex envelope having a Doppler spectrum of the form

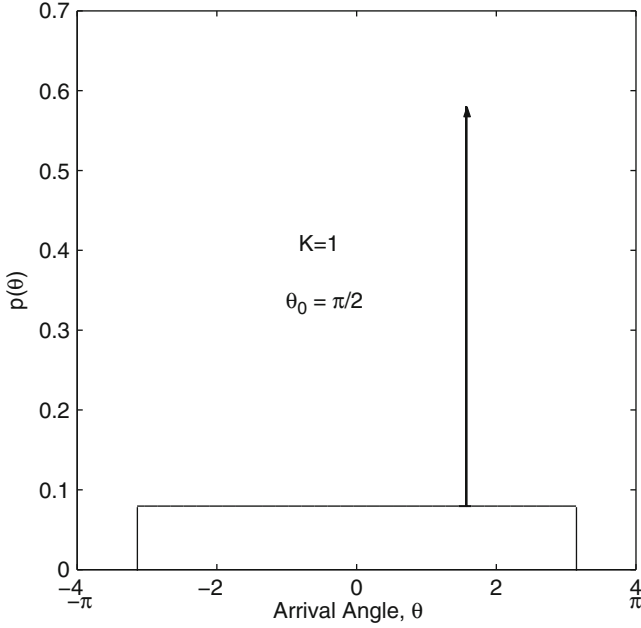$$S_{gg}(f) = \frac{1}{K+1}S_{gg}^c(f) + \frac{K}{K+1}S_{gg}^d(f), \quad (2.44)$$

Fig. 2.7 Plot of $p(\theta)$ versus θ with 2D isotropic scattering plus a LoS or specular component arriving at angle $\theta_0 = \pi/2$

where $S_{gg}^{\mathrm{d}}(f)$ is the discrete portion of the Doppler spectrum due to the specular component and $S_{gg}^{\mathrm{c}}(f)$ is the continuous portion of the Doppler spectrum due to the scatter component. For the case when $\hat{p}(\theta) = 1/(2\pi), \theta \in [-\pi, \pi]$, the correlation functions in (2.42) and (2.43) are obtained and the corresponding Doppler spectrum is

$$S_{gg}(f) = \begin{cases} \frac{1}{K+1} \cdot \frac{\Omega_{\mathrm{p}}}{2\pi f_{\mathrm{m}}} \frac{1}{\sqrt{1-(f/f_{\mathrm{m}})^2}} \\ \quad + \frac{K}{K+1} \frac{\Omega_{\mathrm{p}}}{2} \delta(f - f_{\mathrm{m}} \cos(\theta_0)) & 0 \le |f| \le f_{\mathrm{m}}. \\ 0 & \text{otherwise} \end{cases} \tag{2.45}$$

Note that the Doppler spectrum in (2.45) has the same shape as Fig. 2.6, except for the discrete spectral tone at frequency $f = f_{\mathrm{m}} \cos(\theta_0)$.

Sometimes the azimuth distribution $p(\theta)$ may not be uniform, a condition commonly called non-isotropic scattering. Several distributions have been suggested to model non-isotropic scattering. Once possibility is the Gaussian distribution

$$p(\theta) = \frac{1}{\sqrt{2\pi}\sigma_{\mathrm{S}}} \exp\left\{ -\frac{(\theta - \mu)^2}{2\sigma_{\mathrm{S}}^2} \right\}, \tag{2.46}$$
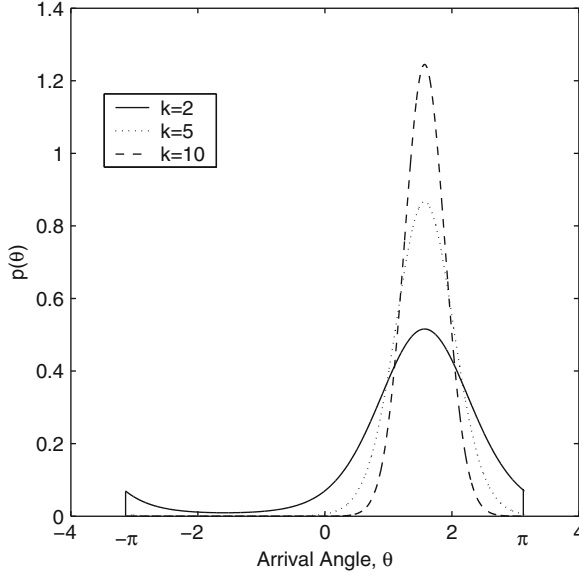
Fig. 2.8 Plot of $p(\theta)$ versus θ for the von Mises distribution with a mean angle-to-arrival $\mu = \pi/2$

where μ is the mean AoA, and σ_S is the root mean square (rms) AoA spread. Another possibility is the von Mises distribution

$$p(\theta) = \frac{1}{2\pi I_0(k)} \exp\{k\cos(\theta - \mu)\}, \tag{2.47}$$

where $\theta \in [-\pi, \pi)$, $I_0(\,\cdot\,)$ is the zeroth-order modified Bessel function of the first kind, $\mu \in [-\pi, \pi)$ is the mean AoA, and k controls the spread of scatterers around the mean. When $k = 0$, the von Mises distribution reduces to $p(\theta) = 1/(2\pi)$, yielding 2D isotropic scattering. As k increases, the scatterers become more clustered around the mean AoA μ and the scattering becomes increasingly non-isotropic as shown in Fig. 2.8. Still another possibility is the cosine distribution

$$p(\theta) = \begin{cases} \frac{\pi}{4\theta_{\max}} \cos\left(\frac{\pi}{2}\frac{\theta}{\theta_{\max}}\right), & |\theta| \le \theta_{\max} \le \frac{\pi}{2} \\ 0 & , \text{ elsewhere} \end{cases}. \tag{2.48}$$

The parameter $\theta_{\max}$ controls the AoA spread of the incoming waves. Figure 2.9 shows a plot of $p(\theta)$ for $\theta_{\max} = 30^\circ$, 60°, and 90°. Note that the distribution is symmetric about $\theta = 0$. Therefore, this azimuth distribution is less flexible than either the Gaussian or von Mises distributions. The density in (2.48) is sometimes used to model the *elevation* AoA distribution of scatterers in 3D propagation models, where the mean elevation AoA is 0° [291].
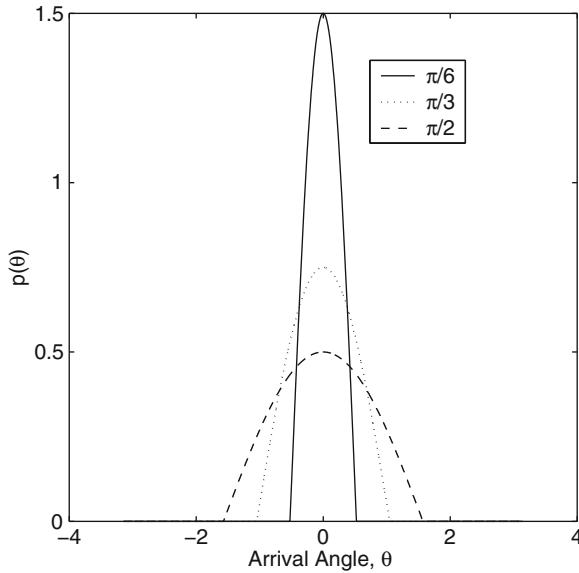
Fig. 2.9 Plot of $p(\theta)$ versus θ for the angle of arrival pdf in (2.48) for various θ_{max}. The mean angle of arrival is $\theta = 0$

Once the azimuth distribution is specified, the correlation functions $\phi_{g_I g_I}(\tau)$ and $\phi_{g_I g_Q}(\tau)$ can be readily obtained by evaluating the expectations in (2.21) and (2.25), respectively, using for example the densities in (2.46), (2.47), or (2.48). The Doppler spectrum, $S_{gg}(f)$, can be obtained by taking the Fourier transform of $\phi_{gg}(\tau)$ or, alternatively, by substituting the azimuth distribution $p(\theta)$ directly into (2.38).

2.1.3 Received Envelope and Phase Distribution

2.1.3.1 Rayleigh Fading

When the composite received signal consists of a large number of sinusoidal components, the received complex envelope $g(t) = g_I(t) + jg_Q(t)$ can be treated as a complex Gaussian random process. For some types of scattering environments, for example, 2D isotropic scattering, $g_I(t)$ and $g_Q(t)$ at any time t_1 are independent identically distributed Gaussian random variables with zero mean and variance $b_0 = \mathrm{E}[g_I^2(t_1)] = \mathrm{E}[g_Q^2(t_1)]$. Under these conditions, the magnitude of the received complex envelope

$$\alpha \overset{\triangle}{=} |g(t_1)| = \sqrt{g_I^2(t_1) + g_Q^2(t_1)} \tag{2.49}$$

has a Rayleigh distribution at any time t_1, as shown in (A.26), that is,

$$p_\alpha(x) = \frac{x}{b_0} \exp\left\{-\frac{x^2}{2b_0}\right\}, \qquad x \ge 0. \tag{2.50}$$

The average envelope power is $\Omega_p = E[\alpha^2] = 2b_0$ so that

$$p_\alpha(x) = \frac{2x}{\Omega_p} \exp\left\{-\frac{x^2}{\Omega_p}\right\}, \qquad x \ge 0. \tag{2.51}$$

This type of fading is called Rayleigh fading. The corresponding squared envelope $\alpha^2 = |g(t_1)|^2$ is exponentially distributed at any time t_1 with density

$$p_{\alpha^2}(x) = \frac{1}{\Omega_p} \exp\left\{-\frac{x}{\Omega_p}\right\}, \qquad x \ge 0. \tag{2.52}$$

The squared envelope is important for the performance analysis of digital communication systems because it is proportional to the received signal power and, hence, the received signal-to-noise ratio. This concept will be discussed in more detail in Chap. 5.

2.1.3.2 Ricean Fading

As mentioned earlier, some types of scattering environments have a specular or LoS component. In this case, $g_I(t)$ and $g_Q(t)$ are Gaussian random processes with nonzero means $m_I(t)$ and $m_Q(t)$, respectively. If we again assume that $g_I(t)$ and $g_Q(t)$ are uncorrelated, and the random variables $g_I(t_1)$ and $g_Q(t_1)$ have the same variance b_0, then the magnitude of the received complex envelope $\alpha = |g(t_1)|$ at any time t_1 has a Ricean distribution as shown in (A.61), that is,

$$p_\alpha(x) = \frac{x}{b_0} \exp\left\{-\frac{x^2+s^2}{2b_0}\right\} I_o\left(\frac{xs}{b_0}\right) \qquad x \ge 0, \tag{2.53}$$

where

$$s^2 = m_I^2(t) + m_Q^2(t) \tag{2.54}$$

is called the noncentrality parameter. This type of fading is called Ricean fading and is often used to describe fading in environments where an LoS or strong specular path exists between the transmitter and receiver.

A very simple Ricean fading model assumes that the means $m_I(t)$ and $m_Q(t)$ are constants, that is, $m_I(t) = m_I$ and $m_Q(t) = m_Q$. Such an approach will certainly yield a Ricean distributed envelope, but it lacks physical meaning. A better model has been suggested by Aulin [16], such that the azimuth distribution $p(\theta)$ is defined

in (2.41) and is shown in Fig. 2.7. In this case, the LoS or specular component determines the means $m_I(t)$ and $m_Q(t)$ of the in-phase and quadrature components, respectively, as follows:

$$m_I(t) = s \cdot \cos(2\pi f_m \cos(\theta_0)t + \phi_0) \tag{2.55}$$

$$m_Q(t) = s \cdot \sin(2\pi f_m \cos(\theta_0)t + \phi_0), \tag{2.56}$$

where $f_m \cos(\theta_0)$ and ϕ_0 are the Doppler shift and random phase associated with the LoS or specular component, respectively.

The Rice factor, K, is defined as the ratio of the LoS or specular power s^2 to scattered power $2b_0$, that is, $K = s^2/2b_0$. When $K = 0$, there is no LoS or specular component and the envelope exhibits Rayleigh fading. When $K = \infty$, there is no scatter component and the channel does not exhibit any fading. The envelope distribution can be rewritten in terms of the Rice factor and the average envelope power $E[\alpha^2] = \Omega_p = s^2 + 2b_0$ by first noting that

$$s^2 = \frac{K\Omega_p}{K+1}, \qquad b_0 = \frac{\Omega_p}{2(K+1)}. \tag{2.57}$$

Substituting s^2 and b_0 into (2.53) yields

$$p_\alpha(x) = \frac{2x(K+1)}{\Omega_p} \exp\left\{-K - \frac{(K+1)x^2}{\Omega_p}\right\} I_o\left(2x\sqrt{\frac{K(K+1)}{\Omega_p}}\right), \quad x \geq 0. \tag{2.58}$$

Figure 2.10 shows the Rice pdf for several values of K. The curve for $K = 0$ is the Rayleigh pdf.

The squared envelope $\alpha^2 = |g(t_1)|^2$ at any time t_1 has the following noncentral chi-square distribution with two degrees of freedom:

$$p_{\alpha^2}(x) = \frac{(K+1)}{\Omega_p} \exp\left\{-K - \frac{(K+1)x}{\Omega_p}\right\} I_o\left(2\sqrt{\frac{K(K+1)x}{\Omega_p}}\right), \quad x \geq 0. \tag{2.59}$$

2.1.3.3 Nakagami Fading

The Nakagami distribution was introduced by Nakagami in the early 1940s to characterize rapid fading in long distance HF channels [191]. The Nakagami distribution was selected to fit empirical data and is known to provide a closer match to some measurement data than either the Rayleigh, Ricean, or log-normal distributions [49].

Fig. 2.10 The Rice pdf for several values of K with $\Omega_p = 1$
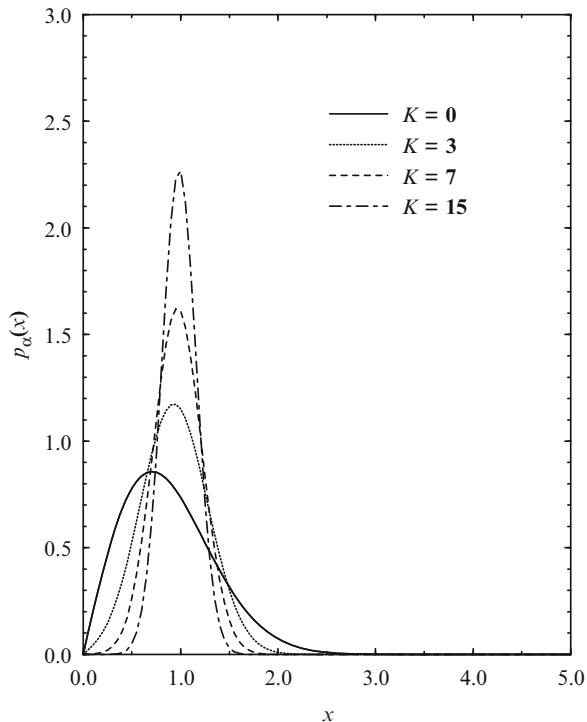
Nakagami fading describes the magnitude of the received complex envelope by the distribution

$$p_\alpha(x) = 2 \left(\frac{m}{\Omega_p} \right)^m \frac{x^{2m-1}}{\Gamma(m)} \exp\left\{ -\frac{mx^2}{\Omega_p} \right\} \qquad m \geq \frac{1}{2}, \tag{2.60}$$

where $\Omega_p = \mathrm{E}[\alpha^2]$. Figure 2.11 shows the Nakagami distribution for several values of the shape factor, m. Beyond its empirical justification, the Nakagami distribution is often used for the following reasons. First, the Nakagami distribution can model fading conditions that are either more or less severe than Rayleigh fading. When $m = 1$, the Nakagami distribution becomes the Rayleigh distribution, when $m = 1/2$ it becomes a one-sided Gaussian distribution, and when $m \to \infty$ the distribution approaches an impulse (no fading). Second, the Rice distribution can be closely approximated using the following relation between the Rice factor K and the Nakagami shape factor m [191];

$$K \approx \sqrt{m^2 - m} + m - 1 \tag{2.61}$$

$$m \approx \frac{(K+1)^2}{(2K+1)}. \tag{2.62}$$

Fig. 2.11 The Nakagami pdf
for several values of m with
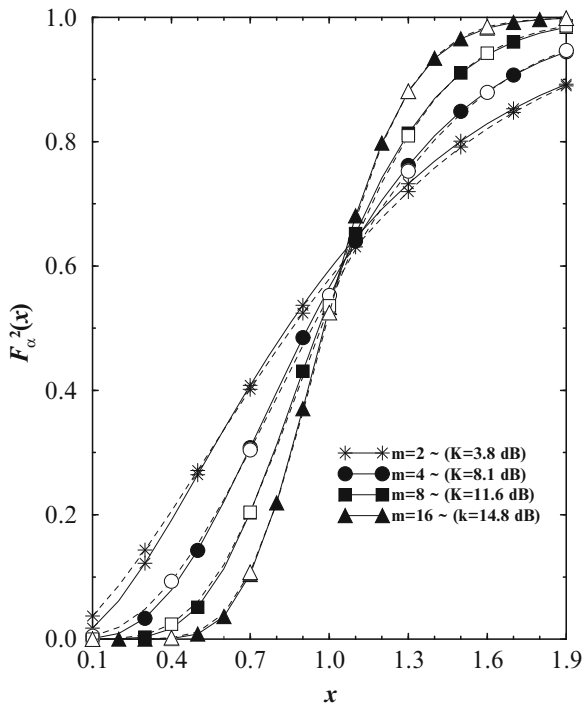$\Omega_{\mathrm{p}} = 1$
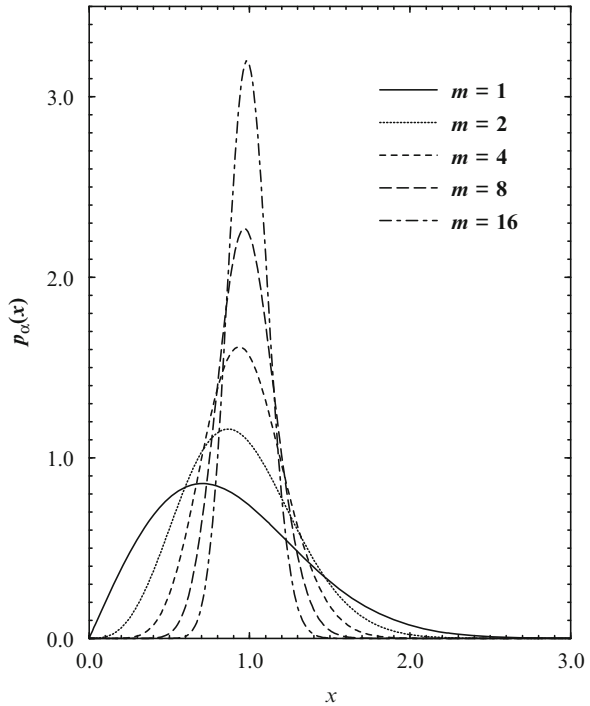
Finally, since the Rice distribution contains a Bessel function while the Nakagami distribution does not, the Nakagami distribution often leads to convenient closed form analytical expressions that may otherwise be intractable.

With Nakagami fading, the squared envelope has the Gamma distribution

$$p_{\alpha^2}(x) = \left(\frac{m}{\Omega_{\mathrm{p}}}\right)^m \frac{x^{m-1}}{\Gamma(m)} \exp\left\{-\frac{mx}{\Omega_{\mathrm{p}}}\right\}. \tag{2.63}$$

Using the relationship between the K factor and the shape factor m in (2.61), the cumulative distribution function (cdf), $F_{\alpha^2}(x) = \mathrm{P}(\alpha^2 \leq x)$ of the squared envelope with Nakagami and Ricean fading is plotted in Fig. 2.12. It is apparent from Fig. 2.12 that a Gamma distribution can approximate a noncentral chi-square distribution to a reasonable degree of accuracy. However, the reader is cautioned that the tails of the pdf are often the most important. The reason is that bit errors in a communication link tend to occur during deep fades, which correspond to small values of x in the cdf. Figure 2.12 does not show how well the tails of a Ricean pdf are approximated by a Nakagami pdf.

Fig. 2.12 Comparison of the cdf of the squared envelope with Ricean and Nakagami fading

Legend:
- $*$ $m=2 \sim (K=3.8 \text{ dB})$
- $\bullet$ $m=4 \sim (K=8.1 \text{ dB})$
- $\blacksquare$ $m=8 \sim (K=11.6 \text{ dB})$
- $\blacktriangle$ $m=16 \sim (k=14.8 \text{ dB})$

2.1.3.4   Envelope Phase

The phase of the received complex envelope $g(t) = g_I(t) + jg_Q(t)$ is

$$\phi(t) = \text{Tan}^{-1}\left(\frac{g_Q(t)}{g_I(t)}\right). \tag{2.64}$$

For Rayleigh fading, $g_I(t_1)$ and $g_Q(t_1)$ are independent identically distributed zero-mean Gaussian random variables at any time t_1. It follows (Appendix A.3.2.4) that the phase $\phi \equiv \phi(t_1)$ at any time t_1 is uniformly distributed over the interval $[-\pi, \pi)$, that is,

$$p_\phi(x) = \frac{1}{2\pi}, \quad -\pi \leq x \leq \pi. \tag{2.65}$$

For Ricean fading channels, the phase ϕ is not uniformly distributed and takes on a more complicated integral form.

2.1.4 Envelope Correlation and Spectra

The autocorrelation of the envelope $\alpha(t) = |g(t)|$ of a complex Gaussian random process can be expressed in terms of the hypergeometric function $F(\cdot,\cdot;\cdot,\cdot)$ as [72]

$$\phi_{\alpha\alpha}(\tau) = \mathrm{E}[\alpha(t)\,\alpha(t+\tau)]$$

$$= \frac{\pi}{2}|\phi_{gg}(0)|F\left(-\frac{1}{2}, -\frac{1}{2}; 1, \frac{|\phi_{gg}(\tau)|^2}{|\phi_{gg}(0)|^2}\right), \tag{2.66}$$

where

$$|\phi_{gg}(\tau)|^2 = \phi_{g_I g_I}^2(\tau) + \phi_{g_I g_Q}^2(\tau). \tag{2.67}$$

The above expression is analytically cumbersome, but fortunately a useful approximation can be obtained by expanding the hypergeometric function into the following infinite series:

$$F\left(-\frac{1}{2}, -\frac{1}{2}; 1, x\right) = 1 + \frac{1}{4}x + \frac{1}{64}x^2 + \cdots \tag{2.68}$$

Neglecting the terms beyond second order yields the approximation

$$\phi_{\alpha\alpha}(\tau) \doteq \frac{\pi}{2}|\phi_{gg}(0)|\left(1 + \frac{1}{4}\frac{|\phi_{gg}(\tau)|^2}{|\phi_{gg}(0)|^2}\right). \tag{2.69}$$

At $\tau = 0$, the approximation gives $\phi_{\alpha\alpha}(0) = 5\pi\Omega_p/8$, whereas the true value is $\phi_{\alpha\alpha}(0) = \Omega_p$. Hence, the relative error in the signal power is only 1.86%, leading us to believe that the approximation is probably very good.

The psd of the received envelope can be obtained by taking the Fourier transform of $\phi_{\alpha\alpha}(\tau)$. The psd will include a discrete spectral component at $f = 0$ due to the dc component of the received envelope. Since we are primarily interested in the continuous portion of the psd, the autocovariance function $\lambda_{\alpha\alpha}(\tau)$ is of interest, where

$$\lambda_{\alpha\alpha}(\tau) = \mathrm{E}[\alpha(t)\alpha(t+\tau)] - \mathrm{E}[\alpha(t)]\mathrm{E}[\alpha(t+\tau)]$$

$$= \frac{\pi}{2}|\phi_{gg}(0)|\left(1 + \frac{1}{4}\frac{|\phi_{gg}(\tau)|^2}{|\phi_{gg}(0)|^2}\right) - \frac{\pi}{2}|\phi_{gg}(0)|$$

$$= \frac{\pi}{8|\phi_{gg}(0)|}|\phi_{gg}(\tau)|^2. \tag{2.70}$$

For 2D isotropic scattering and an isotropic receiver antenna $|\phi_{gg}(\tau)|^2 = \phi_{g_I g_I}^2(\tau)$ and, therefore,

$$\lambda_{\alpha\alpha}(\tau) = \frac{\pi\Omega_p}{16}J_0^2(2\pi f_m\tau). \tag{2.71}$$
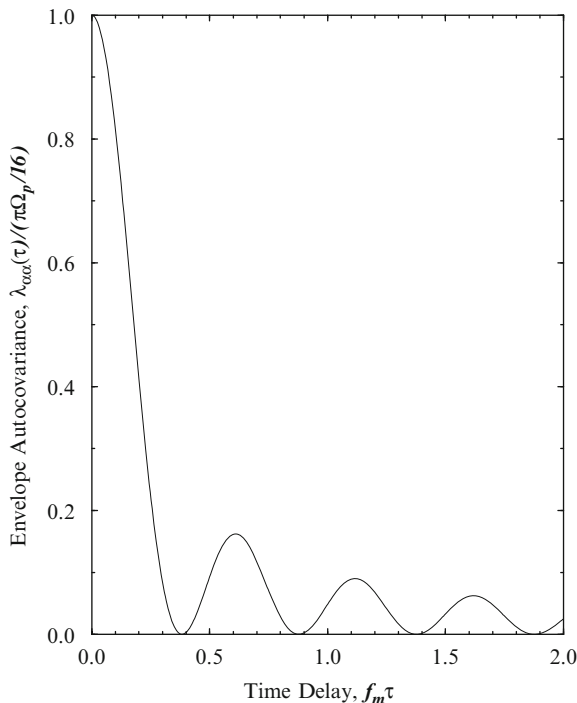
Fig. 2.13 Normalized envelope autocovariance against the normalized time delay $f_{\mathrm{m}}\tau$ for a 2D isotropic scattering with an isotropic receiver antenna

Figure 2.13 plots the normalized envelope auto-covariance $\lambda_{\alpha\alpha}(\tau)/(\pi\Omega_{\mathrm{p}}/16)$ against the normalized time delay $f_{\mathrm{m}}\tau$ for the case of 2D isotropic scattering and an isotropic receiver antenna.

The Fourier transform of $\lambda_{\alpha\alpha}(\tau)$ yields the continuous portion $S_{\alpha\alpha}^{\mathrm{c}}(f)$ of the envelope psd $S_{\alpha\alpha}(f)$, and can be calculated using the identities $|\phi_{gg}(\tau)|^2 = \phi_{gg}(\tau)\phi_{gg}^*(\tau)$ and $\phi_{gg}(\tau) = \phi_{gg}^*(-\tau)$ to write

$$
\begin{aligned}
S_{\alpha\alpha}^{\mathrm{c}}(f) &= \frac{\pi}{8|\phi_{gg}(0)|} S_{gg}(f) * S_{gg}(f) \\
&= \frac{\pi}{8|\phi_{gg}(0)|} \int_{-\infty}^{\infty} S_{gg}(x) S_{gg}(x-f)\mathrm{d}x \\
&= \frac{\pi}{8|\phi_{gg}(0)|} \int_{-f_{\mathrm{m}}}^{f_{\mathrm{m}}-|f|} S_{gg}(x) S_{gg}(x+|f|)\mathrm{d}x, \ \ 0 \le |f| \le 2f_{\mathrm{m}}. \quad (2.72)
\end{aligned}
$$

Note that $S_{\alpha\alpha}(f)$ is always real, positive, and even. It is centered about $f = 0$ with a spectral width of $4f_{\mathrm{m}}$, where f_{m} is the maximum Doppler frequency. To proceed further, we need to specify $S_{gg}(f)$. With 2D isotropic scattering and an isotropic
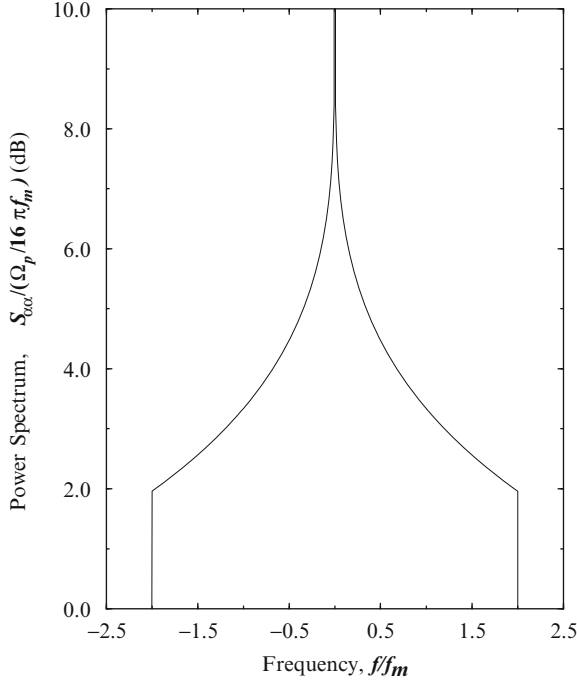
Fig. 2.14 Continuous portion of the normalized envelope psd against the normalized frequency f/f_{m} for a 2D isotropic scattering channel with an isotropic receiver antenna

receiver antenna $S_{gg}(f) = S_{g_{\mathrm{I}}g_{\mathrm{I}}}(f)$, where $S_{g_{\mathrm{I}}g_{\mathrm{I}}}(f)$ is given by (2.31). The result from evaluating (2.72) is (see Problem 2.9)

$$S_{\alpha\alpha}^{\mathrm{c}}(f) = \frac{\Omega_{\mathrm{p}}}{16\pi}\frac{1}{f_{\mathrm{m}}}K\left(\sqrt{1-\left(\frac{f}{2f_{\mathrm{m}}}\right)^2}\right) \qquad 0 \le |f| \le 2f_{\mathrm{m}}, \qquad (2.73)$$

where $K(\ \cdot\ )$ is the complete elliptic integral of the first kind, defined by

$$K(\gamma) = \int_0^1 \frac{\mathrm{d}x}{\sqrt{(1-x^2)(1-\gamma^2 x^2)}}. \qquad (2.74)$$

The continuous portion of the normalized envelope psd $S_{\alpha\alpha}(f)/(\Omega_{\mathrm{p}}/16\pi f_{\mathrm{m}})$ is plotted against the normalized frequency f/f_{m} in Fig. 2.14.

The psd of the received envelope $\alpha(t)$ for a non-isotropic scattering channel can be obtained using the above procedure. For example, consider the particular scattering environment shown in Fig. 2.7 with the associated Doppler spectrum in (2.45). To obtain the continuous portion of the psd of the envelope $\alpha(t)$, we substitute (2.45) into (2.72) to obtain (see Problem 2.10)
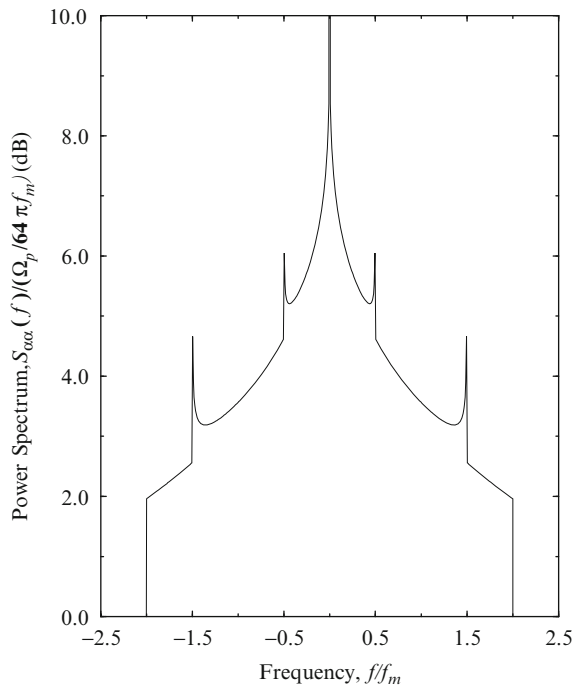
Fig. 2.15 Continuous portion of the normalized envelope psd against the normalized frequency f/f_m for the scattering environment shown in Fig. 2.7; $K = 10$ and $\theta_0 = \pi/3$

$$S_{\alpha\alpha}^{\mathrm{c}}(f) = \left(\frac{1}{K+1}\right)^2 \frac{\Omega_p}{16\pi f_\mathrm{m}} \left(K \left(\sqrt{1 - \left(\frac{f}{2f_\mathrm{m}}\right)^2} \right) \right.$$

$$\left. + \frac{K\pi}{\sqrt{1 - (f/f_\mathrm{m} + \cos(\theta_0))^2}} + \frac{K\pi}{\sqrt{1 - (f/f_\mathrm{m} - \cos(\theta_0))^2}} + K^2\pi^2 f_\mathrm{m}\delta(f) \right).$$

$$(2.75)$$

Figure 2.15 shows a plot of the continuous portion of the normalized envelope psd $S_{\alpha\alpha}(f)/(\Omega_p/(K+1)^2 16\pi f_\mathrm{m})$ against the normalized frequency f/f_m for $K = 10$ and $\theta_0 = \pi/3$.

2.1.4.1 Squared-Envelope Correlation and Spectrum

The autocorrelation of the squared envelope is

$$\phi_{\alpha^2\alpha^2}(\tau) = \mathrm{E}[\alpha^2(t)\alpha^2(t+\tau)]. \qquad (2.76)$$

Since $\alpha^2(t) = g_I^2(t) + g_Q^2(t)$, it follows that

$$\phi_{\alpha^2\alpha^2}(\tau) = E[g_I^2(t)g_I^2(t+\tau)] + E[g_Q^2(t)g_Q^2(t+\tau)]$$
$$+ E[g_I^2(t)g_Q^2(t+\tau)] + E[g_Q^2(t)g_I^2(t+\tau)]. \tag{2.77}$$

First consider the case where the propagation environment is such that $g_I(t)$ and $g_Q(t)$ have zero mean. Then the squared-envelope autocorrelation is (see Problem 2.11)

$$\phi_{\alpha^2\alpha^2}(\tau) = 4\phi_{g_Ig_I}^2(0) + 4\phi_{g_Ig_I}^2(\tau) + 4\phi_{g_Ig_Q}^2(\tau)$$
$$= 4\phi_{g_Ig_I}^2(0) + 4\left|\phi_{gg}(\tau)\right|^2. \tag{2.78}$$

Finally, the squared-envelope autocovariance is

$$\lambda_{\alpha^2\alpha^2}(\tau) = \phi_{\alpha^2\alpha^2}(\tau) - E^2[\alpha^2(t)]$$
$$= 4\left|\phi_{gg}(\tau)\right|^2. \tag{2.79}$$

With 2D isotropic scattering and an isotropic receiver antenna, the above expression reduces to

$$\lambda_{\alpha^2\alpha^2}(\tau) = \Omega_p^2 J_0^2(2\pi f_m\tau). \tag{2.80}$$

By comparing (2.70) and (2.79), we observe that the *approximate* autocorrelation function of the envelope and the *exact* autocorrelation function of the squared envelope are identical, except for a multiplicative constant. If the propagation environment is characterized by a specular or LoS component (e.g., Ricean fading), then $g_I(t)$ and $g_Q(t)$ have nonzero means and the autocovariance of the squared envelope has a more complicated form. Let

$$g_I(t) = \hat{g}_I(t) + m_I(t), \tag{2.81}$$
$$g_Q(t) = \hat{g}_Q(t) + m_Q(t), \tag{2.82}$$

where $m_I(t)$ and $m_Q(t)$ are the means of $g_I(t)$ and $g_Q(t)$, respectively. From Problem 2.12,

$$\phi_{\alpha^2\alpha^2}(\tau) = 4|\phi_{\hat{g}\hat{g}}|^2(\tau) + 4\phi_{\hat{g}_I\hat{g}_I}^2(0) + 4\text{Re}\left\{m(t)m^*(t+\tau)\phi_{\hat{g}\hat{g}}(\tau)\right\}$$
$$+ 2\left(|m(t)|^2 + |m(t+\tau)|^2\right)\phi_{\hat{g}_I\hat{g}_I}(0) + |m(t)|^2|m(t+\tau)|^2, \tag{2.83}$$

where

$$m(t) = m_I(t) + jm_Q(t), \tag{2.84}$$
$$m(t+\tau) = m_I(t+\tau) + jm_Q(t+\tau). \tag{2.85}$$

The squared-envelope autocovariance is

$$\lambda_{\alpha^2\alpha^2}(\tau) = 4\left|\phi_{\hat{g}\hat{g}}(\tau)\right|^2 + 4\text{Re}\left\{m(t)m^*(t+\tau)\phi_{\hat{g}\hat{g}}(\tau)\right\}. \tag{2.86}$$
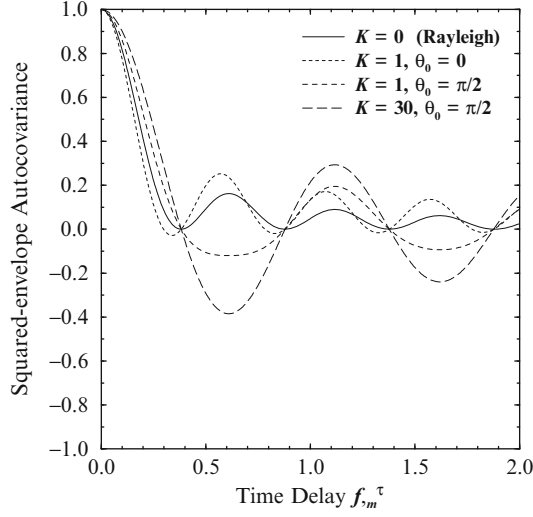
Fig. 2.16 Squared-envelope autocovariance against the normalized time delay $f_m \tau$ for the scattering environment shown in Fig. 2.7

Consider the scattering environment shown in Fig. 2.7. The corresponding correlation functions $\phi_{g_I g_I}(\tau)$ and $\phi_{g_I g_Q}(\tau)$ are given by (2.42) and (2.43), respectively, and the means $m_I(t)$ and $m_Q(t)$ are defined in (2.55) and (2.56). It can be shown that

$$\phi_{\hat{g}_I \hat{g}_I}(\tau) = \frac{1}{K+1} \frac{\Omega_p}{2} J_0(2\pi f_m \tau), \qquad (2.87)$$

$$\phi_{\hat{g}_I \hat{g}_Q}(\tau) = 0 \qquad (2.88)$$

and

$$m(t)m^*(t+\tau) = s^2 \left(\cos(2\pi f_m \tau \cos(\theta_0)) - j\sin(2\pi f_m \tau \cos(\theta_0)) \right)$$

$$= \frac{K\Omega_p}{K+1} \left(\cos(2\pi f_m \tau \cos(\theta_0)) - j\sin(2\pi f_m \tau \cos(\theta_0)) \right), \qquad (2.89)$$

where K is the Rice factor and θ_0 is the angle that the specular component makes with the MS direction of motion. Using these results in (2.86) gives

$$\lambda_{\alpha^2 \alpha^2}(\tau) = \left(\frac{\Omega_p}{K+1} \right)^2 J_0(2\pi f_m \tau) \left(J_0(2\pi f_m \tau) + 2K\cos(2\pi f_m \tau \cos(\theta_0)) \right). \qquad (2.90)$$

The normalized squared-envelope autocovariance is plotted in Fig. 2.16 as a function of the normalized time delay $f_m \tau$ for various values of K and θ_0.

2.1.5   Level Crossing Rates and Fade Durations

Two important second-order statistics associated with envelope fading are the level crossing rate (how often the envelope crosses a specified level) and the average fade duration (how long the envelope remains on average below a specified level). These quantities are affected not only by the scattering environment but also by the velocity of the MS.

2.1.5.1   Envelope Level Crossing Rate

The envelope level crossing rate at a specified envelope level R, L_R, is defined as the rate (in crossings per second) at which the envelope α crosses the level R in the positive (or negative) going direction. Obtaining the level crossing rate requires the joint pdf, $p(\alpha, \dot{\alpha})$, of the envelope level $\alpha = |g(t_1)|$ and the envelope slope $\dot{\alpha} = \mathrm{d}|g(t_1)|/\mathrm{d}t$ at any time instant t_1.[1] In terms of the joint pdf $p(\alpha, \dot{\alpha})$, the expected amount of time the envelope lies in the interval $(R, R + \mathrm{d}\alpha)$ for a given envelope slope $\dot{\alpha}$ and time increment $\mathrm{d}t$ is

$$p(R, \dot{\alpha})\mathrm{d}\alpha \mathrm{d}\mathrm{d}\dot{\alpha}\mathrm{d}t. \tag{2.91}$$

The time required for the envelope α to traverse the interval $(R, R + \mathrm{d}\alpha)$ *once* for a given envelope slope $\dot{\alpha}$ is

$$\mathrm{d}\alpha/\dot{\alpha}. \tag{2.92}$$

The ratio of these two quantities is the expected number of crossings of the envelope α within the interval $(R, R + \mathrm{d}\alpha)$ for a given envelope slope $\dot{\alpha}$ and time increment $\mathrm{d}t$, viz.

$$\dot{\alpha}p(R, \dot{\alpha})\mathrm{d}\dot{\alpha}\mathrm{d}t. \tag{2.93}$$

The expected number of crossings of the envelope level R for a given envelope slope $\dot{\alpha}$ in a time interval of duration T is

$$\int_0^T \dot{\alpha}p(R, \dot{\alpha})\mathrm{d}\dot{\alpha}\mathrm{d}t = \dot{\alpha}p(R, \dot{\alpha})\mathrm{d}\dot{\alpha}T. \tag{2.94}$$

The expected number of crossings of the envelope level R with a positive slope in the time interval T is

$$N_R = T \int_0^\infty \dot{\alpha}p(R, \dot{\alpha})\mathrm{d}\dot{\alpha}. \tag{2.95}$$

---

[1] For simplicity of notation, we suppress the time variable and simply write $\alpha \equiv \alpha(t_1)$ and $\dot{\alpha} \equiv \dot{\alpha}(t_1)$.

Finally, the expected number of crossings per second of the envelope level R, or the level crossing rate, is

$$L_R = \int_0^\infty \dot{\alpha} p(R, \dot{\alpha}) \mathrm{d}\dot{\alpha}. \tag{2.96}$$

This is actually a general result that applies to any random process characterized by the joint pdf $p(\alpha, \dot{\alpha})$.

Rice has derived the joint pdf $p(\alpha, \dot{\alpha})$ for a sine wave plus Gaussian noise [225]. A Ricean fading channel consists of LoS or specular (sine wave) component plus a scatter (Gaussian noise) component. For the case of a Ricean fading channel, we have the joint density function

$$p(\alpha, \dot{\alpha}) = \frac{\alpha (2\pi)^{-3/2}}{\sqrt{Bb_0}} \times \int_{-\pi}^{\pi} \exp\left\{ -\frac{1}{2Bb_0} \left[B\left(\alpha^2 - 2\alpha s \cos(\theta) + s^2\right) \right. \right.$$
$$\left. \left. + (b_0 \dot{\alpha} + b_1 s \sin(\theta))^2 \right] \right\} \mathrm{d}\theta, \tag{2.97}$$

where s is the non-centrality parameter in the Rice distribution, and $B = b_0 b_2 - b_1^2$, and where b_0, b_1, and b_2 are constants that are derived from the power spectrum of the scatter component. For the scattering environment described by (2.41) and Fig. 2.7, the sine wave corresponds to the specular component arriving at angle θ_0, while the Gaussian noise is due to the scatter component with azimuth distribution $\hat{p}(\theta) = 1/(2\pi), -\pi \leq \theta \leq \pi$. Note that the joint pdf derived by Rice in (2.97) is general enough to apply to scattering environments described by other $\hat{p}(\theta)$ as well.

Suppose that the specular or LoS component of the complex envelope $g(t)$ has a Doppler frequency equal $f_q = f_m \cos(\theta_0)$, where $0 \leq |f_q| \leq f_m$. In this case [225]

$$b_n = (2\pi)^n \int_{-f_m}^{f_m} S_{gg}^c(f)(f - f_q)^n \mathrm{d}f \tag{2.98}$$

$$= (2\pi)^n b_0 \int_0^{2\pi} \hat{p}(\theta) G(\theta) \left(f_m \cos(\theta) - f_q\right)^n \mathrm{d}\theta, \tag{2.99}$$

where $\hat{p}(\theta)$ is the azimuth distribution of the *scatter* component, $G(\theta)$ is the antenna gain pattern, and $S_{gg}^c(f)$ is the corresponding continuous portion of the Doppler power spectrum. Equivalence between (2.98) and (2.99) can be established using (2.38). Note that $S_{gg}^c(f)$ is given by the Fourier transform of

$$\phi_{gg}^c(\tau) = \phi_{g_I g_I}^c(\tau) + j \phi_{g_I g_Q}^c(\tau), \tag{2.100}$$

where

$$\phi_{g_I g_I}^c(\tau) = \frac{\Omega_p}{2} \int_0^{2\pi} \cos(2\pi f_m \tau \cos(\theta)) \hat{p}(\theta) G(\theta) \mathrm{d}\theta, \tag{2.101}$$

$$\phi^c_{g_I g_Q}(\tau) = \frac{\Omega_p}{2} \int_0^{2\pi} \sin(2\pi f_m \tau \cos(\theta)) \hat{p}(\theta) G(\theta) d\theta. \qquad (2.102)$$

In some special cases, the psd $S^c_{gg}(f)$ is symmetrical about the frequency $f_q = f_m \cos(\theta_0)$. This condition occurs, for example, when $f_q = 0$ ($\theta_0 = 90^\circ$), $\hat{p}(\theta) = 1/(2\pi), -\pi \le \theta \le \pi$, and $G(\theta) = 1$. In this case, $b_n = 0$ for all odd values of n (and in particular $b_1 = 0$) so that (2.97) reduces to the convenient product form

$$p(\alpha, \dot{\alpha}) = \sqrt{\frac{1}{2\pi b_2}} \exp\left\{-\frac{\dot{\alpha}^2}{2b_2}\right\} \cdot \frac{\alpha}{b_0} \exp\left\{-\frac{(\alpha^2 + s^2)}{2b_0}\right\} I_0\left(\frac{\alpha s}{b_0}\right)$$

$$= p(\dot{\alpha}) \cdot p(\alpha). \qquad (2.103)$$

Since $p(\alpha, \dot{\alpha}) = p(\dot{\alpha}) \cdot p(\alpha)$ in (2.103), it follows that α and $\dot{\alpha}$ are statistically independent. When $f_q = 0$ and $\hat{p}(\theta) = 1/(2\pi)$, a closed form expression can be obtained for the envelope level crossing. Substituting (2.40) into (2.98) gives

$$b_n = \begin{cases} b_0 (2\pi f_m)^n \frac{1 \cdot 3 \cdot 5 \, \cdots \, (n-1)}{2 \cdot 4 \cdot 6 \, \cdots \, n} & n \text{ even} \\ 0 & n \text{ odd} \end{cases}. \qquad (2.104)$$

Therefore, $b_1 = 0$ and $b_2 = b_0 (2\pi f_m)^2/2$. By substituting the joint density in (2.103) into (2.96) and using the expression for b_0 in (2.57), we obtain the envelope level crossing rate

$$L_R = \sqrt{2\pi(K+1)} f_m \rho e^{-K-(K+1)\rho^2} I_0\left(2\rho\sqrt{K(K+1)}\right), \qquad (2.105)$$

where

$$\rho = \frac{R}{\sqrt{\Omega_p}} = \frac{R}{R_{rms}} \qquad (2.106)$$

and $R_{rms} \stackrel{\triangle}{=} \sqrt{E[\alpha^2]}$ is the rms envelope level. Under the further condition that $K = 0$ (Rayleigh fading), the above expression simplifies to

$$L_R = \sqrt{2\pi} f_m \rho e^{-\rho^2}. \qquad (2.107)$$

Notice that the level crossing rate is directly proportional to the maximum Doppler frequency f_m and, hence, the MS speed $v = f_m/\lambda_c$. The normalized level crossing rate L_R/f_m in (2.105) is plotted in Fig. 2.17 as a function of ρ and K.

2.1.5.2 Zero Crossing Rate

Recall that received complex envelope $g(t) = g_I(t) + g_Q(t)$ is a complex Gaussian random process. If the channel is characterized by a specular or LoS component,
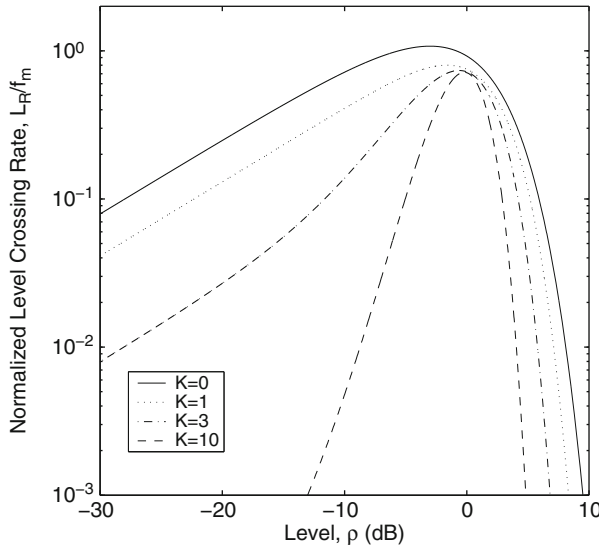
Fig. 2.17 Normalized level crossing rate for the scattering environment shown in Fig. 2.7 with $\theta_0 = 90^\circ$

then $g_I(t)$ and $g_Q(t)$ have mean values $m_I(t)$ and $m_Q(t)$, respectively. Here we are interested in the zero crossing rate of the zero-mean Gaussian random processes $\hat{g}_I(t) = g_I(t) - m_I(t)$ and $\hat{g}_Q(t) = g_Q(t) - m_Q(t)$. Rice [225] has derived this zero crossing rate as

$$L_Z = \frac{1}{\pi}\sqrt{\frac{b_2}{b_0}}. \tag{2.108}$$

When the scatter component has the azimuth distribution $\hat{p}(\theta) = 1/(2\pi), -\pi \leq \theta \leq \pi$, the zero crossing rate is

$$L_Z = \sqrt{2} f_m. \tag{2.109}$$

Similar to the level crossing rate, the zero crossing rate is directly proportional to the maximum Doppler frequency f_m.

2.1.5.3 Average Fade Duration

Another quantity of interest is the average duration that the envelope remains below a specified level R. Although the pdf of the envelope fade duration is unknown, the average fade duration can be calculated. Consider a very long time interval of length T and let t_i be the duration of the ith fade below the level R. The probability that the received envelope is less than R is

$$P[\alpha \leq R] = \frac{1}{T}\sum_i t_i. \tag{2.110}$$

The average fade duration is equal to

$$\bar{t} = \frac{\sum_i t_i}{T L_R} = \frac{P[\alpha \le R]}{L_R}. \tag{2.111}$$

If the envelope is Ricean distributed as in (2.58), then

$$P(\alpha \le R) = \int_0^R p(\alpha) d\alpha = 1 - Q\left(\sqrt{2K}, \sqrt{2(K+1)\rho^2}\right), \tag{2.112}$$

where $Q(a,b)$ is the Marcum Q function. Moreover, if we again assume that $f_q = 0$ and $\hat{p}(\theta) = 1/(2\pi)$, we have

$$\bar{t} = \frac{1 - Q\left(\sqrt{2K}, \sqrt{2(K+1)\rho^2}\right)}{\sqrt{2\pi(K+1)} f_m \rho e^{-K-(K+1)\rho^2} I_0\left(2\rho\sqrt{K(K+1)}\right)}. \tag{2.113}$$

If $K = 0$ (Rayleigh fading), then

$$P[\alpha \le R] = \int_0^R p(\alpha) d\alpha = 1 - e^{-\rho^2} \tag{2.114}$$

and

$$\bar{t} = \frac{e^{\rho^2} - 1}{\rho f_m \sqrt{2\pi}}. \tag{2.115}$$

The normalized average fade duration $\bar{t} f_m$ in (2.113) is plotted in Fig. 2.18 as a function of ρ.

The level crossing rate, zero crossing rate, and average fade duration all depend on the velocity of the MS, since $f_m = v/\lambda_c$. Very deep fades tend to occur infrequently and do not last very long. For example, at 60 miles/h and 900 MHz, the maximum Doppler frequency is $f_m = 80$ Hz. Therefore, with 2D isotropic scattering and Rayleigh fading ($K = 0$), there are $L_R = 74$ fades/s at $\rho = 0$ dB with an average fade duration of 8.5 ms. However, at $\rho = -20$ dB there are only 20 fades/s with an average fade duration of 0.5 ms. Note that since ρ represents a normalized envelope (magnitude) level, we use $\rho_{(dB)} = 20\log_{10}\rho$. We can also observe from Fig. 2.17 that for small $\rho_{(dB)}$, the level crossing rate decreases with an increasing Rice factor K. Furthermore, we see from Fig. 2.18 that for small $\rho_{(dB)}$ the average fade duration increases with increasing K. Hence, as K increases the fades occur less frequently, but last longer when they do occur.

2.1.6 Space–Time Correlation

Many mobile radio systems use receiver antenna diversity, where spatially separated receiver antennas are used to provide multiple faded replicas of the same information bearing signal. In order for such diversity systems to provide the maximum diversity gain, it is desirable that the multiple faded replicas experience uncorrelated
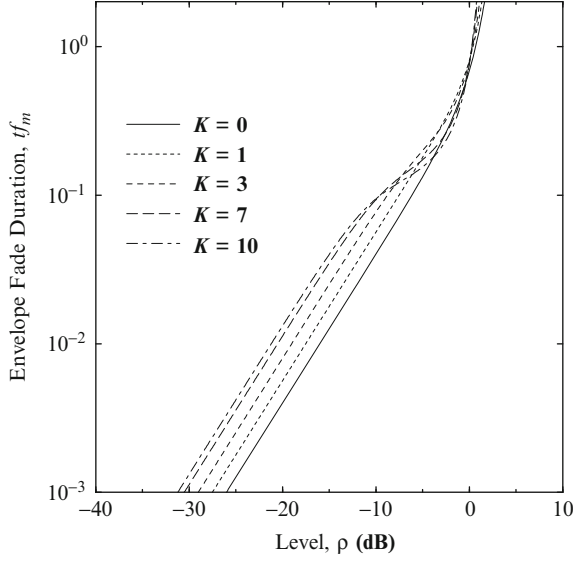
Fig. 2.18 Normalized average fade duration for the scattering environment shown in Fig. 2.7 with $\theta_0 = 90°$

fading. The spatial correlation characteristics are needed for determining the required spatial separation between antenna elements so that they are sufficiently decorrelated. Moreover, it is sometimes desirable to simultaneously characterize both the spatial and temporal channel correlation characteristics. For these purposes, space–time correlation functions are useful. To obtain the space–time correlation functions, it is necessary to specify the scattering geometry. One possibility for NLoS conditions is the single-ring model shown in Fig. 2.19, where the BS and MS are located at O_B and O_M, respectively, and separated by distance D, and the scatterers are assumed to be located on a ring of radius R centered around the MS such that $D \gg R$. We consider two MS antennas, $A_M^{(q)}, q = 1, 2$, separated by distance δ_M. The MS antenna array is oriented with angle θ_M with respect to the x-axis, and the MS moves with velocity v and angle γ_M with respect to the x-axis. For the environment shown in Fig. 2.19, the channel from O_B to $A_M^{(q)}$ has the complex envelope

$$g_q(t) = \sum_{n=1}^{N} C_n e^{j\phi_n - j2\pi(\varepsilon_n + \varepsilon_{nq})/\lambda_c} e^{j2\pi f_m t \cos\left(\alpha_M^{(n)} - \gamma_M\right)}, \quad q = 1, 2, \tag{2.116}$$

where ε_n and ε_{nq} denote the distances $O_B - S_n$ and $S_M^{(n)} - A_M^{(q)}, q = 1, 2$, respectively. From the law of cosines, the distances ε_n and ε_{nq} can be expressed as a function of the AoA $\alpha_M^{(n)}$ as follows:

$$\varepsilon_n^2 = D^2 + R^2 + 2DR\cos\left(\alpha_M^{(n)}\right), \tag{2.117}$$

$$\varepsilon_{nq}^2 = ((1.5 - q)\delta_M)^2 + R^2 - 2(1.5 - q)\delta_M R\cos\left(\alpha_M^{(n)} - \theta_M\right), \quad q = 1, 2. \tag{2.118}$$
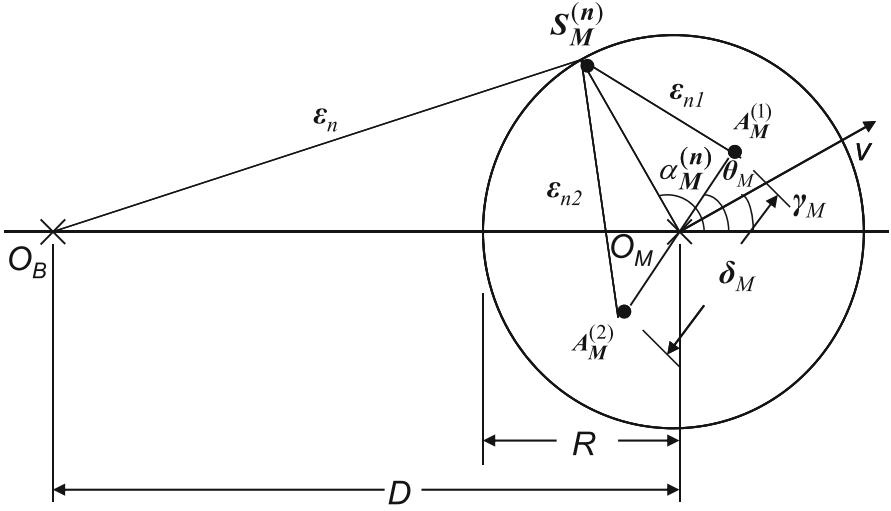
Fig. 2.19 Single-ring scattering model for NLoS propagation on the forward link of a cellular system. The MS is surrounded by a scattering ring of radius R and is at distance D from the BS, where $R \ll D$

Recognizing that $R/D \ll 1$, $\delta_{\mathrm{M}} \ll R$ and $\sqrt{1 \pm x} \approx 1 \pm x/2$ for small x, we have

$$\varepsilon_n \approx D + R \cos\left(\alpha_{\mathrm{M}}^{(n)}\right), \tag{2.119}$$

$$\varepsilon_{nq} \approx R - (1.5 - q)\delta_{\mathrm{M}} \cos\left(\alpha_{\mathrm{M}}^{(n)} - \theta_{\mathrm{M}}\right), \ q = 1, 2. \tag{2.120}$$

Substituting (2.119) and (2.120) into (2.116) gives

$$g_q(t) = \sum_{n=1}^{N} C_n \mathrm{e}^{\mathrm{j}\phi_n - \mathrm{j}2\pi\left(D + R\cos\alpha_{\mathrm{M}}^{(n)} + R - (1.5 - q)\delta_{\mathrm{M}}\cos(\alpha_{\mathrm{M}}^{(n)} - \theta_{\mathrm{M}})\right)/\lambda_{\mathrm{c}}}$$

$$\times \mathrm{e}^{\mathrm{j}2\pi f_{\mathrm{m}} t \cos(\alpha_{\mathrm{M}}^{(n)} - \gamma_{\mathrm{M}})}, \ q = 1, 2. \tag{2.121}$$

The space–time correlation function between the two complex faded envelopes $g_1(t)$ and $g_2(t)$ is

$$\phi_{g_1, g_2}(\delta_{\mathrm{M}}, \tau) = \frac{1}{2}\mathrm{E}\left[g_1(t)g_2(t + \tau)^*\right]. \tag{2.122}$$

Using (2.121) and (2.122), the space–time correlation function between $g_1(t)$ and $g_2(t)$ can be written as

$$\phi_{g_1, g_2}(\delta_{\mathrm{M}}, \tau) = \frac{\Omega_{\mathrm{p}}}{2N} \sum_{n=1}^{N} \mathrm{E}\left[\mathrm{e}^{\mathrm{j}2\pi(\delta_{\mathrm{M}}/\lambda_{\mathrm{c}})\cos\left(\alpha_{\mathrm{M}}^{(n)} - \theta_{\mathrm{M}}\right)} \mathrm{e}^{-\mathrm{j}2\pi f_{\mathrm{m}}\tau\cos\left(\alpha_{\mathrm{M}}^{(n)} - \gamma_{\mathrm{M}}\right)}\right]. \tag{2.123}$$

Since the number of scatters is infinite, the discrete angles of arrival $\alpha_M^{(n)}$ can be replaced with a continuous random variable α_M with probability density function $p(\alpha_M)$. Hence, the space–time correlation function becomes

$$\phi_{g_1,g_2}(\delta_M, \tau) = \frac{\Omega_p}{2} \int_0^{2\pi} e^{jb\cos(\alpha_M - \theta_M)} e^{-ja\cos(\alpha_M - \gamma_M)} p(\alpha_M) d\alpha_M, \qquad (2.124)$$

where $a = 2\pi f_m \tau$ and $b = 2\pi \delta_M / \lambda_c$.

For the case of 2D isotropic scattering with isotropic MS antenna, $p(\alpha_M) = 1/(2\pi), -\pi \leq \alpha_M \leq \pi$, and the space–time correlation function becomes

$$\phi_{g_1,g_2}(\delta_M, \tau) = \frac{\Omega_p}{2} J_0\left(\sqrt{a^2 + b^2 - 2ab\cos(\theta_M - \gamma_M)}\right). \qquad (2.125)$$

The spatial and temporal correlation functions can be obtained by setting $\tau = 0$ and $\delta_M = 0$, respectively. This gives $\phi_{g_1,g_2}(\delta_M) = \phi_{g_1,g_2}(\delta_M, 0) = \frac{\Omega_p}{2} J_0(2\pi\delta_M/\lambda_c)$ and $\phi_{gg}(\tau) = \phi_{g_1,g_2}(0, \tau) = \frac{\Omega_p}{2} J_0(2\pi f_m \tau)$, which matches our earlier result in (2.26) as expected. For the case of 2D isotropic scattering and an isotropic MS antenna, it follows that Fig. 2.13 also plots the normalized envelope spatial autocovariance function $\lambda_{\alpha\alpha}(\ell)/(\pi\Omega_p/16)$ against the normalized spatial separation $f_m \tau = \delta_M/\lambda_c$. The spatial autocovariance function is zero at $\delta_M/\lambda_c = 0.38$ and is less than 0.3 for $\delta_M/\lambda_c > 0.38$. The implication is that under conditions of 2D isotropic scattering and isotropic MS antennas, sufficient spatial decorrelation can be obtained by spacing the MS antenna elements a half wavelength apart.

2.1.6.1   Received Signal at the Base Station

Radio channels are reciprocal in the sense that if a propagation path exists, it will carry energy equally well in either the uplink or downlink directions. That is, the plane waves in either direction will propagate by exactly the same set of scatterers. Therefore, we expect that the temporal autocorrelation functions and Doppler spectra will be the same for both the uplink and downlink directions. However, for cellular land mobile radio applications, most of the scatters are in the vicinity of the MS, while the BS antennas are elevated and free of local scatters. Consequently, the plane waves will arrive at the BS antennas with a narrow AoA spread, whereas they arrive with a large AoA spread at the MS. This will cause significant differences in the spatial correlation properties of the uplink and downlink. As we will see, a much larger spatial distance is required to obtain a given degree of spatial decorrelation at the BS as compared to the MS.

To obtain the space–time correlation functions, it is once again necessary to specify the scattering geometry. One possibility for NLoS conditions is the single ring model shown in Fig. 2.20, where the MS and BS are located at O_M and O_B, respectively, and separated by distance D, and the scatterers are assumed to be
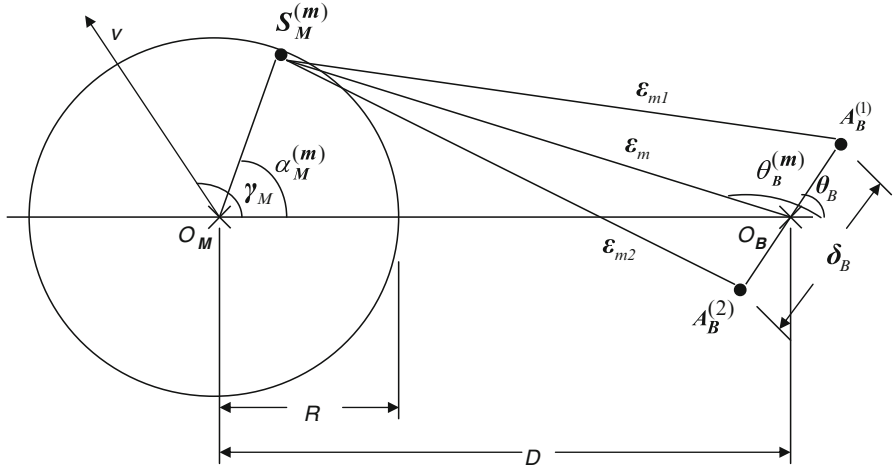
Fig. 2.20 Single-ring scattering model for NLoS propagation on the reverse link of a cellular system. The MS is surrounded by a scattering ring of radius R and is at distance D from the BS, where $R \ll D$

located on a ring of radius R centered around the MS such that $D \gg R$. We consider two BS antennas, $A_{\mathrm{B}}^{(q)}, q = 1, 2$, separated by distance δ_{B}. The BS antenna array is oriented with angle θ_{B} with respect to the x-axis, and the MS moves with velocity v and angle γ_{M} with respect to the x-axis. For the environment shown in Fig. 2.20, the channel from O_{M} to $A_{\mathrm{B}}^{(q)}$ has the complex envelope

$$g_q(t) = \sum_{m=1}^{N} C_m e^{j\phi_m - j2\pi(R + \varepsilon_{mq})/\lambda_c} e^{j2\pi f_m t \cos\left(\alpha_{\mathrm{M}}^{(m)} - \gamma_{\mathrm{M}}\right)}, \ q = 1, 2, \qquad (2.126)$$

where ε_{mq} denotes the distance $S_{\mathrm{M}}^{(m)} - A_{\mathrm{B}}^{(q)}, q = 1, 2$. To proceed further, we need to express ε_{mq} as a function of $\alpha_{\mathrm{M}}^{(m)}$.

Applying the cosine law to the triangle $\triangle S_{\mathrm{M}}^{(m)} O_{\mathrm{B}} A_{\mathrm{B}}^{(q)}$, the distance ε_{mq} can be expressed as a function of the angle $\theta_{\mathrm{B}}^{(m)} - \theta_{\mathrm{B}}$ as follows:

$$\varepsilon_{mq}^2 = ((1.5 - q)\delta_{\mathrm{B}})^2 + \varepsilon_m^2 - 2(1.5 - q)\delta_{\mathrm{B}}\varepsilon_m \cos\left(\theta_{\mathrm{B}}^{(m)} - \theta_{\mathrm{B}}\right), q = 1, 2, \quad (2.127)$$

where ε_m is the distance $S_{\mathrm{M}}^{(m)} - O_{\mathrm{B}}$. By applying the sine law to the triangle $\triangle O_{\mathrm{M}} S_{\mathrm{M}}^{(m)} O_{\mathrm{B}}$, we obtain the following identity

$$\frac{\varepsilon_m}{\sin\left(\alpha_{\mathrm{M}}^{(m)}\right)} = \frac{R}{\sin\left(\pi - \theta_{\mathrm{B}}^{(m)}\right)} = \frac{D}{\sin\left(\pi - \alpha_{\mathrm{M}}^{(m)} - \left(\pi - \theta_{\mathrm{B}}^{(m)}\right)\right)}. \qquad (2.128)$$

Since the angle $\pi - \theta_B^{(m)}$ is small, we can apply the small angle approximations $\sin x \approx x$ and $\cos x \approx 1$ for small x, to the second equality in the above identity. This gives

$$\frac{R}{\left(\pi - \theta_B^{(m)}\right)} \approx \frac{D}{\sin\left(\pi - \alpha_M^{(m)}\right)} \tag{2.129}$$

or

$$\left(\pi - \theta_B^{(m)}\right) \approx (R/D)\sin\left(\pi - \alpha_M^{(m)}\right). \tag{2.130}$$

It follows that the cosine term in (2.127) becomes

$$\cos\left(\theta_B^{(m)} - \theta_B\right) = \cos\left(\pi - \theta_B - \left(\pi - \theta_B^{(m)}\right)\right)$$

$$= \cos\left(\pi - \theta_B\right)\cos\left(\pi - \theta_B^{(m)}\right) + \sin\left(\pi - \theta_B\right)\sin\left(\pi - \theta_B^{(m)}\right)$$

$$\approx \cos(\pi - \theta_B) + \sin(\pi - \theta_B)(R/D)\sin\left(\pi - \alpha_M^{(m)}\right)$$

$$= -\cos(\theta_B) + (R/D)\sin(\theta_B)\sin\left(\alpha_M^{(m)}\right). \tag{2.131}$$

Substituting the approximation in (2.131) into (2.127), along with $\delta_B/\varepsilon_m \ll 1$, gives

$$\varepsilon_{mq}^2 \approx \varepsilon_m^2\left(1 - 2(1.5 - q)\frac{\delta_B}{\varepsilon_m}\left((R/D)\sin\left(\theta_B\right)\sin\left(\alpha_M^{(m)}\right) - \cos\left(\theta_B\right)\right)\right). \tag{2.132}$$

Applying the approximation $\sqrt{1 \pm x} \approx 1 \pm x/2$ for small x, we have

$$\varepsilon_{mq} \approx \varepsilon_m - (1.5 - q)\delta_B\left((R/D)\sin(\theta_B)\sin\left(\alpha_M^{(m)}\right) - \cos\left(\theta_B\right)\right). \tag{2.133}$$

Applying the cosine law to the triangle $\triangle O_M S_M^{(m)} O_B$, we have

$$\varepsilon_m^2 = D^2 + R^2 - 2DR\cos\left(\alpha_M^{(m)}\right)$$

$$\approx D^2\left(1 - 2(R/D)\cos\left(\alpha_M^{(m)}\right)\right), \tag{2.134}$$

and again using the approximation $\sqrt{1 \pm x} \approx 1 \pm x/2$ for small x, we have

$$\varepsilon_m \approx D - R\cos\left(\alpha_M^{(m)}\right). \tag{2.135}$$

Finally, using (2.135) in (2.127) gives

$$\varepsilon_{mq} \approx D - R\cos\left(\alpha_M^{(m)}\right) - (1.5 - q)\delta_B\left((R/D)\sin\left(\theta_B\right)\sin\left(\alpha_M^{(m)}\right) - \cos\left(\theta_B\right)\right). \tag{2.136}$$

Substituting (2.136) into (2.126) gives the result

$$
g_q(t) = \sum_{m=1}^{N} C_m e^{j\phi_m + j2\pi f_m t \cos\left(\alpha_{\mathrm{M}}^{(m)} - \gamma_{\mathrm{M}}\right)}
$$

$$
\times e^{-j2\pi\left(R + D - R\cos\left(\alpha_{\mathrm{M}}^{(m)}\right) - (1.5-q)\delta_{\mathrm{B}}\left((R/D)\sin(\theta_{\mathrm{B}})\sin\left(\alpha_{\mathrm{M}}^{(m)}\right) - \cos(\theta_{\mathrm{B}})\right)\right)/\lambda_{\mathrm{c}}},
$$
(2.137)

which is a function of the azimuth angle of departure $\alpha_{\mathrm{M}}^{(m)}$.

The space–time correlation function between the two complex faded envelopes $g_1(t)$ and $g_2(t)$ at the BS is once again given by (2.122). Using (2.137) and (2.122), the space–time correlation function between $g_1(t)$ and $g_2(t)$ can be written as follows:

$$
\phi_{g_1,g_2}(\delta_{\mathrm{B}}, \tau) = \frac{\Omega_{\mathrm{p}}}{2N} \sum_{m=1}^{N} \mathrm{E}\left[e^{j2\pi(\delta_{\mathrm{B}}/\lambda_{\mathrm{c}})\left((R/D)\sin(\theta_{\mathrm{B}})\sin\left(\alpha_{\mathrm{M}}^{(m)}\right) - \cos(\theta_{\mathrm{B}})\right)} \right.
$$

$$
\left. \times e^{-j2\pi f_m \tau \cos\left(\alpha_{\mathrm{M}}^{(m)} - \gamma_{\mathrm{M}}\right)} \right].
$$
(2.138)

Since the number of scatters around the MS is infinite, the discrete angles-of-arrival $\alpha_{\mathrm{M}}^{(m)}$ can be replaced with a continuous random variable α_{M} with probability density function $p(\alpha_{\mathrm{M}})$. Hence, the space–time correlation function becomes

$$
\phi_{g_1,g_2}(\delta_{\mathrm{B}}, \tau) = \frac{\Omega_{\mathrm{p}}}{2} \int_{-\pi}^{\pi} e^{-ja\cos(\alpha_{\mathrm{M}} - \gamma_{\mathrm{M}})} e^{jb((R/D)\sin(\theta_{\mathrm{B}})\sin(\alpha_{\mathrm{M}}) - \cos(\theta_{\mathrm{B}}))} p(\alpha_{\mathrm{M}}) d\alpha_{\mathrm{M}},
$$
(2.139)

where $a = 2\pi f_{\mathrm{m}}\tau$ and $b = 2\pi\delta_{\mathrm{B}}/\lambda_{\mathrm{c}}$.

For the case of 2D isotropic scattering with an isotropic MS transmit antenna, $p(\alpha_{\mathrm{M}}) = 1/(2\pi), -\pi \le \alpha_{\mathrm{M}} \le \pi$, and the space–time correlation function becomes

$$
\phi_{g_1,g_2}(\delta_{\mathrm{B}}, \tau) = \frac{\Omega_{\mathrm{p}}}{2} e^{-jb\cos(\theta_{\mathrm{B}})}
$$

$$
\times J_0\left(\sqrt{a^2 + b^2(R/D)^2 \sin^2(\theta_{\mathrm{B}}) - 2ab(R/D)\sin(\theta_{\mathrm{B}})\sin(\gamma_{\mathrm{M}})} \right).
$$
(2.140)

The spatial and temporal correlation functions can be obtained by setting $\tau = 0$ and $\delta_{\mathrm{B}} = 0$, respectively. For the temporal correlation function $\phi_{gg}(\tau) = \phi_{g_1,g_2}(0, \tau) = \frac{\Omega_{\mathrm{p}}}{2} J_0(2\pi f_{\mathrm{m}}\tau)$ which matches our earlier result in (2.26) as expected. The spatial correlation function is

$$
\phi_{g_1,g_2}(\delta_{\mathrm{B}}) = \phi_{g_1,g_2}(\delta_{\mathrm{B}}, 0) = \frac{\Omega_{\mathrm{p}}}{2} e^{-jb\cos(\theta_{\mathrm{B}})} J_0\left(b(R/D)\sin(\theta_{\mathrm{B}}) \right).
$$
(2.141)
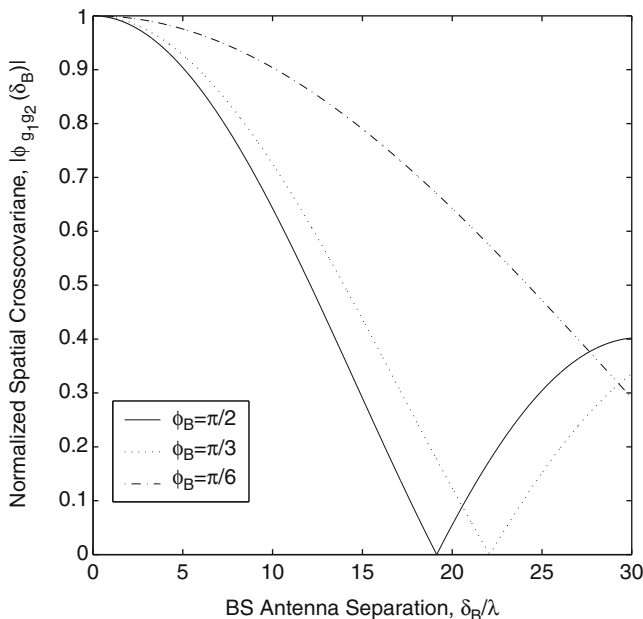
Fig. 2.21 Envelope cross-correlation magnitude at the base station for $R = 60\,\text{m}$ and various arrival angles, θ_B; $D = 3,000\,\text{m}$

Figure 2.21 plots the magnitude of the normalized spatial envelope cross-covariance function, $|\phi_{g_1,g_2}(\delta_B)|/(\Omega_p/2)$, for $R = 60\,\text{m}$ and various BS array orientation angles θ_B. Likewise, Fig. 2.22 plots $|\phi_{g_1,g_2}(\delta_B)|/(\Omega_p/2)$ for $\theta_B = \pi/3$ and various scattering radii, R. In general, we observe that a much greater spatial separation is required to achieve a given degree of envelope decorrelation at the BS as compared to the MS. This can be readily seen by the term $R/D \ll 1$ in the argument of the Bessel function in (2.141). Also, the spatial correlation increases as the angle θ_B and scattering radii R decrease. BS antenna arrays that are broadside with the MS direction will experience the lowest correlation, while those that are in-line with the MS direction will experience the highest correlation. In fact, for in-line antennas we have $|\phi_{g_1,g_2}(\delta_B)| = 1$.

2.2 Mobile-to-Mobile Channels

Mobile-to-mobile (M-to-M) communication channels arise when both the transmitter and receiver are in motion and are equipped with low elevation antennas that are surrounded by local scatterers. The statistical properties of M-to-M channels differ significantly from those of conventional F-to-M cellular land mobile radio channels, where the mobile station is surrounded by local scatterers and the base
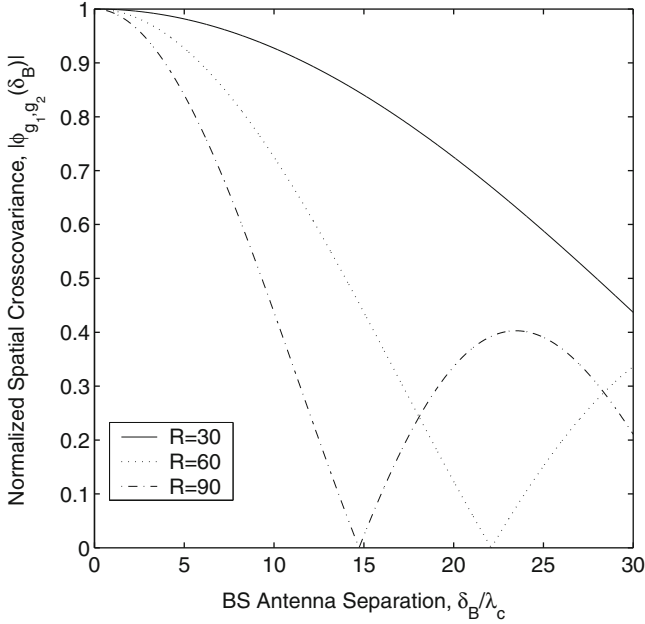
Fig. 2.22 Envelope cross-correlation magnitude at the base station for $\theta_B = \pi/3$ and various scattering radii, R; $D = 3,000\,\mathrm{m}$

station is stationary, elevated, and relatively free of local scattering. Akki and Haber [9, 10] were the first to propose a mathematical reference model for M-to-M flat fading channels under NLoS propagation conditions. The Akki and Haber model was extended by Vatalaro and Forcella [262] to account for 3D scattering, and by Linnartz and Fiesta [161] to include LoS propagation conditions. Channel measurements for outdoor-to-outdoor, narrow-band outdoor-to-indoor, and wide-band mobile-to-mobile communications have been reported in [7, 143, 146, 175], and methods for simulating M-to-M channels have been proposed in [204, 277, 301].

2.2.1 *Mobile-to-Mobile Reference Model*

Akki and Haber's mathematical reference model for M-to-M flat fading channels gives the complex faded envelope as [10]

$$g(t) = \sqrt{\frac{1}{N}} \sum_{n=1}^{N} e^{j2\pi \left(f_m^T \cos\left(\alpha_T^{(n)}\right) + f_m^R \cos\left(\alpha_R^{(n)}\right) \right) t + j\phi_n}, \tag{2.142}$$

where N is the number of propagation paths; f_m^T and f_m^R are the maximum Doppler frequencies due to the motion of the transmitter and receiver, respectively; $\alpha_T^{(n)}$ is the random angle of departure and $\alpha_R^{(n)}$ is the random AoA of the nth propagation path measured with respect to the transmitter and receiver velocity vectors, respectively; ϕ_n is a random phase uniformly distributed on $[-\pi, \pi)$ independent of $\alpha_T^{(n)}$ and $\alpha_R^{(n)}$ for all n.

In the above model, the Doppler frequency experienced by each propagation path is the sum of the individual Doppler frequencies induced by the motion of the transmitter and receiver. Once again, for sufficiently large N, the central limit theorem can be invoked with the result that $g_I(t)$ and $g_Q(t)$ can be treated as zero-mean Gaussian random processes. If we assume omnidirectional transmitter and receiver antennas and 2D isotropic scattering around both the transmitter and receiver, then the envelope $|g(t)|$ is Rayleigh distributed at any time t. This is similar to the case of conventional fixed to mobile cellular land mobile radio channels with 2D isotropic scattering and an isotropic antenna at the MS. However, the ensemble averaged temporal correlation functions of the faded envelope are quite different and are as follows [9, 10]:

$$\phi_{g_I g_I}(\tau) = \frac{1}{2} J_0(2\pi f_m^T \tau) J_0(2\pi a f_m^T \tau),$$

$$\phi_{g_Q g_Q}(\tau) = \frac{1}{2} J_0(2\pi f_m^T \tau) J_0(2\pi a f_m^T \tau),$$

$$\phi_{g_I g_Q}(\tau) = \phi_{g_Q g_I}(\tau) = 0,$$

$$\phi_{gg}(\tau) = \frac{1}{2} J_0(2\pi f_m^T \tau) J_0(2\pi a f_m^T \tau), \tag{2.143}$$

where $a = f_m^R / f_m^T$ is the ratio of the two maximum Doppler frequencies (or speeds) of the receiver and transmitter, and $0 \le a \le 1$ assuming $f_m^R \le f_m^T$. Observe that the temporal correlation functions of M-to-M channels involve a product of two Bessel functions in contrast to the single Bessel function found in F-to-M channels. Also, $a = 0$ yields the temporal correlation functions for F-to-M channels as expected. The corresponding Doppler spectrum obtained by taking the Fourier transform of (2.143) is

$$S_{gg}(f) = \frac{1}{\pi^2 f_m^T \sqrt{a}} K \left(\frac{1+a}{2\sqrt{a}} \sqrt{1 - \left(\frac{f}{(1+a) f_m^T} \right)^2} \right), \tag{2.144}$$

where $K(\,\cdot\,)$ is the complete elliptic integral of the first kind. The Doppler spectrum of M-to-M channels in (2.144) differs from the classical spectrum of F-to-M cellular land mobile radio channels, as illustrated in Fig. 2.23, which shows the Doppler spectrum for different values of a.
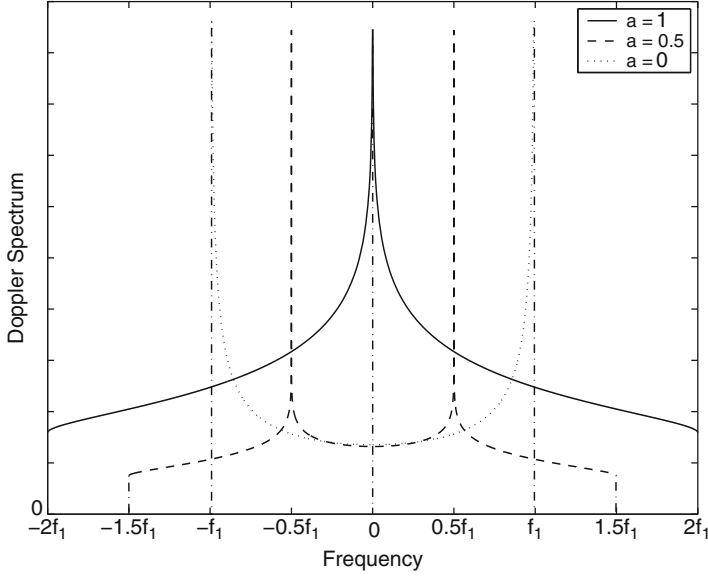
Fig. 2.23 Doppler spectrum for M-to-M and F-to-M channels

2.3 MIMO Channels

An MIMO system is one that consists, for example, of multiple transmit and receive antennas as shown in Fig 2.24. For a system consisting of L_T transmit and L_R receive antennas, the channel can be described by the $L_T \times L_R$ matrix

$$\mathbf{G}(t,\tau) = \begin{bmatrix} g_{1,1}(t,\tau) & g_{1,2}(t,\tau) & \cdots & g_{1,L_T}(t,\tau) \\ g_{2,1}(t,\tau) & g_{2,2}(t,\tau) & \cdots & g_{2,L_T}(t,\tau) \\ \vdots & \vdots & & \vdots \\ g_{L_R,1}(t,\tau) & g_{L_R,2}(t,\tau) & \cdots & g_{L_R,L_T}(t,\tau) \end{bmatrix}, \tag{2.145}$$

where $g_{qp}(t,\tau)$ denotes the time-varying sub-channel impulse response between the pth transmit antenna and qth receive antenna.

Suppose that the complex envelopes of the signals transmitted from the L_T transmit antennas are described by the vector

$$\tilde{\mathbf{s}}(t) = (\tilde{s}_1(t), \tilde{s}_2(t), \ldots, \tilde{s}_{L_T}(t))^T, \tag{2.146}$$

where $\tilde{s}_p(t)$ is the signal transmitted from the pth transmit antenna. Likewise, let

$$\tilde{\mathbf{r}}(t) = (\tilde{r}_1(t), \tilde{r}_2(t), \ldots, \tilde{r}_{L_R}(t))^T, \tag{2.147}$$
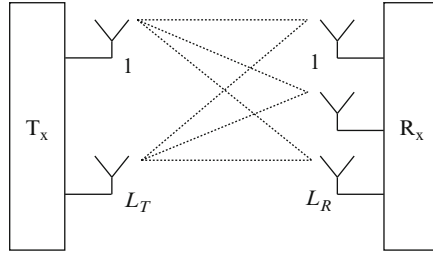
Fig. 2.24 MIMO system with multiple transmit and multiple receive antennas

denote the vector of received complex envelopes, where $\tilde{r}_q(t)$ is the signal received at the qth receiver antenna. Then

$$\tilde{\mathbf{r}}(t) = \int_0^t \mathbf{G}(t,\tau)\tilde{\mathbf{s}}(t-\tau)\mathrm{d}\tau. \tag{2.148}$$

Under conditions of flat fading

$$\mathbf{G}(t,\tau) = \mathbf{G}(t)\delta(\tau - \hat{\tau}), \tag{2.149}$$

where $\hat{\tau}$ is the delay through the channel and

$$\tilde{\mathbf{r}}(t) = \mathbf{G}(t)\tilde{\mathbf{s}}(t - \hat{\tau}). \tag{2.150}$$

If the MIMO channel is characterized by slow fading, then

$$\tilde{\mathbf{r}}(t) = \int_0^t \mathbf{G}(\tau)\tilde{\mathbf{s}}(t-\tau)\mathrm{d}\tau. \tag{2.151}$$

In this case, the channel matrix $\mathbf{G}(\tau)$ remains constant over the duration of the transmitted waveform $\tilde{\mathbf{s}}(t)$, but can vary from one channel use to the next, where a channel use may be defined as the transmission of either a single modulated symbol or a vector of modulated symbols from each antenna. In the case of a vector of modulated symbols, this type of channel is sometimes called a quasi-static fading channel or a block fading channel. Finally, if the MIMO channel is characterized by slow flat fading, then

$$\tilde{\mathbf{r}}(t) = \mathbf{G}\tilde{\mathbf{s}}(t). \tag{2.152}$$

MIMO channel models can be classified as either *physical* or *analytical* models. Physical MIMO models characterize the channel on the basis of electromagnetic wave propagation between the transmitter and receiver antennas. Such physical channel models can be further classified as deterministic models, geometry-based stochastic models, and nongeometric stochastic models. Deterministic models construct the MIMO channel in a completely deterministic manner, such as ray

tracing and stored measurement data. With geometry-based stochastic models, the time-variant MIMO channel impulse response is generated by applying the laws of wave propagation to specific transmitter, receiver, and scattering geometries, which are generated in a stochastic or random fashion [302–304]. The nongeometric stochastic models determine physical parameters such as the angles of departure and angles of arrival in a completely stochastic fashion by prescribing underlying probability density functions, but not using an underlying geometry. These models include the extended Saleh–Valenzuela models [53, 272].

The MIMO analytical models characterize the MIMO sub-channel impulse responses in a mathematical manner without explicitly considering the underlying electromagnetic wave propagation. Analytic models can be further classified as propagation motivated models or correlation-based models. Propagation motivated models include the finite scattering models [40], maximum entropy models [75], and virtual channel representation [233]. Correlation-based models generate random realizations of the channel matrix with specified correlations between the matrix elements [140, 281]. These models are easy to implement, which has made them very popular for MIMO channel simulations. Moreover, the analytical models are relatively easy to understand and so we treat them here.

2.3.1   Analytical MIMO Channel Models

Analytical MIMO channel models are most often used under quasi-static flat fading conditions. We have seen earlier that the time-variant channel impulses for flat fading channels can be treated as complex Gaussian random processes under conditions of Rayleigh and Ricean fading. The various analytical models generate the MIMO matrices as realizations of complex Gaussian random variables having specified means and correlations. To model Ricean fading, the channel matrix can be divided into a deterministic part and a random part, that is,

$$\mathbf{G} = \sqrt{\frac{K}{K+1}}\bar{\mathbf{G}} + \sqrt{\frac{1}{K+1}}\mathbf{G}_{\mathrm{s}}, \qquad (2.153)$$

where $\mathrm{E}[\mathbf{G}] = \sqrt{\frac{K}{K+1}}\bar{\mathbf{G}}$ is the LoS or specular component and $\sqrt{\frac{K}{K+1}}\mathbf{G}_{\mathrm{s}}$ is the scatter component assumed to have zero-mean. The elements of the matrices $\bar{\mathbf{G}}$ and $\mathbf{G}_{\mathrm{s}}$ are normalized to have power Ω_{p}, so that the elements of matrix $\mathbf{G}$ have power Ω_{p}, that is, $\mathrm{E}[|g_{pq}|^2] = \Omega_{\mathrm{p}}$. In this case, K represents the Rice factor, defined as the ratio of the power in the LoS or specular component to the power in the scatter component.

To simply our further treatment of the MIMO channel, assume for the time being that $K = 0$, so that $\mathbf{G} = \mathbf{G}_{\mathrm{s}}$. The simplest MIMO model assumes that the entries of the matrix $\mathbf{G}$ are independent and identically distributed (i.i.d) complex Gaussian random variables. This model corresponds to the so-called rich scattering or spatially white environment. Such an independence assumption simplifies the

performance analysis of various digital signaling schemes operating on MIMO channels. However, in reality the sub-channels will be correlated and, therefore, the i.i.d. model will lead to optimistic results.

A variety of more sophisticate models have been introduced to account for spatial correlation of the sub-channels. Consider the vector $\mathbf{g} = \text{vec}\{\mathbf{G}\}$, where $\mathbf{G} = [\mathbf{g}_1, \mathbf{g}_2, \ldots, \mathbf{g}_{L_T}]$ and $\text{vec}\{\mathbf{G}\} = [\mathbf{g}_1^T, \mathbf{g}_2^T, \ldots, \mathbf{g}_{L_T}^T]^T$. The vector $\mathbf{g}$ is a column vector of length $n = L_T L_R$. The vector $\mathbf{g}$ is zero-mean complex Gaussian random vector and its statistics are fully specified by the $n \times n$ covariance matrix $\mathbf{R}_G = \frac{1}{2}\text{E}[\mathbf{g}\mathbf{g}^H]$. Hence, $\mathbf{g} \sim \mathscr{CN}(\mathbf{0}, \mathbf{R}_G)$ and, if $\mathbf{R}_G$ is invertible, the probability density function of $\mathbf{g}$ is

$$p(\mathbf{g}) = \frac{1}{(2\pi)^n \det(\mathbf{R}_G)} e^{-\frac{1}{2}\mathbf{g}^H \mathbf{R}_G^{-1}\mathbf{g}}, \quad \mathbf{g} \in \mathscr{C}^n. \tag{2.154}$$

Realizations of the MIMO channel with the distribution in (2.154) can be generated by

$$\mathbf{G} = \text{unvec}\{\mathbf{g}\} \quad \text{with} \quad \mathbf{g} = \mathbf{R}_G^{1/2}\mathbf{w}. \tag{2.155}$$

Here, $\mathbf{R}_G^{1/2}$ is any matrix square root of $\mathbf{R}_G$, that is, $\mathbf{R}_G = \mathbf{R}_G^{1/2}(\mathbf{R}_G^{1/2})^H$, and $\mathbf{w}$ is a length n vector where $\mathbf{w} \sim \mathscr{CN}(\mathbf{0}, \mathbf{I})$.

2.3.1.1 Kronecker Model

The Kronecker model [140] constructs the MIMO channel matrix $\mathbf{G}$ under the assumption that the spatial correlation at the transmitter and receiver is separable. This is equivalent to restricting the correlation matrix $\mathbf{R}_G$ to have the Kronecker product form

$$\mathbf{R}_G = \mathbf{R}_T \otimes \mathbf{R}_R, \tag{2.156}$$

where

$$\mathbf{R}_T = \frac{1}{\sqrt{2}}\text{E}[\mathbf{G}^H \mathbf{G}] \qquad \mathbf{R}_R = \frac{1}{\sqrt{2}}\text{E}[\mathbf{G}\mathbf{G}^H]. \tag{2.157}$$

are the $L_T \times L_T$ and $L_R \times L_R$ transmit and receive correlation matrices, respectively, and $\otimes$ is the Kronecker product. For example, the Kronecker product of an $n \times n$ matrix $\mathbf{A}$ and an $m \times m$ matrix $\mathbf{B}$ would be

$$\mathbf{A} \otimes \mathbf{B} = \begin{bmatrix} a_{11}\mathbf{B} & \cdots & a_{1n}\mathbf{B} \\ a_{n1}\mathbf{B} & \cdots & a_{nn}\mathbf{B} \end{bmatrix}. \tag{2.158}$$

Under the above Kronecker assumption, (2.155) simplifies to the Kronecker model

$$\mathbf{g} = (\mathbf{R}_T \otimes \mathbf{R}_R)^{1/2}\mathbf{w} \tag{2.159}$$

and

$$\mathbf{G} = \mathbf{R}_R^{1/2}\mathbf{W}\mathbf{R}_T^{1/2}, \tag{2.160}$$

where $\mathbf{W}$ is an $L_R \times L_T$ matrix consisting of i.i.d. zero mean complex Gaussian random variables.

The elements of the matrix $\mathbf{G}$ represent correlations between the faded envelopes of the MIMO sub-channels. If the elements of $\mathbf{G}$ could be arbitrarily selected, then the correlation functions would be a function of four sub-channel index parameters, that is,

$$\frac{1}{2}\mathrm{E}[g_{qp}g_{\tilde{q}\tilde{p}}^*] = \phi(q, p, \tilde{q}, \tilde{p}), \qquad (2.161)$$

where g_{qp} is the channel between the pth transmit and qth receive antenna. However, due to the Kronecker property in (2.156), the elements of $\mathbf{G}$ are structured. One implication of the Kronecker property is spatial stationarity

$$\frac{1}{2}\mathrm{E}[g_{qp}g_{\tilde{q}\tilde{p}}^*] = \phi(q - \tilde{q}, p - \tilde{p}). \qquad (2.162)$$

This implies that the sub-channel correlations are determined not by their position in the matrix $\mathbf{G}$, but by their difference in position. In addition to the stationary property, manipulation of the Kronecker product form in (2.156) implies that

$$\frac{1}{2}\mathrm{E}[g_{qp}g_{\tilde{q}\tilde{p}}^*] = \phi_T(p - \tilde{p}) \cdot \phi_R(q - \tilde{q}). \qquad (2.163)$$

This means that the correlation can be separated into two parts: a transmitter part and a receiver part, and both parts are stationary. Finally, we note that the Kronecker property in (2.156) holds if and only if the separable property in (2.163) holds. Later in our discussion of physical models, we will show that the separable property is satisfied by double-bounced channels such as the double ring model in Fig. 2.44, where the angles of arrival for each ray at the receiver are independent of the angles of departure at the transmitter.

2.3.1.2 Weichselberger Model

The Weichselberger model [281] overcomes the separable requirement of the channel correlation functions in (2.163) so as to include a broader range of MIMO channels. Its definition is based on an eigenvalue decomposition of the transmitter and receiver correlation matrices,

$$\mathbf{R}_T = \mathbf{U}_T \Lambda_T \mathbf{U}_T^H, \qquad (2.164)$$

$$\mathbf{R}_R = \mathbf{U}_R \Lambda_R \mathbf{U}_R^H. \qquad (2.165)$$

Here the matrices Λ_T and Λ_R are diagonal matrices containing the eigenvalues of, and $\mathbf{U}_T$ and $\mathbf{U}_R$ are unity matrices containing the eigenvectors of, $\mathbf{R}_T$ and $\mathbf{R}_R$, respectively. The Weichselberger model constructs the matrix $\mathbf{G}$ as

$$\mathbf{G} = \mathbf{U}_R \left(\tilde{\Omega} \odot \mathbf{W} \right) \mathbf{U}_T^T, \qquad (2.166)$$

where $\mathbf{W}$ is an $L_R \times L_T$ matrix consisting of i.i.d. zero mean complex Gaussian random variables and $\odot$ denotes the Schur–Hadmard product (element-wise matrix multiplication), and Ω is an $L_R \times L_T$ coupling matrix whose nonnegative real values determine the average power coupling between the transmitter and receiver eigenvectors. The matrix $\tilde{\Omega}$ is the element-wise square root of Ω. For validation of the Weichselberger model, the matrix Ω can be determined from measured data as

$$\Omega = \mathrm{E}_\mathbf{G}\left[(\mathbf{U}_R^H \mathbf{G} \mathbf{U}_T^*) \odot (\mathbf{U}_R^T \mathbf{G}^* \mathbf{U}_T)\right]. \tag{2.167}$$

Note that the Kronecker model is a special case of the Weichselberger model obtained with the coupling matrix $\Omega = \lambda_R \lambda_T^T$, where λ_R and λ_T are column vectors containing the eigenvalues of Λ_T and Λ_R, respectively.

2.4 Statistical Characterization of Multipath-Fading Channels

Multipath-fading channels can be modeled as randomly time-variant linear filters, whose inputs and outputs can be described in both the time and frequency-domains. This leads to four possible transmission functions [28]; the time-variant impulse response $g(\tau,t)$, the output Doppler-spread function $H(f,v)$, the time-variant transfer function $T(f,t)$, and the delay Doppler-spread function $S(\tau,v)$. The time-variant impulse response relates the complex low-pass input and output time waveforms, $\tilde{s}(t)$ and $\tilde{r}(t)$, respectively, through the convolution integral

$$\tilde{r}(t) = \int_0^t \tilde{s}(t-\tau)g(t,\tau)\mathrm{d}\tau. \tag{2.168}$$

In physical terms, $g(t,\tau)$ can be interpreted as the channel response at time t due to an impulse applied at time $t-\tau$. Since a physical channel is causal, $g(t,\tau) = 0$ for $\tau < 0$ and, therefore, the lower limit of integration in (2.168) is zero. If the convolution in (2.168) is approximated as a discrete sum, then

$$\tilde{r}(t) = \sum_{m=0}^n \tilde{s}(t-m\Delta\tau)g(t,m\Delta\tau)\Delta\tau. \tag{2.169}$$

This representation allows us to visualize the channel as a transversal filter with tap spacing $\Delta\tau$ and time-varying tap gains $g(t,m\Delta\tau)$ as shown in Fig. 2.25.

The second transmission function relates the input and output spectra, $\tilde{S}(f)$ and $\tilde{R}(f)$, respectively, through the integral equation

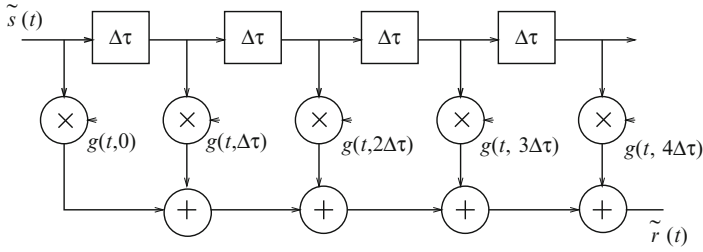$$\tilde{R}(f) = \int_{-\infty}^\infty \tilde{S}(f-v)H(f-v,v)\mathrm{d}v. \tag{2.170}$$

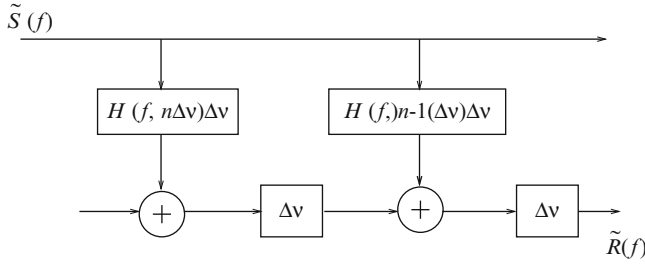**Fig. 2.25** Discrete-time tapped delay line model for a multipath-fading channel

Fig. 2.26 Frequency conversion model for a multipath-fading channel

Bello called the function $H(f,v)$ the output Doppler-spread function [28]. This function explicitly shows the effect of Doppler shift or spectral broadening on the output spectrum. In physical terms, the frequency-shift variable v can be interpreted as the Doppler shift that is introduced by the channel. Once again, the integral in (2.170) can be approximated by the discrete sum

$$\tilde{R}(f) = \sum_{m=-n}^{n} \tilde{S}(f - m\Delta v)H(f - m\Delta v, m\Delta v)\Delta v. \tag{2.171}$$

This allows the channel to be represented by a bank of filters with transfer functions $H(f, m\Delta v)\Delta v$ followed by a dense frequency conversion chain with tap spacing Δv that produces the Doppler shifts as shown in Fig. 2.26.

The third transmission function $T(f,t)$ is the familiar time-variant transfer function and relates the output time waveform to the input spectrum as follows:

$$\tilde{r}(t) = \int_{-\infty}^{\infty} \tilde{S}(f)T(f,t)e^{j2\pi ft}df. \tag{2.172}$$

The final description relates the input and output time waveforms through the double integral

$$\tilde{r}(t) = \int_{-\infty}^{\infty}\int_{-\infty}^{\infty} \tilde{s}(t-\tau)S(\tau,v)e^{j2\pi f\tau}dvd\tau. \tag{2.173}$$

Fig. 2.27 Fourier transform relations between the transmission functions
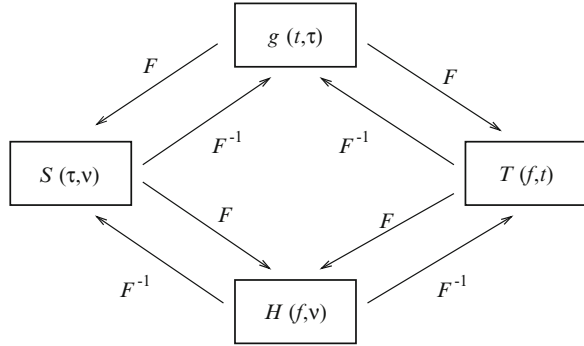
The function $S(\tau, \nu)$ is called the delay Doppler-spread function [28] and provides a measure of the scattering amplitude of the channel in terms of the time delay τ and Doppler frequency ν.

The four transmission functions are related to each other through Fourier transform pairs as shown in Fig. 2.27. In each transform pair there is always a fixed variable, so that the transform involves the other two variables.

2.4.1   Statistical Channel Correlation Functions

Similar to flat fading channels, the channel impulse response $g(t, \tau) = g_I(t, \tau) + jg_Q(t, \tau)$ of a frequency-selective fading channel can be modeled as a complex Gaussian random process, where the quadrature components $g_I(t, \tau)$ and $g_Q(t, \tau)$ are real Gaussian random processes. Hence, all of the transmission functions defined in the last section are themselves random processes. Since the underlying process is Gaussian, a complete statistical description of these transmission functions is provided by their means and autocorrelation functions. In the following discussion, we assume zero-mean Gaussian random processes for simplicity so that only the autocorrelation functions are of interest. Since there are four transmission functions, four autocorrelation functions can be defined as follows [201, 217]:
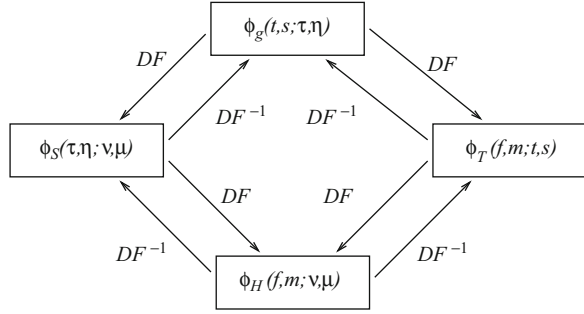
$$\phi_g(t, s; \tau, \eta) = \frac{1}{2}\mathrm{E}[g(t, \tau)g^*(s, \eta)], \tag{2.174}$$

$$\phi_T(f, m; t, s) = \frac{1}{2}\mathrm{E}[T(f, t)T^*(m, s)], \tag{2.175}$$

$$\phi_H(f, m; \nu, \mu) = \frac{1}{2}\mathrm{E}[H(f, \nu)H^*(m, \mu)], \tag{2.176}$$

$$\phi_S(\tau, \eta; \nu, \mu) = \frac{1}{2}\mathrm{E}[S(\tau, \nu)S^*(\eta, \mu)]. \tag{2.177}$$

Fig. 2.28 Double Fourier transform relations between the channel autocorrelation functions

These autocorrelation functions are related to each other through double Fourier transform pairs. For example,

$$\phi_S(\tau,\eta;\nu,\mu) = \int_{-\infty}^{\infty}\int_{-\infty}^{\infty} \phi_g(t,s;\tau,\eta)e^{-j2\pi(\nu t - \mu s)}\,dt\,ds, \qquad (2.178)$$

$$\phi_g(t,s;\tau,\eta) = \int_{-\infty}^{\infty}\int_{-\infty}^{\infty} \phi_S(\tau,\eta;\nu,\mu)e^{j2\pi(\nu t - \mu s)}\,d\nu\,d\mu. \qquad (2.179)$$

The complete set of such relationships is summarized in Fig. 2.28.

2.4.2 Classification of Channels

WSS channels have fading statistics that remain constant over small periods of time or short spatial distances. This implies that the channel correlation functions depend on the time variables t and s only through the time difference $\Delta t = s - t$. It can be demonstrated (see Problem 2.19) that WSS channels give rise to scattering with uncorrelated Doppler shifts. This behavior suggests that the attenuations and phase shifts associated with multipath components having different Doppler shifts are uncorrelated. This makes sense because multipath components with different Doppler shifts arrive from different directions and, hence, propagate via different sets of scatterers. For WSS channels, the correlation functions become

$$\phi_g(t,t+\Delta t;\tau,\eta) = \phi_g(\Delta t;\tau,\eta), \qquad (2.180)$$

$$\phi_T(f,m;t,t+\Delta t) = \phi_T(f,m;\Delta t), \qquad (2.181)$$

$$\phi_H(f,m;\nu,\mu) = \psi_H(f,m;\nu)\delta(\nu-\mu), \qquad (2.182)$$

$$\phi_S(\tau,\eta;\nu,\mu) = \psi_S(\tau,\eta;\nu)\delta(\nu-\mu), \qquad (2.183)$$

where

$$\psi_H(f,m;v) = \int_{-\infty}^{\infty} \phi_T(f,m;\Delta t)e^{-j2\pi v\Delta t}d\Delta t, \tag{2.184}$$

$$\psi_S(\tau,\eta;v) = \int_{-\infty}^{\infty} \phi_c(\Delta t;\tau,\eta)e^{-j2\pi v\Delta t}d\Delta t \tag{2.185}$$

are Fourier transform pairs.

Uncorrelated scattering (US) channels   are characterized by an uncorrelated complex gain with paths of different delays. Bello showed that US channels are WSS in the frequency variable so that the correlation functions depend on the frequency variables f and m only through the frequency difference $\Delta f = m - f$ [28]. Analogous to (2.182) and (2.183), the channel correlation functions are singular in the time-delay variable (see Problem 2.20). Again, this makes sense because multipath components arriving with different delays propagate via different sets of scatterers. For US channels, the channel correlation functions become

$$\phi_g(t,s;\tau,\eta) = \psi_g(t,s;\tau)\delta(\eta - \tau), \tag{2.186}$$

$$\phi_T(f,f+\Delta f;t,s) = \phi_T(\Delta f;t,s), \tag{2.187}$$

$$\phi_H(f,f+\Delta f;v,\mu) = \phi_H(\Delta f;v,\mu), \tag{2.188}$$

$$\phi_S(\tau,\eta;v,\mu) = \psi_S(\tau;v,\mu)\delta(\eta - \tau), \tag{2.189}$$

where

$$\psi_g(t,s;\tau) = \int_{-\infty}^{\infty} \phi_T(\Delta f;t,s)e^{j2\pi\Delta f\tau}d\Delta f, \tag{2.190}$$

$$\psi_S(\tau;v,\mu) = \int_{-\infty}^{\infty} \phi_H(\Delta f;v,\mu)e^{j2\pi\Delta f\tau}d\Delta f \tag{2.191}$$

are Fourier transform pairs.

WSS uncorrelated scattering (WSSUS) channels   exhibit uncorrelated scattering in both the time-delay and Doppler shift. Fortunately, many radio channels can be effectively modeled as WSSUS channels. For WSSUS channels, the correlation functions have singular behavior in both the time delay and Doppler shift variables, and reduce to the following simple forms:

$$\phi_g(t,t+\Delta t;\tau,\eta) = \psi_g(\Delta t;\tau)\delta(\eta - \tau), \tag{2.192}$$

$$\phi_T(f,f+\Delta f;t,t+\Delta t) = \phi_T(\Delta f;\Delta t), \tag{2.193}$$

$$\phi_H(f,f+\Delta f;v,\mu) = \psi_H(\Delta f;v)\delta(v - \mu), \tag{2.194}$$

$$\phi_S(\tau,\eta;v,\mu) = \psi_S(\tau,v)\delta(\eta - \tau)\delta(v - \mu). \tag{2.195}$$

The correlation functions for WSSUS channels are related through the Fourier transform pairs shown in Fig. 2.29.

Fig. 2.29 Fourier transform
relations between the channel
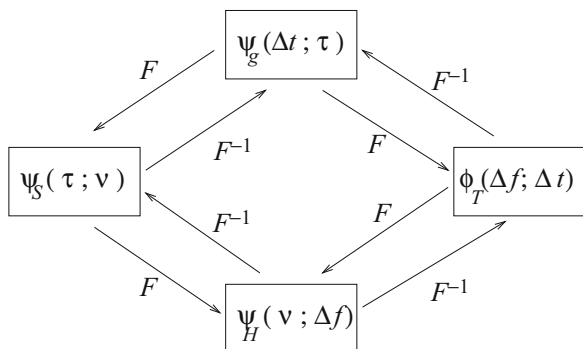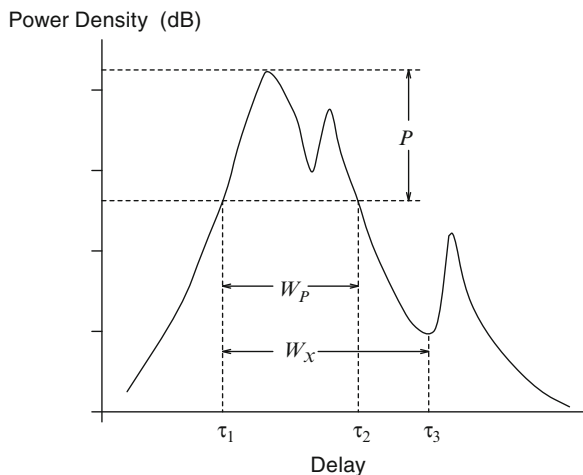correlation functions for
WSSUS channels

Fig. 2.30 A typical
power-delay profile

2.4.3 Power Delay Profile and Coherence Bandwidth

The function $\psi_g(0;\tau) \equiv \psi_g(\tau)$ is called the power-delay profile and gives the
average power at the channel output as a function of the time delay τ. A typical
power-delay profile is shown in Fig. 2.30. One quantity of interest is the average
delay, defined as

$$\mu_\tau = \frac{\int_0^\infty \tau \psi_g(\tau) d\tau}{\int_0^\infty \psi_g(\tau) d\tau}. \tag{2.196}$$

Note that the normalization $\int_0^\infty \psi_g(\tau)d\tau$ is applied because $\psi_g(\tau)$ does not necessar-
ily integrate to unity like a probability density function. Another quantity of interest
is the rms delay spread, defined as

$$\sigma_\tau = \sqrt{\frac{\int_0^\infty (\tau - \mu_\tau)^2 \psi_g(\tau) d\tau}{\int_0^\infty \psi_g(\tau) d\tau}}. \tag{2.197}$$

There are other quantities that can also be used to describe the power-delay profile. One is the width, W_x, of the middle portion of the power-delay profile that contains a fraction x of the total power in the profile. Referring to Fig. 2.30

$$W_x = \tau_3 - \tau_1, \tag{2.198}$$

where τ_1 and τ_3 are chosen so that

$$\int_0^{\tau_1} \psi_g(\tau)d\tau = \int_{\tau_3}^{\infty} \psi_g(\tau)d\tau \tag{2.199}$$

and

$$\int_{\tau_1}^{\tau_3} \psi_g(\tau)d\tau = x \int_0^{\infty} \psi_g(\tau)d\tau. \tag{2.200}$$

Another quantity is the difference in delays where the power-delay profile rises to a value P dB below its maximum value for the first time and where the power-delay profile drops to a value P dB below its maximum value for the last time. This quantity is denoted by W_P and is also illustrated in Fig. 2.30, where $W_P = \tau_2 - \tau_1$. In general, the average delay and delay spread of the channel will diminish with decreasing cell size, the reason being that the radio path lengths are shorter. While the delay spread in a typical macrocellular application may be on the order of 1–$10\,\mu$s, the delay spreads in a typical microcellular applications are much less. Delay spreads for indoor channels can range anywhere from 30 to 60 ns in buildings with interior walls and little metal, to 300 ns in buildings with open plans and a significant amount of metal.

The function $\phi_T(\Delta t;\Delta f)$ is called the spaced-time spaced-frequency correlation function. The function $\phi_T(0;\Delta f) \equiv \phi_T(\Delta f)$ measures the frequency correlation of the channel. The coherence bandwidth, B_c, of the channel is defined as the smallest value of Δf for which $\phi_T(\Delta f) = x\phi_T(0)$ for some suitably small value of $x, 0 < x < 1$. As a result of the Fourier transform relation between $\phi_g(\tau)$ and $\phi_T(\Delta f)$, the reciprocal of either the average delay or the delay spread is a measure of the coherence bandwidth of the channel. That is,

$$B_c \propto \frac{1}{\mu_\tau} \quad \text{or} \quad B_c \propto \frac{1}{\sigma_\tau}. \tag{2.201}$$

Wideband fading channels can be classified according to the relationship between the transmitted signal bandwidth W_s and the coherence bandwidth B_c. If $B_c < W_s$, the channel is said to exhibit frequency selective fading which introduces intersymbol interference (ISI) into the received signal. If $B_c \gg W_s$, the channel is said to exhibit flat fading, and very little ISI is introduced into the received signal.

The function $\phi_H(v;0) \equiv \phi_H(v)$ is identical to the Doppler spectrum $S_{gg}(f)$ (2.30), that is, $\phi_H(v) \equiv S_{gg}(f)$, and gives the average power at the channel output

as a function of the Doppler frequency ν. The range of values over which $\phi_H(\nu)$ is significant is called the Doppler spread and is denoted by B_d. Since $\phi_H(\nu)$ and $\phi_T(\Delta t)$ are a Fourier transform pair, it follows that the inverse of the Doppler spread gives a measure of the channel coherence time, T_c, that is,

$$T_c \approx \frac{1}{B_d}. \tag{2.202}$$

Wideband fading channels can also be classified according to the relationship between the transmitted symbol duration, T, and the coherence time T_c. If $T_c < T$, the channel is said to exhibit fast fading which introduces severe frequency dispersion into the received signal. If $T_c \gg T$, the channel is said to exhibit the very common case of slow fading which introduces very little frequency dispersion into the received signal.

Finally, the function $\psi_S(\tau, \nu)$ is called the scattering function and gives the average power output of the channel as a function of the time delay τ and the Doppler shift ν. Plots of the scattering function are often used to provide a concise statistical description of a multipath-fading channel from measurement data.

2.5 Simulation of Multipath-Fading Channels

A channel simulator is an essential component for the development and testing of wireless systems. Simulation of mobile radio channels is commonly used as opposed to field trials, because it allows for less expensive and more reproducible system tests and evaluations. For this purpose, it is desirable to generate complex faded envelopes that match the statistical characteristics of a reference model while at the same time having low complexity. For example, the reference model might be a 2D isotropic scattering channel with an isotropic antenna.

Two fundamentally different approaches to channel simulation models are the filtered white Gaussian noise models and the sum-of-sinusoids (SoS) models. The basic idea of the filtered-based approach is to shape the power spectrum of a white Gaussian noise process using a filter having a transfer function that is the square root of the power density spectrum of the desired random process. The sum of sinusoids approach, on the other hand, approximates the complex fading envelope by the superposition of a finite number of sinusoids with properly chosen amplitudes, frequencies, and phases.

2.5.1 Filtered White Gaussian Noise Models

Recall that the faded envelope $g(t) = g_I(t) + jg_Q(t)$ is a complex Gaussian random process. A straightforward method for constructing a fading simulator is to low-pass filter two independent white Gaussian noise processes, as shown in Fig. 2.31.
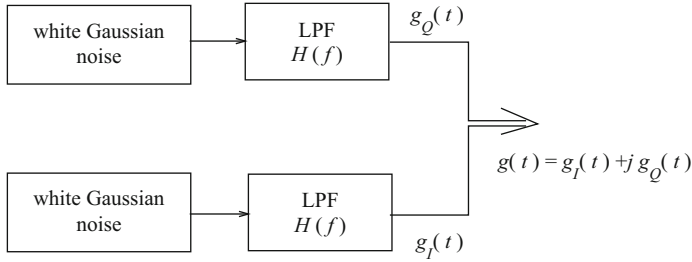
Fig. 2.31 Fading simulator that uses low-pass filtered white Gaussian noise

Since the input processes to the filters are independent, the random processes $g_I(t)$ and $g_Q(t)$ are independent and have power spectral densities that are determined by the squared magnitude response of the low-pass filters. If the white Gaussian noise sources have power spectral densities equal to $\Omega_p/2$ W/Hz and the low-pass filters have transfer function $H(f)$, then

$$S_{g_I g_I}(f) = S_{g_Q g_Q}(f) = \frac{\Omega_p}{2}|H(f)|^2,$$
$$S_{g_I g_Q}(f) = 0, \tag{2.203}$$

where the normalization $\int_{-\infty}^{\infty} |H(f)|^2 \mathrm{d}f = 1$ is assumed so that the envelope power is equal to Ω_p. The filtered white noise processes $g_I(t)$ and $g_Q(t)$ are independent zero-mean Gaussian random process, so that the envelope $\alpha \equiv |g(t_1)|$ is Rayleigh distributed at any time t_1.

2.5.1.1 IDFT Method

One approach for generating the faded envelope using the filtering method has been suggested by Young & Beaulieu [298] and is based on an inverse discrete Fourier transform (IDFT) as shown in Fig. 2.32. The input sequences $\{A[k]\}$ and $\{B[k]\}$ are first generated, each consisting of N i.i.d. real zero-mean Gaussian random variables with variance $N\Omega_p/2$. These samples are then applied to a filter with frequency response $H[k]$, followed by an IDFT to generate the time-domain samples of the complex faded envelope as

$$g[n] = \mathrm{IDFT}\{A[k]H[k] - \mathrm{j}B[k]H[k]\}_{n=0}^{N-1}$$
$$= \frac{1}{N}\sum_{k=0}^{N-1}(A[k]H[k] - \mathrm{j}B[k]H[k])\,\mathrm{e}^{\mathrm{j}2\pi kn/N}, \ n = 0, \ldots, N-1. \tag{2.204}$$
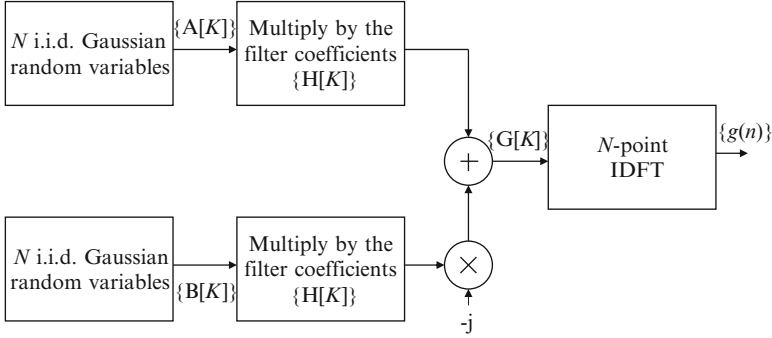
Fig. 2.32 IDFT-based fading simulator

Due to linearity of the IDFT operation, the discrete-time autocorrelation function of the output sample sequence $\{g[n]\} = \{g_I[n]\} + j\{g_Q[n]\}$, is [298]

$$\phi_{gg}[n] = \phi_{g_I g_I}[n] + j\phi_{g_I g_Q}[n]$$

$$= \frac{\Omega_p}{2} \left(a_I[n] + ja_Q[n]\right), \tag{2.205}$$

where $\{a[n]\} = \{a_I[n]\} + j\{a_Q[n]\}$ is given by the IDFT of the sequence $\{(H[k])^2\}$, that is,

$$a[n] = \frac{1}{N} \sum_{k=0}^{N-1} (H[k])^2 e^{j2\pi kn/N}, \; n = 0, \dots, N-1. \tag{2.206}$$

The only problem remaining is to design the filter, $H[k]$. To do so, we follow the argument by Young & Beaulieu [298].

A sequence $\{A_{CS}[k]\}$ that satisfies the property $A_{CS}[k] = A_{CS}^*[N-k]$ is called a conjugate-symmetric sequence, while a sequence $\{A_{CAS}[k]\}$ that satisfies the property $A_{CAS}[k] = -A_{CAS}^*[N-k]$ is called a conjugate-antisymmetric sequence. The IDFT of a conjugate-symmetric sequence is real valued, while the IDFT of a conjugate-antisymmetric sequence is imaginary valued. If the sequence $\{a[n]\}$ has discrete Fourier transform (DFT) $\{A[k]\}$ we have

$$a[n] = a_I[n] + ja_Q[n] = \text{IDFT}\{A[k]\}$$

$$= \text{IDFT}\{A_{CS}[k]\} + \text{IDFT}\{A_{CAS}[k]\}. \tag{2.207}$$

We also note that

$$A_{CS}[k] = \frac{1}{2}A[k] + \frac{1}{2}A^*[N-k] \tag{2.208}$$

and

$$A_{CAS}[k] = \frac{1}{2}A[k] - \frac{1}{2}A^*[N-k] \tag{2.209}$$

for any sequence $\{A[k]\}$, where $A[k] = A_{CS}[k] + A_{CAS}[k]$. Thus, the sequence $\{A[k]\}$ can always be decomposed into the sum of conjugate-symmetric and conjugate-antisymmetric components. To ensure that the quadrature components of the faded envelope, $\{g_I[n]\}$ and $\{g_Q[n]\}$, are uncorrelated, which is the case for 2D isotropic scattering and an isotropic antenna, we require that $A_{CAS}[k] = 0$ for all k. Using (2.208), the filter should have the following structure:

$$
H[k] = \begin{cases}
\sqrt{H_s[0]}, & k = 0 \\
\sqrt{\frac{H_s[k]}{2}}, & k = 1, 2, \ldots, \left(\frac{N}{2} - 1\right) \\
\sqrt{H_s[k]}, & k = \frac{N}{2} \\
\sqrt{\frac{H_s[N-k]}{2}}, & k = \left(\frac{N}{2} + 1\right), \ldots, (N-1)
\end{cases}, \tag{2.210}
$$

where the filter $H_s[k]$ can be obtained from the sampled Doppler spectrum.

To obtain the required filter $H[k]$, we assume 2D isotropic scattering with an isotropic antenna. The required normalized autocorrelation function and normalized Doppler spectrum are, respectively,

$$
\phi_{gg}(\tau) = J_0(2\pi f_m \tau) \tag{2.211}
$$

and

$$
S_{gg}(f) = \begin{cases}
\frac{1}{\pi f_m} \frac{1}{\sqrt{1 - (f/f_m)^2}} & |f| \leq f_m \\
0 & \text{otherwise}
\end{cases}. \tag{2.212}
$$

Ideally, we wish the generated sequence $g[n]$ to have the normalized autocorrelation function

$$
\phi_{gg}[n] = J_0(2\pi \hat{f}_m |n|), \tag{2.213}
$$

where $\hat{f}_m = f_m T_s$ is the maximum normalized Doppler frequency and T_s is the sampling period. However, an exact realization of this autocorrelation function is not possible, because the time-domain sequence is truncated to N samples. Looked at another way, while the theoretical spectrum is bandlimited, the truncation to N samples in the time-domain means that the realized spectrum is not bandlimited.

To obtain the required filter, we sample the continuous spectrum in (2.212) at frequencies $f_k = k/(NT_s), k = 0, \ldots, N - 1$. Special treatment is given to the frequency-domain coefficients at two points. The first is at zero frequency, where we set $H_s[0] = 0$ to ensure that the generated time-domain sequence always has zero-mean regardless of the particular values assumed by the length-N input sequences $\{A[k]\}$ and $\{B[k]\}$. The second is at the index k_m that is at, or just below, the maximum Doppler frequency, that is,

$$
k_m = \lfloor f_m N T_s \rfloor = \lfloor \hat{f}_m N \rfloor, \tag{2.214}
$$

where $\lfloor x \rfloor$ is the largest integer contained in x. The realized maximum Doppler frequency is $k_{\mathrm{m}}/(NT_{\mathrm{s}})$ Hz. The area under the Doppler spectrum curve in (2.212) from zero to frequency f is [118, 2.271.4]

$$C(f) = \frac{k_{\mathrm{m}}}{NT_{\mathrm{s}}}\arcsin(fNT_{\mathrm{s}}/k_{\mathrm{m}}), \ \ 0 \leq f \leq k_{\mathrm{m}}/(NT_{\mathrm{s}}). \tag{2.215}$$

The area under the Doppler spectrum between the frequencies represented by the samples $(k_{\mathrm{m}} - 1)$ and k_{m} is equal to $C(k_{\mathrm{m}}/(NT_{\mathrm{s}})) - C([k_{\mathrm{m}} - 1]/(NT_{\mathrm{s}}))$. Approximating this area by a rectangle of height $(H_s[k_{\mathrm{m}}])^2$ and width $1/(NT_{\mathrm{s}})$ gives

$$H_s[k_{\mathrm{m}}] = \sqrt{k_{\mathrm{m}}\left[\frac{\pi}{2} - \arctan\left(\frac{k_{\mathrm{m}} - 1}{\sqrt{2k_{\mathrm{m}} - 1}}\right)\right]}. \tag{2.216}$$

The complete filter $H[k]$ can now be specified as follows:

$$H[k] = \begin{cases} 0, & k = 0 \\[2ex] \sqrt{\dfrac{1}{2\pi f_{\mathrm{m}}\sqrt{1 - (k/(N\hat{f}_{\mathrm{m}}))^2}}}, & k = 1, 2, \ldots, k_{\mathrm{m}} - 1 \\[3ex] \sqrt{k_{\mathrm{m}}\left[\frac{\pi}{2} - \arctan\left(\frac{k_{\mathrm{m}} - 1}{\sqrt{2k_{\mathrm{m}} - 1}}\right)\right]}, & k = k_{\mathrm{m}} \\[3ex] 0, & k = k_{\mathrm{m}} + 1, \ldots, N - k_{\mathrm{m}} - 1 \\[3ex] \sqrt{k_{\mathrm{m}}\left[\frac{\pi}{2} - \arctan\left(\frac{k_{\mathrm{m}} - 1}{\sqrt{2k_{\mathrm{m}} - 1}}\right)\right]}, & k = N - k_{\mathrm{m}} \\[3ex] \sqrt{\dfrac{1}{2\pi f_{\mathrm{m}}\sqrt{1 - (N - k/(N\hat{f}_{\mathrm{m}}))^2}}}, & N - k_{\mathrm{m}} + 1, \ldots, N - 1 \end{cases} \tag{2.217}$$

The above IDFT approach will generate a Rayleigh faded envelope with an autocorrelation function that closely matches the reference model for large N. However, the main limitation of the IDFT approach arises from the block-oriented structure which may preclude continuous transmission in which there is a discontinuity in the time series (i.e., the faded envelope) from one block of N samples to the next.

Table 2.1 Coefficients for $K = 5$ biquad stage elliptical filter

Stage		Filter coefficients		
k	a_k	b_k	c_k	d_k
1	1.5806655278853	0.99720549234156	−0.64808639835819	0.88900798545419
2	0.19859624284546	0.99283177405702	−0.62521063559242	0.97280125737779
3	−0.60387555371625	0.9999939585621	−0.62031415619505	0.99996628706514
4	−0.56105447536557	0.9997677910713	−0.79222029531477	0.2514924845181
5	−0.39828788982331	0.99957862369507	−0.71405064745976	0.64701702807931
A	0.020939537466725			

2.5.1.2 IIR Filtering Method

Another approach is to implement the filters in the time-domain as finite impulse response (FIR) or infinite impulse response (IIR) filters. There are two main challenges with this approach. The first challenge arises from the fact that the sampled channel waveform is bandlimited to a discrete frequency $\hat{f}_m = f_m T_s$, where T_s is the sample period. Consider, for example, a cellular system operating at a carrier frequency of $f_c = 1,800$ MHz with a maximum MS speed of 300 km/h. In this case, the maximum Doppler frequency is $f_m = f_c(v/\lambda_c) = 500$ Hz, where c is the speed of light. If the signal is sampled at rate $R_s = 1/T_s = 1$ MHz, then the normalized Doppler frequency is $\hat{f}_m = f_m T_s = 0.0005$. If implemented as a FIR filter, such an extremely narrowband filter would required an impractically high filter order. Fortunately, this can be satisfied with an IIR filter designed at a lower sampling frequency followed by an interpolator to increase the sampling frequency. For example, we could design the shaping filter at a sampling frequency of 2 kHz, which is two times the Nyquist frequency. Later interpolate by a factor of $I = 500$ to obtain the desired sampling frequency of 1 MHz.

The second main challenge is that the square-root of the target Doppler spectrum for 2D isotropic scattering and an isotropic antenna in (2.212) is irrational and, therefore, none of the straightforward filter design methods can be applied. However, an approach developed by Steiglitz [245] allows the design of an IIR filter with an arbitrary magnitude response. Another possibility is to use the MATLAB function `iirlpnorm` [174].

Here we consider an IIR filter of order $2K$ that is synthesized as the cascade of K Direct-Form II second-order (two poles and two zeroes) sections (biquads) having the form

$$H(z) = A \prod_{k=1}^{K} \frac{1 + a_k z^{-1} + b_k z^{-2}}{1 + c_k z^{-1} + d_k z^{-2}}. \tag{2.218}$$

For example, for $f_m T_s = 0.4$, $K = 5$, and an ellipsoidal accuracy of 0.01, the filter design procedure described by Komninakis [142] results in the coefficients tabulated in Table 2.1. Figure 2.33 plots the magnitude response of the designed filter, which is shown to closely match that of the ideal filter.
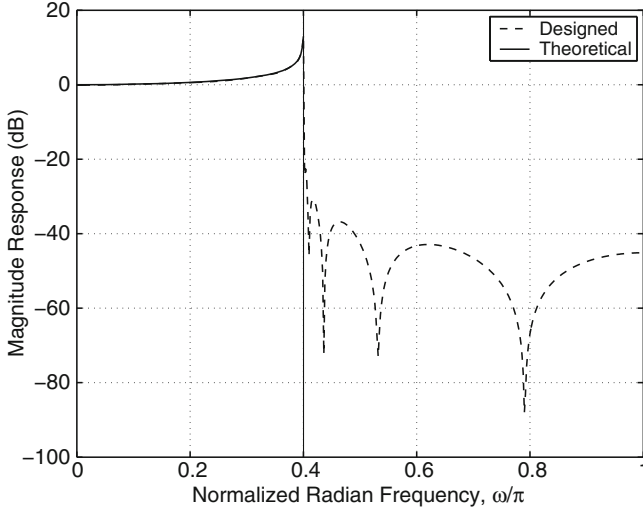
Fig. 2.33 Magnitude response of the designed shaping filter with $K = 5$ biquad sections

2.5.2 Sum of Sinusoids Methods

SoS channel models attempt to simulate the channel as a stationary complex Gaussian random process, formed by the sum of multiple sinusoids having appropriately selected frequencies, amplitudes, and phases. The objective is to generate a faded envelope having statistical properties that are as close as possible to a specified reference model, while at the same time minimizing the number of sinusoids that are required to achieve a given degree of modeling accuracy. SoS models are broadly categorized as either *deterministic* or *statistical*. Deterministic SoS models use fixed frequencies, amplitudes, and phases for the sinusoidal components. Therefore, the statistical properties of the faded envelope are deterministic for all simulation trials. Such models are useful for simulations that require continuous transmission over a long time interval, such as a real-time hardware channel simulator. In contrast, the statistical SoS models require multiple simulation trials, where one or more of the parameter sets (frequencies, amplitudes, or phases) are randomly selected for each simulation trial. As a result, the simulated channels have statistical properties that vary for each simulation trial, but they converge to the desired statistical properties when averaged over a sufficiently large number of simulation trials. Since a statistical model requires multiple simulation trials, it cannot be used in cases where continuous transmission is required. An ergodic statistical SoS model is one whose statistical properties converge to the desired properties in a single simulation trial. For this reason, an ergodic statistical model is essentially a deterministic model, but differs in the sense that one of the parameter sets, usually the phases, are randomly generated when the simulator is initialized.

2.5.2.1 Clarke's Model

Clarke derived a statistical SoS simulation model that begins with (2.9) and (2.6) and assumes equal strength multipath components ($C_n = \sqrt{1/N}$). The received complex envelope has the form

$$g(t) = \sqrt{\frac{1}{N}} \sum_{n=1}^{N} e^{j(2\pi f_\mathrm{m} t \cos(\theta_n) + \hat{\phi}_n)}, \tag{2.219}$$

where N is the number of sinusoids and the phases $\hat{\phi}_n$ are independent identically distributed (i.i.d.) uniform random variables on $[-\pi, \pi)$.

   If we assume a reference model having 2D isotropic scattering and an isotropic antenna, then the θ_n are also i.i.d. uniform random variables on $[-\pi, \pi)$ and are independent of the $\hat{\phi}_n$. Based on the above assumptions concerning the C_n, $\hat{\phi}_n$, and θ_n, the ensemble averaged correlation functions of Clarke's model in (2.219) for a *finite N* are[2]

$$\phi_{g_\mathrm{I} g_\mathrm{I}}(\tau) = \phi_{g_\mathrm{Q} g_\mathrm{Q}}(\tau) = \frac{1}{2} J_0(2\pi f_\mathrm{m} \tau), \tag{2.220}$$

$$\phi_{g_\mathrm{I} g_\mathrm{Q}}(\tau) = \phi_{g_\mathrm{Q} g_\mathrm{I}}(\tau) = 0, \tag{2.221}$$

$$\phi_{gg}(\tau) = \frac{1}{2} J_0(2\pi f_\mathrm{m} \tau), \tag{2.222}$$

$$\phi_{\alpha^2 \alpha^2}(\tau) = 1 + \frac{N-1}{N} J_0^2(2\pi f_\mathrm{m} \tau). \tag{2.223}$$

Note that for finite N, the autocorrelation and cross-correlation functions of $g_\mathrm{I}(t)$ and $g_\mathrm{Q}(t)$ match those of the reference model in (2.26) and (2.28), while the squared envelope autocorrelation function reaches the desired form $1 + J_0^2(2\pi f_\mathrm{m} \tau)$ in (2.78) asymptotically as $N \to \infty$.

2.5.2.2 Jakes' Model

Jakes [134] derived a deterministic SoS simulation model that is perhaps the most widely cited model in literature. Jakes' model begins by choosing the N sinusoidal components to be uniformly distributed in angle, that is,

$$\theta_n = \frac{2\pi n}{N}, \quad n = 1, 2, \ldots, N. \tag{2.224}$$

---

[2]Note that $\Omega_\mathrm{p} = \sum_{n=1}^{N} C_n^2 = 1$ in this case; other values of Ω_p can be obtained by straight forward scaling.

By choosing $N/2$ to be an odd integer, the sum in (2.219) can be rearranged into the form

$$g(t) = \sqrt{\frac{1}{N}} \left\{ \sum_{n=1}^{N/2-1} \left[e^{-j(2\pi f_{\mathrm{m}} t \cos(\theta_n) + \hat{\phi}_{-n})} + e^{j(2\pi f_{\mathrm{m}} t \cos(\theta_n) + \hat{\phi}_n)} \right] \right.$$

$$\left. + e^{-j(2\pi f_{\mathrm{m}} t + \hat{\phi}_{-N})} + e^{j(2\pi f_{\mathrm{m}} t + \hat{\phi}_N)} \right\}, \tag{2.225}$$

where we have relabeled the phase indices. Note that the Doppler shifts progress from $-2\pi f_{\mathrm{m}} \cos(2\pi/N)$ to $+2\pi f_{\mathrm{m}} \cos(2\pi/N)$ as n progresses from 1 to $N/2-1$ in the first sum, while they progress from $+2\pi f_{\mathrm{m}} \cos(2\pi/N)$ to $-2\pi f_{\mathrm{m}} \cos(2\pi/N)$ in the second sum. Therefore, the frequencies in these terms overlap. To reduce the number of sinusoidal components used in the model, Jakes uses non-overlapping frequencies to write $g(t)$ as

$$g(t) = \sqrt{\frac{1}{N}} \left\{ \sqrt{2} \sum_{n=1}^{M} \left[e^{-j(2\pi f_{\mathrm{m}} t \cos(\theta_n)) + \hat{\phi}_{-n}} + e^{j(2\pi f_{\mathrm{m}} t \cos(\theta_n) + \hat{\phi}_n)} \right] \right.$$

$$\left. + e^{-j(2\pi f_{\mathrm{m}} t + \hat{\phi}_{-N})} + e^{j(2\pi f_{\mathrm{m}} t + \hat{\phi}_N)} \right\}, \tag{2.226}$$

where

$$M = \frac{1}{2}\left(\frac{N}{2} - 1\right) \tag{2.227}$$

and the factor $\sqrt{2}$ is included so that the total power remains unchanged. Note that (2.225) and (2.226) are not equal. In (2.225) all phases are independent. However, (2.226) implies that $\hat{\phi}_n = -\hat{\phi}_{-N/2+n}$ and $\hat{\phi}_{-n} = -\hat{\phi}_{N/2-n}$ for $n = 1,\ldots,M$. If we further constrain the phases such that $\hat{\phi}_n = -\hat{\phi}_{-n}, n = 1,\ldots,M$ and $\hat{\phi}_N = -\hat{\phi}_{-N}$, then (2.226) can be rewritten in the form $g(t) = g_{\mathrm{I}}(t) + j g_{\mathrm{Q}}(t)$, where

$$g_{\mathrm{I}}(t) = \sqrt{\frac{2}{N}} \cdot 2 \sum_{n=1}^{M} \cos(\beta_n)\cos(2\pi f_n t) + \sqrt{2}\cos(\alpha)\cos(2\pi f_{\mathrm{m}} t), \quad (2.228)$$

$$g_{\mathrm{Q}}(t) = \sqrt{\frac{2}{N}} \cdot 2 \sum_{n=1}^{M} \sin(\beta_n)\cos(2\pi f_n t) + \sqrt{2}\sin(\alpha)\cos(2\pi f_{\mathrm{m}} t), \quad (2.229)$$

and where $\alpha = \hat{\phi}_N$ and $\beta_n = \hat{\phi}_n$.

Jakes chooses the phases α and β_n with the objective of making $\langle g_{\mathrm{I}}^2(t) \rangle = \langle g_{\mathrm{Q}}^2(t) \rangle$ and $\langle g_{\mathrm{I}}(t) g_{\mathrm{Q}}(t) \rangle = 0$, where $\langle \cdot \rangle$ denotes time averaging. From (2.228) and (2.229),

$$\langle g_{\mathrm{I}}^2(t) \rangle = \frac{2}{N}\left[2\sum_{n=1}^{M}\cos^2(\beta_n) + \cos^2(\alpha) \right]$$

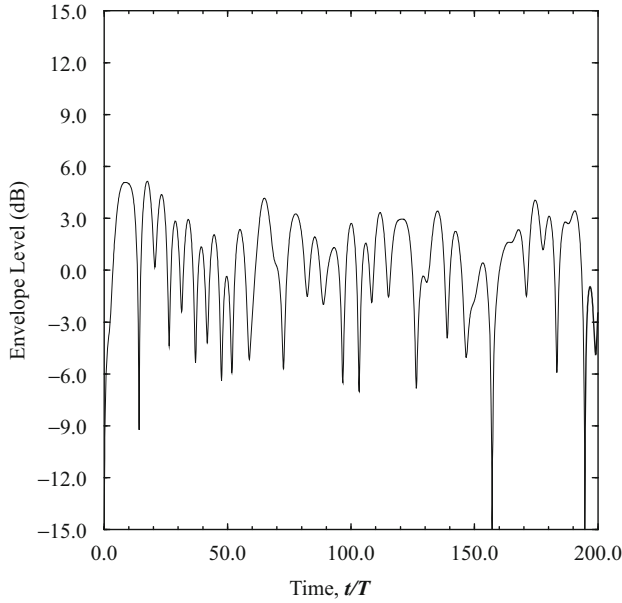$$= \frac{2}{N}\left[M + \cos^2(\alpha) + \sum_{n=1}^{M}\cos(2\beta_n) \right], \tag{2.230}$$

Fig. 2.34 Faded envelope generated using Jakes' method with $M = 8$ oscillators; $f_\mathrm{m}T = 0.1$

$$\langle g_Q^2(t)\rangle = \frac{2}{N}\left[2\sum_{n=1}^{M}\sin^2(\beta_n) + \sin^2(\alpha)\right]$$

$$= \frac{2}{N}\left[M + \sin^2(\alpha) - \sum_{n=1}^{M}\cos(2\beta_n)\right] \tag{2.231}$$

and

$$\langle g_I(t)g_Q(t)\rangle = \frac{2}{N}\left[2\sum_{n=1}^{M}\sin(\beta_n)\cos(\beta_n) + \sin(\alpha)\cos(\alpha)\right]. \tag{2.232}$$

Choosing $\alpha = 0$ and $\beta_n = \pi n/M$ gives $\langle g_Q^2(t)\rangle = M/(2M+1)$, $\langle g_I^2(t)\rangle = (M+1)/(2M+1)$ and $\langle g_I(t)g_Q(t)\rangle = 0$. Note that there is a small imbalance in the values of $\langle g_Q^2(t)\rangle$ and $\langle g_I^2(t)\rangle$. Finally, we note that $\langle g_I^2(t)\rangle + \langle g_Q^2(t)\rangle = \Omega_\mathrm{p} = 1$. The envelope power $\langle g_I^2(t)\rangle + \langle g_Q^2(t)\rangle$ can be easily scaled to any other desired value. A typical faded envelope obtained using Jakes' method with $N = 34$ or ($M = 8$) is shown in Fig. 2.34.

The accuracy of Jakes' simulator can be evaluated by comparing the autocorrelation functions of the complex envelope with those of the 2D isotropic scattering reference model. Suppose we modify Clarke's method by imposing the additional restrictions of even N and $\theta_n = 2\pi n/N$. The resulting model is still a statistical
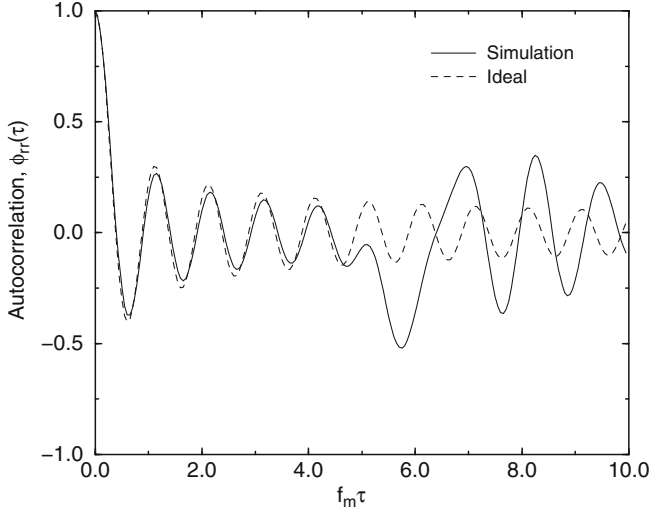
Fig. 2.35 Autocorrelation of in-phase and quadrature components obtained using Clarke's method with $M = 8$ oscillators

model, because the phases $\hat{\phi}_n$ are still i.i.d. uniform random variable on $[-\pi, \pi)$. A faded envelope is obtained having the autocorrelation function

$$\phi_{gg}(\tau) = \frac{1}{2N} \sum_{n=1}^{N} \cos\left(2\pi f_{\mathrm{m}}\tau \cos\left(\frac{2\pi n}{N}\right)\right), \tag{2.233}$$

where ensemble averaging is performed over the random phases. Note that this autocorrelation tends to a Bessel function as $N \to \infty$. The normalized autocorrelation functions in (2.222) and (2.233) with $N = 8$ are plotted against the normalized time delay $f_{\mathrm{m}}\tau$ in Fig. 2.35. Observe that Clark's model with $\theta_n = 2\pi n/N$ yields an autocorrelation function that deviates from the desired values at large lags. This can be improved upon by increasing the number of oscillators that are used in the simulator. For example, Fig. 2.36 shows the autocorrelation function when the number of oscillators is doubled from $N = 8$ to $N = 16$.

The autocorrelation function in (2.233) was originally reported in Jakes' [134], and it may be confused with the autocorrelation function of the faded envelope generated by (2.228) and (2.229). However, Jakes' method in (2.228) and (2.229) is a deterministic simulation model with no random parameters and, therefore, only the time averaged autocorrelation function exists. This time averaged autocorrelation function has been derived by Pop and Beaulieu as [209]

$$\hat{\phi}_{gg}(t, t+\tau) = \frac{1}{2N}\left(\cos(2\pi f_{\mathrm{m}}\tau) + \cos(2\pi f_{\mathrm{m}}(2t+\tau))\right)$$

$$+ \frac{1}{N}\sum_{n=1}^{M}\left(\cos(2\pi f_n \tau) + \cos(2\pi f_n(2t+\tau))\right). \tag{2.234}$$
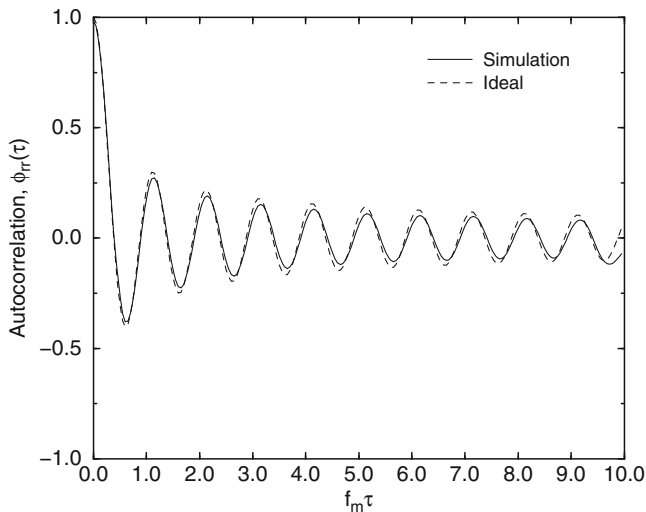
Fig. 2.36 Autocorrelation of in-phase and quadrature components obtained using Clarke's method with 16 oscillators

From (2.234), it is apparent that the time averaged autocorrelation function with Jakes' method, $\hat{\phi}_{gg}(t, t + \tau)$, depends on the time variable t. Hence, Jakes' method yields a faded envelope that is not stationary or even WSS. The root cause of this nonstationary behavior is the correlation that is introduced into the phases of the Jakes model, that is, restrictions $\hat{\phi}_n = -\hat{\phi}_{-N/2+n}$, $\hat{\phi}_{-n} = -\hat{\phi}_{N/2-n}$, $\hat{\phi}_n = -\hat{\phi}_{-n}, n = 1, \ldots, M$, and $\hat{\phi}_N = -\hat{\phi}_{-N}$.

2.5.3   *Multiple Uncorrelated Faded Envelopes*

In many cases, it is necessary to generate multiple uncorrelated faded envelopes. Jakes [134] suggested a method to modify the method in Sect. 2.5.2.2 to generate up to M fading envelopes. However, the method yields faded envelopes that exhibit very large cross-correlations at some nonzero lags and, therefore, the method is not recommended. We now present deterministic and statistical simulation models that will generate multiple faded envelopes having low cross-correlations. These simulation models outperform other simulation models reported in the literature, and a detailed comparison is available in [300].

2.5.3.1 Deterministic Model

With our deterministic model, the kth faded envelope, $g_k(t) = g_{I,k}(t) + \mathrm{j} g_{Q,k}(t)$, is generated as [300]

$$g_{I,k}(t) = \sqrt{\frac{2}{N}} \sum_{n=0}^{M} a_n \cos(2\pi f_{\mathrm{m}} t \cos(\theta_{n,k}) + \phi_{n,k}), \qquad (2.235)$$

$$g_{Q,k}(t) = \sqrt{\frac{2}{N}} \sum_{n=0}^{M} b_n \sin(2\pi f_{\mathrm{m}} t \cos(\theta_{n,k}) + \phi_{n,k}), \qquad (2.236)$$

where

$$M = \frac{1}{2}\left(\frac{N}{2} - 1\right), \qquad (2.237)$$

and

$$a_n = \begin{cases} 2\cos(\beta_n), & n = 1,\dots,M \\ \sqrt{2}\cos(\beta_n), & n = 0 \end{cases}, \qquad (2.238)$$

$$b_n = \begin{cases} 2\sin(\beta_n), & n = 1,\dots,M \\ \sqrt{2}\sin(\beta_n), & n = 0 \end{cases}, \qquad (2.239)$$

$$\beta_n = \frac{\pi n}{M}, \quad n = 0,\dots,M, \qquad (2.240)$$

$$\theta_{n,k} = \frac{2\pi n}{N} + \frac{2\pi k}{MN} + \frac{0.2\pi}{MN}, \quad n = 0,\dots,M, \ k = 0,\dots,M-1. \qquad (2.241)$$

This method will generate M faded envelopes.

The angle $\theta_{n,k}$ is chosen so that the arrival angles associated with the kth faded envelope are obtained by rotating the arrival angles of the $(k-1)$th faded envelope by $2\pi/MN$. This ensures an asymmetrical arrangement of arrival angles, which minimizes the correlation between the multiple faded envelopes. The initial arrival angle, $\theta_{0,0}$, can be optimized to minimize the correlation between the quadrature components of each faded envelope. This results in the choice $\theta_{0,0} = 0.2\pi/MN$, a value optimized by experimentation. Finally, the phases $\phi_{n,k}$ are chosen as arbitrary realizations of uniform random variables on the interval $[0, 2\pi)$.

For our deterministic model, the autocorrelation and cross-correlation functions of the quadrature components, the autocorrelation and cross-correlation functions of the multiple faded envelopes, and the squared envelope autocorrelation are, respectively, [300]

$$\lim_{N\to\infty} \phi_{g_{I,k}g_{I,k}}(\tau) = \lim_{N\to\infty} \frac{2}{N} \sum_{n=0}^{M} \frac{a_n^2}{2} \cos(2\pi f_{\mathrm{m}} \tau \cos(\theta_{n,k}))$$

$$= \frac{1}{2} J_0(2\pi f_{\mathrm{m}}\tau) + \frac{1}{2} J_4(2\pi f_{\mathrm{m}}\tau), \qquad (2.242)$$

$$\lim_{N\to\infty} \phi_{g_{Q,k}g_{Q,k}}(\tau) = \lim_{N\to\infty} \frac{2}{N} \sum_{n=0}^{M} \frac{b_n^2}{2} \cos(2\pi f_{\mathrm{m}}\tau \sin(\theta_{n,k}))$$

$$= \frac{1}{2}J_0(2\pi f_{\mathrm{m}}\tau) - \frac{1}{2}J_4(2\pi f_{\mathrm{m}}\tau), \tag{2.243}$$

$$\phi_{g_{I,k}g_{Q,k}}(\tau) = \phi_{g_{Q,k}g_{I,k}}(\tau) = \phi_{g_k g_{l\neq k}}(\tau) = 0, \tag{2.244}$$

$$\lim_{N\to\infty} \phi_{g_k g_k}(\tau) = \lim_{N\to\infty} \frac{2}{N} \sum_{n=0}^{M} \frac{a_n^2}{2} \cos(2\pi f_{\mathrm{m}}\tau \cos(\theta_{n,k}))$$

$$+ \lim_{N\to\infty} \frac{2}{N} \sum_{n=0}^{M} \frac{b_n^2}{2} \cos(2\pi f_{\mathrm{m}}\tau \sin(\theta_{n,k}))$$

$$= \frac{1}{2}J_0(2\pi f_{\mathrm{m}}\tau), \tag{2.245}$$

$$\phi_{\alpha_k^2 \alpha_k^2}(\tau) = \frac{2}{N^2} \sum_{n=0}^{M} a_n^4 + \frac{2}{N^2} \sum_{n=0}^{M} b_n^4 + \frac{1}{2}\phi_{g_{I,k}g_{I,k}}^2(\tau)$$

$$+ \frac{1}{2}\phi_{g_{Q,k}g_{Q,k}}^2(\tau) + \phi_{g_{I,k}g_{Q,k}}^2(\tau)$$

$$= \frac{1}{4}J_0^2(\omega_m\tau), \tag{2.246}$$

where $J_0(\cdot)$ is the zero-order Bessel function of the first kind and $J_4(\cdot)$ is the fourth-order Bessel function of the first kind.

Figures 2.37 and 2.38 confirm that, for $M = 8$, the autocorrelation and cross-correlation of the quadrature components and the autocorrelation and cross-correlation of the multiple faded envelopes approach values given by (2.242) – (2.245), respectively. The model satisfies (2.221) and (2.222) of the reference model. However, the autocorrelations of the quadrature components and the autocorrelation of the squared envelope are close to, but do not perfectly match, (2.220) and (2.223). Nevertheless, our deterministic model is shown in [300] to outperform other well-known deterministic simulation models, including the Jakes' model [134] and MEDS model [206].

2.5.3.2   Statistical Model

Our deterministic model can be modified to better match the statistical properties of the reference model by introducing randomness into the model. To do so, the kth faded envelope, $g_k(t) = g_{I,k}(t) + jg_{Q,k}(t)$, is generated as

$$g_{I,k}(t) = \sqrt{\frac{2}{N}} \sum_{n=0}^{M} \cos(\beta_{n,k}) \cos(2\pi f_{\mathrm{m}}t \cos(\theta_{n,k}) + \phi_{n,k}), \tag{2.247}$$
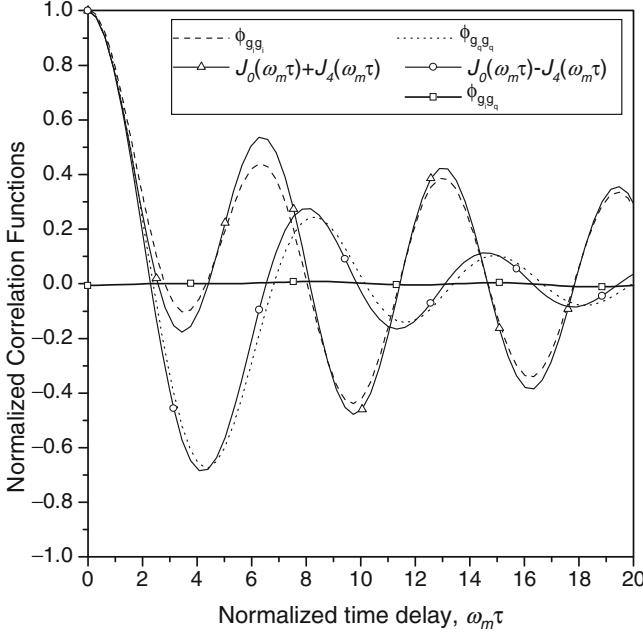
Fig. 2.37 Theoretical and simulated autocorrelation functions and the cross-correlation function of the in-phase and quadrature components of the deterministic model

$$g_{Q,k}(t) = \sqrt{\frac{2}{N}} \sum_{n=0}^{M} \sin(\beta_{n,k}) \sin(2\pi f_{\mathrm{m}} t \cos(\theta_{n,k}) + \phi_{n,k}), \qquad (2.248)$$

where $M = N/4$,

$$\theta_{n,k} = \frac{2\pi n}{N} + \frac{\pi k}{2MN} + \frac{\alpha_k - \pi}{N}, \quad n = 1,\dots,M, \; k = 0,\dots,M-1, \qquad (2.249)$$

and $\phi_{n,k}$, $\beta_{n,k}$, and α_k are independent uniform random variables on the interval $[-\pi, \pi)$. The parameter $\theta_{n,k}$ is chosen in the following manner: the arrival angles of the kth faded envelope are obtained by rotating the arrival angles of the $(k-1)$th faded envelope by $\pi/2MN$. Randomness in the Doppler frequencies is introduced by random variable α_k.

Figures 2.39 and 2.40 show that, for $M = P = 8$ and $N_{stat} = 30$ simulation trials, the autocorrelation and cross-correlations of the quadrature components, and the autocorrelation and cross-correlations of the complex faded envelopes approach those of the reference model in (2.220) and (2.222). Although not shown, the squared-envelope autocorrelation also approaches that of the reference model in (2.223). Finally, our statistical model is shown in [300] to outperform other well-known statistical simulation models, including the Zheng & Xiao model [307].
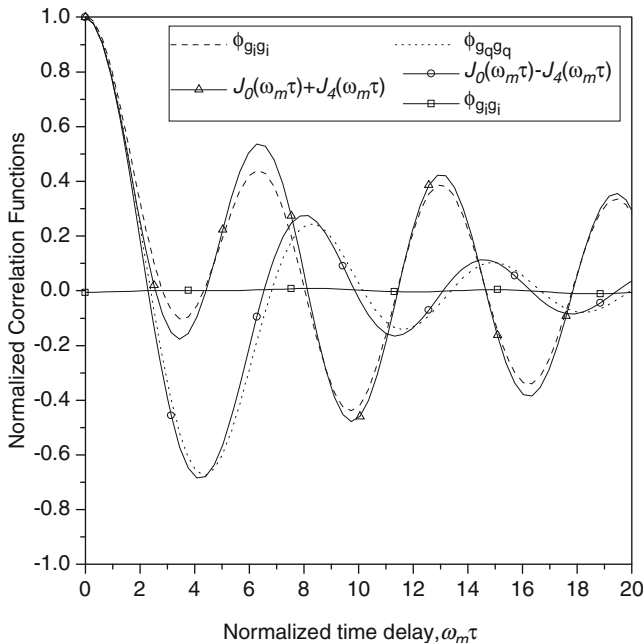
Fig. 2.38 Theoretical and simulated autocorrelation functions and the cross-correlation function of the first and the second complex envelope of the deterministic model

2.5.4   Wide-Band Simulation Models

Wide-band channels can be modeled by a tapped delay line with irregularly spaced tap delays. Each channel tap is the superposition of a large number of scattered plane waves that arrive with approximately the same delay and, therefore, the channel taps will undergo fading. The wide-band channel has the time-variant impulse response

$$g(t, \tau) = \sum_{i=1}^{\ell} g_i(t) \delta(\tau - \tau_i), \tag{2.250}$$

where ℓ is the number of channel taps, and the $\{g_i(t)\}$ and $\{\tau_i\}$ are the complex gains and path delays associated with the channel taps. The corresponding time-variant transfer function is

$$T(f,t) = \sum_{i=1}^{\ell} g_i(t) e^{j2\pi f \tau_i}. \tag{2.251}$$

Usually, the tap delays are multiples of some very small delay τ, such that $\tau_i = K_i \tau$, $i = 1, \ldots, \ell$, which yields the sparse tapped delay line channel model
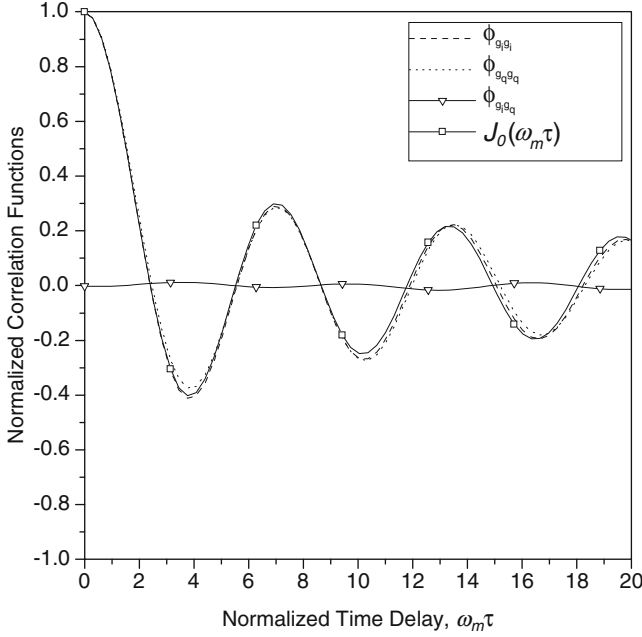
Fig. 2.39 Theoretical and simulated autocorrelation functions and the cross-correlation function of the quadrature components of the statistical model

shown in Fig. 2.41. We call this the "τ-spaced" model. Many of the tap coefficients in the tapped delay line are zero, reflecting the fact that no energy is received at these delays. Also, the K_i should be chosen to be relatively prime so as to prevent any periodicity in the channel. Assuming a WSSUS channel, the autocorrelation function of the time-variant channel impulse response in (2.250) is

$$\phi_g(t, s; \tau, \eta) = \frac{1}{2}\mathrm{E}[g(t, \tau)g^*(s, \eta)] \tag{2.252}$$

$$= \sum_{i=1}^{\ell} \phi_{g_i g_i}(\Delta t)\delta(\tau - \tau_i)\delta(\eta - \tau). \tag{2.253}$$

It follows that the channel correlation function is

$$\psi_g(\Delta t; \tau) = \sum_{i=1}^{\ell} \phi_{g_i g_i}(\Delta t)\delta(\tau - \tau_i) \tag{2.254}$$

and the power-delay profile is

$$\psi_g(\tau) = \psi_g(0; \tau) = \sum_{i=1}^{\ell} \Omega_i\delta(\tau - \tau_i), \tag{2.255}$$
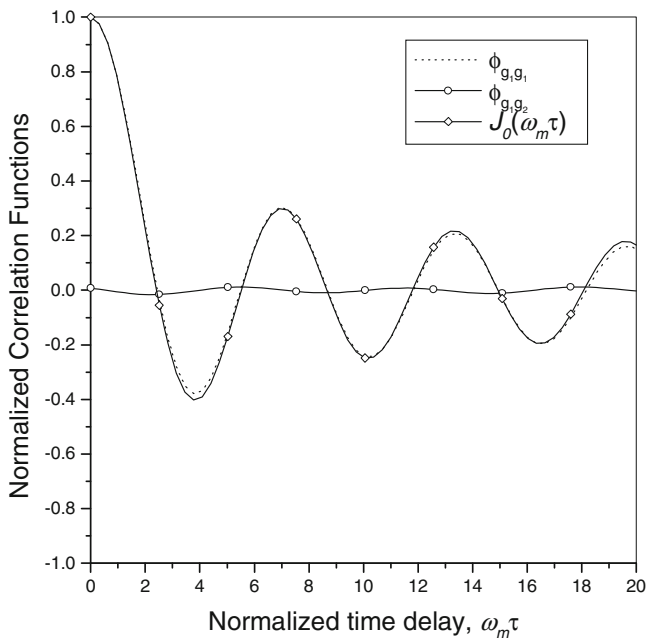
Fig. 2.40 Theoretical and simulated autocorrelation functions and the cross-correlation function of the first and the second complex envelopes of the statistical model
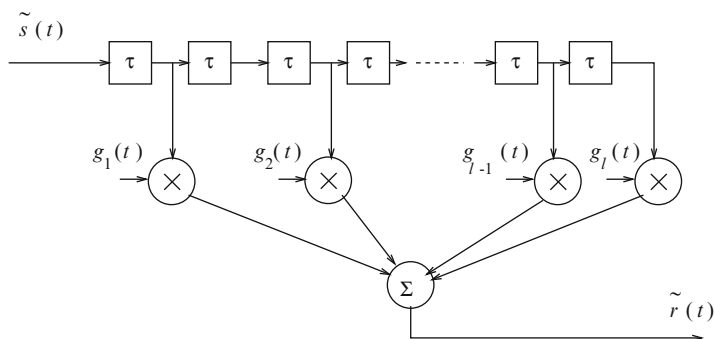
Fig. 2.41 Sparse tapped delay line model for wide-band multipath-fading channels

where $\Omega_i = \phi_{g_i g_i}(0)$ is the envelope power of the ith channel tap, and the total envelope power is

$$\Omega_p = \sum_{k=1}^{\ell} \Omega_k. \tag{2.256}$$

Hence, the channel can be described by the power profile

$$\Omega = (\Omega_0, \, \Omega_1, \ldots, \Omega_\ell) \tag{2.257}$$

and the delay profile

$$\tau = (\tau_1, \tau_2, \dots, \tau_\ell). \tag{2.258}$$

Taking the Fourier transform of (2.254) with respect to the τ variable yields the spaced-time spaced-frequency correlation function

$$\phi_T(\Delta f; \Delta t) = \sum_{i=1}^{\ell} \phi_{g_i g_i}(\Delta t) e^{-j2\pi \Delta f \tau_i}. \tag{2.259}$$

Sometimes the channel taps are assumed to have the same time correlation function, such that

$$\phi_{g_i g_i}(\Delta t) = \Omega_i \phi_t(\Delta t), \quad i = 1, \dots, \ell. \tag{2.260}$$

For example, if each tap is characterized by 2D isotropic scattering, then we have $\phi_t(\Delta t) = \frac{1}{2} J_0(2\pi f_m \Delta t)$. In this case, the spaced-time spaced-frequency correlation function has the separable form

$$\phi_T(\Delta f; \Delta t) = \phi_t(\Delta t)\phi_f(\Delta f), \tag{2.261}$$

where

$$\phi_f(\Delta f) = \sum_{i=1}^{\ell} \Omega_i e^{-j2\pi \Delta f \tau_i}. \tag{2.262}$$

2.5.4.1 COST 207 Models

The COST 207 models were developed for the GSM cellular system. Four different Doppler spectra $S_{gg}(f)$ are specified in the COST 207 models [64]. First define the function

$$G(A, f_1, f_2) = A \exp\left\{-\frac{(f - f_1)^2}{2 f_2^2}\right\} \tag{2.263}$$

which has the shape of a Gaussian probability density function with mean f_1 and variance f_2^2. COST 207 specifies the following Doppler spectra:

(a) CLASS is the classical Doppler spectrum and is used for excess path delays not exceeding 500 ns ($\tau_i \leq 500$ ns);

$$\text{(CLASS)} \quad S_{gg}(f) = \frac{A}{\sqrt{1 - (f/f_m)^2}}, \quad |f| \leq f_m \tag{2.264}$$

Multipath components arriving with short path delays are those that experience local scattering around the MS. In the COST 207 models, the local scattering is modeled as 2D isotropic scattering and the MS is assumed to have an isotropic antenna.

(b) GAUS1 is the sum of two Gaussian functions and is used for excess path delays
     ranging from 500 ns to $2\,\mu$s; (500 ns $\leq \tau_i \leq 2\mu$s)

$$\text{(GAUS1)} \qquad S_{gg}(f) = G(A, -0.8f_{\mathrm{m}}, 0.05f_{\mathrm{m}}) + G(A_1, 0.4f_{\mathrm{m}}, 0.1f_{\mathrm{m}}), \quad (2.265)$$

where A_1 is 10 dB below A. The GAUS1 Doppler spectra implies two clusters
of scattering objects. The larger cluster is located behind the MS such that the
mean AoA is $\theta = \cos^{-1}(-0.8) = \pm 143^{\mathrm{o}}$. A smaller cluster is located in front
of the MS such that the mean AoA is $\theta = \cos^{-1}(0.4) = \pm 66^{\mathrm{o}}$.

(c) GAUS2 is the sum of two Gaussian functions, used for excess path delays
     exceeding $2\,\mu$s; ($\tau_i > 500$ ns)

$$\text{(GAUS2)} \qquad S_{gg}(f) = G(B, 0.7f_{\mathrm{m}}, 0.1f_{\mathrm{m}}) + G(B_1, -0.4f_{\mathrm{m}}, 0.15f_{\mathrm{m}}), \quad (2.266)$$

where B_1 is 15 dB below B. Like GAUS1, GAUS2 implies two clusters of
scattering objects such that the mean angles of arrival are $\theta = \cos^{-1}(0.7) = \pm 45^{\mathrm{o}}$ and $\theta = \cos^{-1}(-0.4) = \pm 113^{\mathrm{o}}$.

(d) RICE is a combination of 2D isotropic scattering and an LoS component;

$$\text{(RICE)} \qquad S_{gg}(f) = \frac{0.41}{2\pi f_{\mathrm{m}}\sqrt{1 - (f/f_{\mathrm{m}})^2}} + 0.91\delta(f - 0.7f_{\mathrm{m}}), \qquad |f| \leq f_{\mathrm{m}}$$

$$(2.267)$$

The RICE scattering environment is depicted in Fig. 2.7, where $\theta_0 = \cos^{-1}(0.7) = 45^{\mathrm{o}}$.

Several power delay profiles have been defined in the COST 207 study for
different environments [64]. Typical urban (TU) (non-hilly) and bad urban (BU)
(hilly) discrete power-delay profiles are shown in Fig. 2.42 and Table 2.5 of
Appendix 1. In these figures and tables, the fractional power sums to unity, that is,
the total envelope power Ω_{p} is normalized to unity. Also notice that the discrete tap
delays in Table 2.5 are chosen to avoid a regular spacing between taps so as to avoid
any periodicities in the time-variant transfer function. Sometimes it is desirable to
use a smaller number of taps to reduce the computational requirements of computer
simulations. Figure 2.43 and Table 2.6 of Appendix 1 show the 6-ray reduced typical
urban and reduced bad urban channel. Also provided in Appendix 1 are discrete tap
models for rural (non-hilly) areas (RA) in Table 2.7, typical hilly terrain (HT) in
Table 2.8, and reduced HT in Table 2.9.

2.5.4.2   COST 259 Models

The COST 207 models were developed for the GSM system having a channel
bandwidth of 200 kHz. However, the COST 207 models are not be appropriate
for WCDMA systems with 5, 10, and 20 MHz channel bandwidths. Similar to
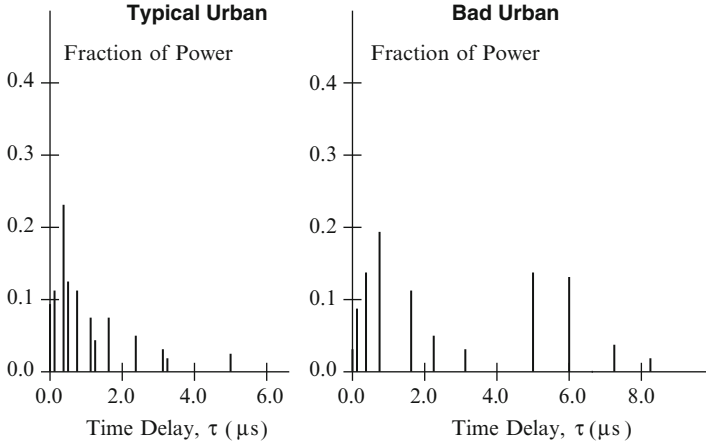
Fig. 2.42 COST 207 typical urban (TU) and bad urban (BU) power-delay profiles
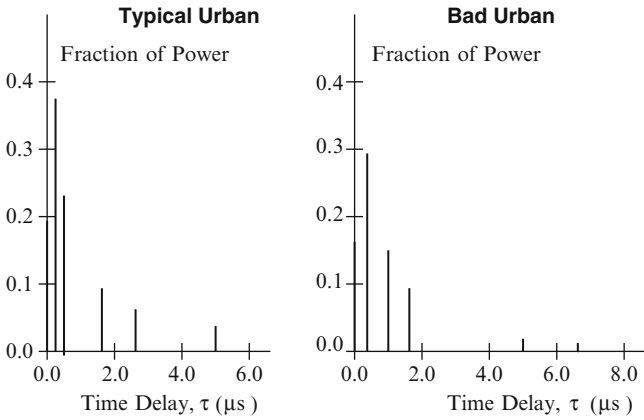
Fig. 2.43 COST 207 reduced typical urban (TU) and bad urban (BU) power-delay profiles

the COST 207 models, typical realizations have been developed by 3GPP for the COST 259 models [91]. These are tabulated in Tables 2.10 –2.12 of Appendix 2 for typical urban (TU), rural area (RA), and hilly terrain (HT). Notice that the tap positions in the 3GPP realizations of the COST 259 models are multiples of $0.001\,\mu$s as compared to the $0.1\,\mu$s used in the COST 207 models. Moreover, a large number of paths (20) are included to ensure that the frequency-domain correlation properties are realistic, which is important for wide-band systems.
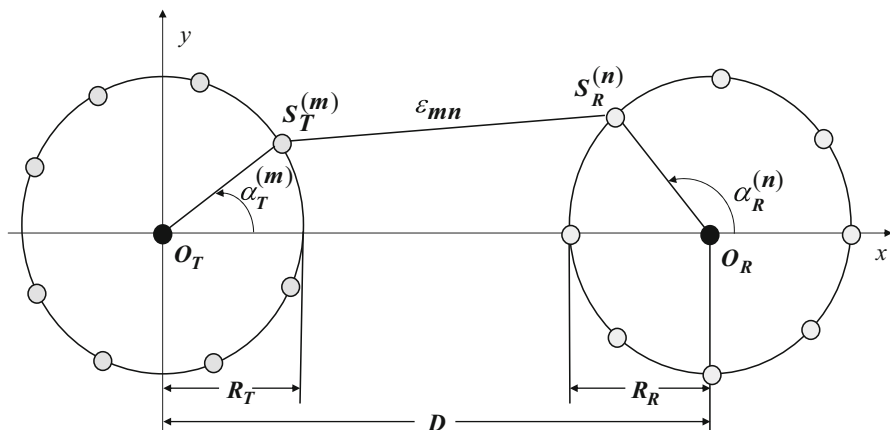
Fig. 2.44 Double ring model for M-to-M radio propagation with isotropic scattering at the transmitter and receiver

2.5.5   Mobile-to-Mobile Simulation Models

An important distinction between F-to-M cellular land mobile radio channels and M-to-M channels arises due to the scattering and mobility at both ends of the link. In contrast to cellular F-to-M channels, it is natural for both the transmitter and the receiver to have low elevation antennas in M-to-M applications. This results in local scattering around both the transmitter and receiver antennas which led to the 2D isotropic scattering assumption in the Akki and Haber reference model [10]. To develop M-to-M channel simulation models, we apply a double-ring concept that defines two rings of isotropic scatterers, one placed around the transmitter and another placed around the receiver as shown in Fig. 2.44. Assuming omnidirectional antennas at both ends, the waves from the transmitter antenna first arrive at the scatterers located on the transmitter ring. Considering these fixed scatterers as "virtual base-stations (VBS)," the communication link from each VBS to the receiver is treated like a F-to-M link. The signals from each VBS arrive at the receiver antenna uniformly from all directions in the horizontal plane due to isotropic scatterers located on the receiver end ring. It should be noted here that the double-ring model has been often used in various forms, for example in [41] and references therein for the study and simulation of the spatial correlations and capacity in MIMO systems, where multiple antennas are used at both the transmitter and receiver. Here we apply the double-ring model to M-to-M channel modeling. The use of a double-ring model has a strong rationale. First and foremost, it is a mathematically convenient reference model. Second, considering the lack of a detailed and standardized M-to-M channel models, the model provides a generic scenario with isotropic scattering at both ends of the communication link. Finally,

empirical Doppler spectrum measurements for vehicle-to-vehicle communication links [7, 175] more or less match those predicted by the double-ring model.

Using the double-ring model in Fig. 2.44, the complex faded envelope can be written as

$$g(t) = \sqrt{\frac{2}{NM}} \sum_{m=1}^{N} \sum_{n=1}^{M} e^{-j2\pi\varepsilon_{mn}/\lambda_c} e^{j2\pi t \left\{ f_{\mathrm{m}}^{\mathrm{T}} \cos\left(\alpha_T^{(m)}\right) + f_{\mathrm{m}}^{\mathrm{R}} \cos\left(\alpha_{\mathrm{R}}^{(n)}\right) \right\} + j\phi_{n,m}}, \quad (2.268)$$

where the index "m" refers to the paths traveling from the transmitter to the N scatterers located on the transmitter end ring, and the index "n" refers to the paths traveling from the M scatterers on the receiver end ring to the receiver. The angle $\alpha_T^{(m)}$ is the random angle of departure and $\alpha_{\mathrm{R}}^{(n)}$ is the random AoA of the $\{m,n\}$th propagation path measured with respect to the x-axis, respectively. The phases $\phi_{n,m}$ are uniformly distributed on $[-\pi,\pi)$ and are independent for all pairs $\{n,m\}$. Note that the single summation in (2.142) is replaced with a double summation, because each plane wave on its way from the transmitter to the receiver is double bounced. The temporal correlation characteristics remain the same as those of the model in (2.142), because each path will undergo a Doppler shift due to the motion of both the transmitter and receiver. Finally, we note that the temporal correlation properties do not depend on the distance ε_{mn} in Fig. 2.44. Although not discussed here, the spatial correlation properties will depend on ε_{mn} and, through ε_{mn}, on the scattering radii R_{T} and R_{R}, and the distance D.

2.5.5.1 Deterministic Model

We now suggest an ergodic statistical (deterministic) simulation model. By choosing only the phases to be random variables, the statistical correlation properties of this model will converge to those of the reference model in a single simulation trial. The complex faded envelope, $g(t) = g_{\mathrm{I}}(t) + jg_{\mathrm{Q}}(t)$, is generated as

$$g_{\mathrm{I}}(t) = \sqrt{\frac{1}{N_I M_I}} \sum_{m=1}^{M_I} \sum_{n=1}^{N_I} \cos\left(2\pi f_{\mathrm{m}}^{\mathrm{T}} \cos(\alpha_{I,n}^{T})t + 2\pi f_{\mathrm{m}}^{\mathrm{R}} \cos(\alpha_{I,m}^{R})t + \phi_{I,n,m}\right),$$

$$(2.269)$$

$$g_{\mathrm{Q}}(t) = \sqrt{\frac{1}{N_Q M_Q}} \sum_{m=1}^{M_Q} \sum_{n=1}^{N_Q} \cos\left(2\pi f_{\mathrm{m}}^{\mathrm{T}} \cos(\alpha_{Q,n}^{T})t + 2\pi f_{\mathrm{m}}^{\mathrm{R}} \cos(\alpha_{Q,m}^{R})t + \phi_{Q,n,m}\right),$$

$$(2.270)$$

where $\phi_{I,n,m}$ and $\phi_{Q,n,m}$ are all independent random phases uniformly distributed on $[-\pi,\pi)$. The nth angle of departure is equal to $\alpha_{I/Q,n}^{T} = \pi(n-0.5)/(2N_{I/Q})$, for $n = 1,2,\ldots,N_{I/Q}$. The mth AoA is equal to $\alpha_{I/Q,m}^{R} = \pi(m-0.5)/(M_{I/Q})$, for $m = 1,2,\ldots,M_{I/Q}$.

There are two remarks about this model. First, the angles $\alpha^T_{I/Q,n}$ are essentially the same as those in the method of exact Doppler spreads (MEDS) model [205], while the angles $\alpha^R_{I/Q,m}$ are chosen to reproduce desired statistical properties for M-to-M channels. Second, to make the time average correlation functions deterministic and independent of the random phases $\phi_{I/Q,n,m}$, the frequencies $f^T_m \cos(\alpha^T_{I,n}) + f^R_m \cos(\alpha^R_{I,m})$ in $g_I(t)$ and $f^T_m \cos(\alpha^T_{Q,n}) + f^R_m \cos(\alpha^R_{Q,m})$ in $g_Q(t)$ must all be distinct and, moreover, they must also be distinct among themselves for all pairs (n,m) and (k,l). Although it is difficult to establish a general rule to meet this criterion, choosing $N_I = M_I$ and $N_Q = M_Q = N_I + 1$ yields distinct Doppler frequencies for practical ranges of N_I varying from 5 to 60 and for different Doppler frequency ratios, that is, different values of $a = f^R_m / f^T_m$. This rule is similar to the one used in the MEDS model [205]. Under these assumptions, it can be shown that the time average correlation functions are

$$\hat{\phi}_{g_I g_I}(\tau) = \frac{1}{2N_I^2} \sum_{n,m=1}^{N_I,N_I} \cos\left(2\pi f^T_m \tau \cos(\alpha^T_{I,n}) + 2\pi f^R_m \tau \cos(\alpha^R_{I,m})\right), \quad (2.271)$$

$$\hat{\phi}_{g_Q g_Q}(\tau) = \frac{1}{2(N_I+1)^2} \sum_{n,m=1}^{(N_I+1),(N_I+1)} \cos(2\pi f^T_m \tau \cos(\alpha^T_{Q,n}) + 2\pi f^R_m \tau \cos(\alpha^R_{Q,m})),$$
$$(2.272)$$

$$\hat{\phi}_{g_I g_Q}(\tau) = \hat{\phi}_{g_Q g_I}(\tau) = 0. \quad (2.273)$$

2.5.5.2   Statistical Model

Although not shown here, our deterministic model has the disadvantage that the time averaged correlation functions match those of the reference model only for a small range of normalized time delays ($0 \leq f^T_m T_s \leq 3$). To improve upon the statistical properties, we suggest an alternative statistical model, where orthogonal functions are chosen for the quadrature components of the complex faded envelope. By allowing all three parameter sets (amplitudes, phases, and Doppler frequencies) to be random variables for each simulation trial, the statistical properties of this model will vary for each simulation trial, but they will converge to those of the reference model when averaged over a sufficient number of simulation trials. This model is also able to generate multiple uncorrelated complex faded envelopes.

The following function is considered as the kth complex faded envelope:

$$g_k(t) = \sqrt{\frac{1}{NM}} \sum_{n=1}^{N} \sum_{m=1}^{M} e^{j(2\pi f^T_m \cos(\alpha^T_{k,n})t + 2\pi f^R_m \cos(\alpha^R_{k,m})t + \phi_{k,n,m})}, \quad (2.274)$$

where f^T_m, f^R_m, $\alpha^T_{k,n}$, $\alpha^R_{k,m}$, and $\phi_{k,n,m}$ are the maximum Doppler frequencies, the random angle of departure, the random AoA, and the random phase, respectively.

It is assumed that P independent complex faded envelopes are required ($k = 0$, $\ldots, P-1$) each consisting of NM sinusoidal components.

The number of sinusoidal components needed for simulation can be reduced by choosing $N_0 = N/4$ to be an integer, by taking into account shifts of the angles $\alpha_{k,n}^T$ and $\alpha_{k,m}^R$, and by splitting the sum in (2.274) into four terms, viz.,

$$
\begin{aligned}
g_k(t) = {} & \sqrt{\frac{1}{NM}} \sum_{m=1}^{M} e^{j2\pi f_{\mathrm{m}}^R t \cos(\alpha_{k,m}^R)} \left(\sum_{n=1}^{N_0} \left(e^{j(2\pi f_{\mathrm{m}}^T t \cos(\alpha_{k,n}^T) + \phi_{k,n,m})} \right. \right. \\
& \left. \left. + e^{j(2\pi f_{\mathrm{m}}^T t \cos(\alpha_{k,n}^T + \pi/2) + \phi_{k,n,m} + \pi/2)} \right) \right) \\
& + \sqrt{\frac{1}{NM}} \sum_{m=1}^{M} e^{j2\pi f_{\mathrm{m}}^R t \cos(\alpha_{k,m}^R)} \left(\sum_{n=1}^{N_0} \left(e^{j(2\pi f_{\mathrm{m}}^T t \cos(\alpha_{k,n}^T + \pi) + \phi_{k,n,m} + \pi)} \right. \right. \\
& \left. \left. + e^{j(2\pi f_{\mathrm{m}}^T t \cos(\alpha_{k,n}^T + 3\pi/2) + \phi_{k,n,m} + 3\pi/2)} \right) \right).
\end{aligned}
\tag{2.275}
$$

Equation (2.275) simplifies as follows:

$$
\begin{aligned}
g_k(t) = {} & \sqrt{\frac{1}{N_0 M}} \sum_{n=1}^{N_0} \sum_{m=1}^{M} \cos\left(2\pi f_{\mathrm{m}}^R t \cos(\alpha_{k,m}^R)\right) \cos\left(2\pi f_{\mathrm{m}}^T t \cos(\alpha_{k,n}^T) + \phi_{k,n,m}\right) \\
& + j\sqrt{\frac{1}{N_0 M}} \sum_{n=1}^{N_0} \sum_{m=1}^{M} \sin\left(2\pi f_{\mathrm{m}}^R t \cos(\alpha_{k,m}^R)\right) \sin\left(2\pi f_{\mathrm{m}}^T t \sin(\alpha_{k,n}^T) + \phi_{k,n,m}\right).
\end{aligned}
\tag{2.276}
$$

Based on $g_k(t)$ in (2.276), we define our statistical simulation model. The kth complex faded envelope, $g_k(t) = g_{I,k}(t) + jg_{Q,k}(t)$, is generated as

$$
g_{I,k}(t) = \frac{1}{\sqrt{N_0 M}} \sum_{n=1}^{N_0} \sum_{m=1}^{M} \cos\left(2\pi f_{\mathrm{m}}^R \cos(\alpha_{k,m}^R) t\right) \cos\left(2\pi f_{\mathrm{m}}^T \cos(\alpha_{k,n}^T) t + \phi_{k,n,m}\right),
\tag{2.277}
$$

$$
g_{Q,k}(t) = \frac{1}{\sqrt{N_0 M}} \sum_{n=1}^{N_0} \sum_{m=1}^{M} \sin\left(2\pi f_{\mathrm{m}}^R \cos(\alpha_{k,m}^R) t\right) \sin\left(2\pi f_{\mathrm{m}}^T \sin(\alpha_{k,n}^T) t + \phi_{k,n,m}\right).
\tag{2.278}
$$

It is assumed that P independent complex envelopes are desired ($k = 0, \ldots, P-1$), each having MN_0 sinusoidal terms in I and Q components. The angles of departure and the angles of arrival are chosen as follows:

$$
\alpha_{k,n}^T = \frac{2\pi n}{4N_0} + \frac{2\pi k}{4PN_0} + \frac{\theta - \pi}{4N_0},
\tag{2.279}
$$

$$\alpha_{k,m}^{R} = 0.5 \left(\frac{2\pi m}{M} + \frac{2\pi k}{PM} + \frac{\psi - \pi}{M} \right),$$ (2.280)

for $n = 1, \ldots, N_0$, $m = 1, \ldots, M$ $k = 0, \ldots, P - 1$. The angles of departure and the angles of arrival in the kth complex faded envelope are obtained by rotating the angles of departure and the angles of arrival in the $(k-1)$th complex envelope by $(2\pi)/(4PN_0)$ and $(2\pi)/(2PM)$, respectively. The parameters $\phi_{k,n,m}$, θ, and ψ are independent uniform random variables on the interval $[-\pi, \pi)$.

The ensemble averaged statistical correlation functions of our statistical model match those of the reference model [301]. For brevity, only the derivation of the autocorrelation function of the in-phase component is presented. Other properties can be derived in an analogous fashion. The autocorrelation function of the in-phase component of the kth complex faded envelope is

$$\phi_{g_{k,I}g_{k,I}}(\tau) = E[g_{k,I}(t)g_{k,I}(t+\tau)]$$ (2.281)

$$= \frac{4}{N_0 M} \sum_{n,m=1}^{N_0,M} \sum_{p,r=1}^{N_0,M} E\left[\cos(2\pi f_{\mathrm{m}}^{R}(t+\tau)\cos(\alpha_{k,m}^{R})) \right.$$

$$\times \cos(2\pi f_{\mathrm{m}}^{R}t\cos(\alpha_{k,p}^{R}))\cos(2\pi f_{\mathrm{m}}^{T}(t+\tau)\cos(\alpha_{k,n}^{T}) + \phi_{k,n,m})$$

$$\left. \times \cos(2\pi f_{\mathrm{m}}^{T}t\cos(\alpha_{k,r}^{T}) + \phi_{k,p,r}) \right]$$

$$= \frac{1}{N_0 M} \sum_{n=1}^{N_0} \sum_{m=1}^{M} E\left[\cos(2\pi f_{\mathrm{m}}^{R}\tau\cos(\alpha_{k,m}^{R}))\cos(2\pi f_{\mathrm{m}}^{T}\tau\cos(\alpha_{k,n}^{T})) \right]$$

$$= \frac{1}{M} \sum_{m=1}^{M} \frac{1}{2\pi} \int_{-\pi}^{\pi} \cos\left(2\pi f_{\mathrm{m}}^{R}\tau\cos\left(\frac{2\pi m}{2M} + \frac{2\pi k}{2PM} + \frac{\psi - \pi}{2M} \right) \right) \mathrm{d}\psi$$

$$\times \frac{1}{N_0} \sum_{n=1}^{N_0} \frac{1}{2\pi} \int_{-\pi}^{\pi} \cos\left(2\pi f_{\mathrm{m}}^{T}\tau\cos\left(\frac{2\pi n}{4N_0} + \frac{2\pi k}{4PN_0} + \frac{\theta - \pi}{4N_0} \right) \right) \mathrm{d}\theta.$$

(2.282)

As in [290], the derivation can be completed by replacing the variables of integration, θ and ψ, with $\gamma_{k,n} = (2\pi n)/(4N_0) + (2\pi k)/(4PN_0) + (\theta - \pi)/(4N_0)$ and $\delta_{k,m} = (2\pi m)/(2M) + (2\pi k)/(2PM) + (\psi - \pi)/(2M)$, respectively. Finally,

$$\lim_{N_0,M \to \infty} \phi_{g_{k,I}g_{k,I}}(\tau) = J_0(2\pi f_{\mathrm{m}}^{T}\tau)J_0(2\pi f_{\mathrm{m}}^{R}\tau).$$ (2.283)

Figure 2.45 shows that, for $N_0 = M = P = 8$ and 30 simulation trials, the autocorrelation and cross-correlation of the complex faded envelopes produced by the statistical model approach those of the reference model.
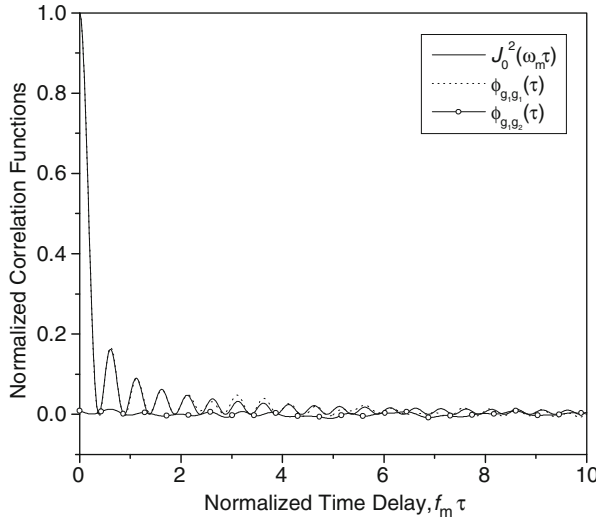
Fig. 2.45 Theoretical and simulated autocorrelation functions and cross-correlation functions of the first and the second faded envelopes produced by the statistical model with 30 simulation trials
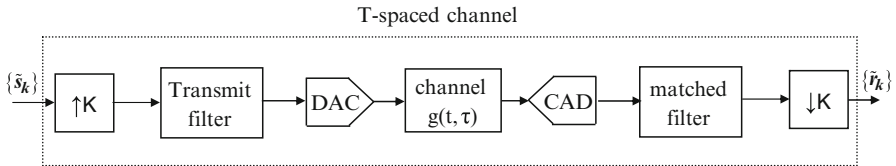
Fig. 2.46 Baseband model for a typical digital communication system

2.5.6 Symbol-Spaced Models

The baseband representation of a typical digital communication system consists of the concatenation of an up-sampler, a discrete-time transmit filter or pulse shaping filter, digital-to-analog converter (DAC), waveform channel, analog-to-digital converter (ADC), and discrete-time receiver filter or matched filter, and down-sampler as shown in Fig. 2.46. The channel $g(t, \tau)$ is assumed to have the structure in (2.250) or Fig. 2.41. Data symbols are input to the up-sampler, one every T seconds, where T is the baud period. Usually, the bandwidth of the transmitted signal W will exceed the Nyquist frequency $1/2T$; for example, when root-raised cosine pulse shaping is used. Therefore, up-sampling is required at the transmitter so that the DAC operates with sample period T/K, where K is the up-sampling

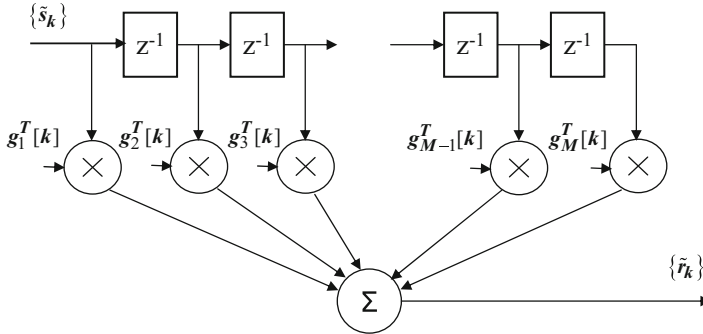**Fig. 2.47** Symbol-spaced tapped delay line model for wide-band multipath-fading channels

factor. At the receiver, the ADC also operates with a sampling period T/K. The up-sampling factor K must be chosen to at least to satisfy the sampling theorem at the transmit side, that is, $K/T \geq 2W$, but often K is made larger to facilitate timing synchronization in the receiver and to accommodate the Doppler spreading that is introduced by the channel. Once the correct sample timing phase is determined, the sample sequence at the output of the receiver filter can be down-sampled for further processing. For the purpose of illustration, we assume down-sampling by factor of K, so that symbol-spaced samples are taken at the output of the receiver filter.[3]

From the above discussion, it is apparent that the overall channel from the input to the transmitter filter to the output of the receiver filter can be modeled as a FIR filter as shown in Fig. 2.47, where the $\{g_n^T[k]\}$ are the tap gains. While it is true that the channel taps, $\{g_i(t)\}$ in the underlying waveform channel in Fig. 2.41 are uncorrelated for WSSUS channels, the same cannot be said of the taps $\{g_n^T[k]\}$ in the FIR filter of Fig. 2.47. The tap correlations in the symbol-spaced model often leads to analytical intractability when evaluating the theoretical performance of digital communication systems that operate on these channels. This difficulty is often overcome by assuming that the taps $\{g_n^T[k]\}$ are uncorrelated [73, 89, 111, 148, 160, 240, 253], when in fact they are not. However, when the same systems are evaluated by software simulation, such modeling simplifications are unnecessary and in fact undesirable. We now describe a method for generating the tap coefficients $\{g_n^T[k]\}$ with the proper cross-correlations in the case where linear modulation schemes are used. The procedure can be readily extended to generate the required tap coefficients when fractional sampling is used, that is, if $K > 1$.

Consider the arrangement shown in Fig 2.48, where we assume the equivalent analog representation of the transmit filter, $h_a(t)$, and receiver matched filter $h_a^*(-t)$. Pulses that are shaped by the transmit filter $h_a(t)$ are transmitted through the channel

---

[3]In practice, $T/2$-spaced samples at the output of the receiver filter are often used for further processing.
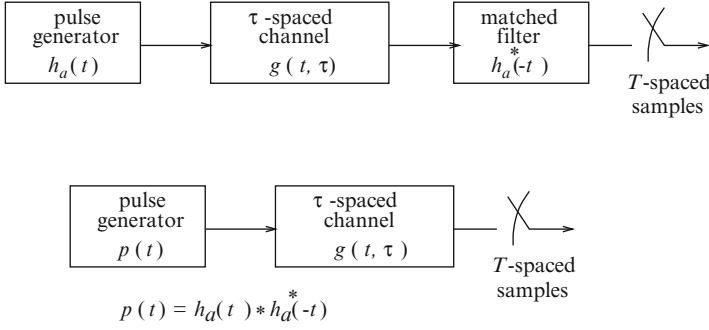
Fig. 2.48 Method for generating correlated tap coefficients in a T-spaced channel model

$g(t, \tau)$ and the receiver matched filter $h_a^*(-t)$. The output of the receiver matched filter is sampled at symbol-spaced intervals. Since the filters $h_a(t)$, $g(t, \tau)$, and $h_a^*(-t)$ are linear, we may exchange their order as shown in Fig 2.48, where the overall pulse is equal to $p(t) = h_a(t) * h_a^*(-t)$. The overall pulse $p(t)$ is usually chosen to be a Nyquist pulse. For example, $p(t)$ might be a raised cosine pulse so that $h_a(t)$ and $h_a^*(-t)$ are root-raised cosine pulses. To obtain the symbol-spaced channel tap coefficients, we pass the pulse $p(t)$ through the channel $g(t, \tau)$ and extract symbol-spaced samples at the output. Assuming that the channel has the form in (2.250), we now show that the symbol-spaced samples are a linear combination of the elements of the tap gain vector

$$\mathbf{g}(t) = (g_1(t), \ g_2(t), \ \ldots, \ g_\ell(t))^T. \tag{2.284}$$

Suppose that a vector of M, symbol-spaced, tap coefficients

$$\mathbf{g}^T(t) = (g_1^T(t), \ g_2^T(t), \ \ldots, \ g_M^T(t))^T \tag{2.285}$$

is to be generated. Then we can write $\mathbf{g}^T(t) = \mathbf{A}\mathbf{g}(t)$, where $\mathbf{g}(t)$ is defined in (2.284), and $\mathbf{A}$ is an $M \times \ell$ real matrix. As shown in Example 2.1 below, the entries of the matrix $\mathbf{A}$ are determined by the overall pulse $p(t)$, the delay profile τ in (2.258), and the timing phase of the sampler that extracts the symbol-spaced samples. The matrix $\mathbf{A}$ must be generated each time the delay profile and/or the sampler timing phase changes. For systems where timing information is derived from a training sequence or synchronization word that is inserted into every transmitted slot or burst, the sampler timing phase is usually adjusted on a burst-by-burst basis and, consequently, the matrix $\mathbf{A}$ must be computed on a burst-by-burst basis as well.

The autocovariance matrix of the symbol-spaced tap gain vector $\mathbf{g}^T(t)$ is

$$\Phi_{\mathbf{g}^T}(\tau) = \frac{1}{2}\mathrm{E}\left[\mathbf{g}^T(t)\mathbf{g}^{T\,H}(t+\tau)\right]$$

$$= \frac{1}{2}\mathrm{E}\left[\mathbf{A}\mathbf{g}(t)\mathbf{g}^H(t+\tau)\mathbf{A}^T\right]$$

$$= \mathbf{A}\frac{1}{2}\mathrm{E}\left[\mathbf{g}(t)\mathbf{g}^H(t+\tau)\right]\mathbf{A}^T$$

$$= \mathbf{A}\Phi_{\mathbf{g}}(\tau)\mathbf{A}^T.$$

For a WSSUS channel and 2D isotropic scattering on each of the channel taps $g_i(t)$, we have

$$\Phi_{\mathbf{g}}(\tau) = \frac{1}{2}\mathrm{diag}[\Omega_1,\Omega_2,\ldots,\Omega_\ell]J_0(2\pi f_{\mathrm{m}}\tau). \qquad (2.286)$$

Example 2.1

Suppose that the channel $g(t,\tau)$ consists of two taps having the spacing $\tau_s = |\tau_1(t) - \tau_0(t)|$. In this example, we wish to generate the two main taps in the symbol-spaced channel model, $g_0^T(t)$ and $g_1^T(t)$. Let

$$\mathbf{g}(t) = (g_0(t),g_1(t))^T,$$
$$\mathbf{g}^T(t) = (g_0^T(t),g_1^T(t))^T$$

and

$$\mathbf{g}^T(t) = \mathbf{A}\mathbf{g}(t).$$

The entries of matrix $\mathbf{A}$ depend on the timing phase of the T-spaced samples taken at the output of the pulse generator. In a practical system, the sampler timing phase is determined by the synchronization process in the receiver. Suppose that the taps just happen to have equal strength, $|g_0(t)|^2 = |g_1(t)|^2$, when the sampler timing is being determined, that is, during the training sequence or synchronization word. Furthermore, for the purpose of illustration, suppose that the result of the sampler timing phase adjustment is such that the symbol-spaced taps have equal strength as well, that is, $|g_0^T(t)|^2 = |g_1^T(t)|^2$. Figure 2.49 illustrates this situation. The entries of matrix $\mathbf{A}$ can be obtained by writing

$$g_0^T(t) = p(\tau_s/2 - T/2)g_0(t) + p(-\tau_s/2 - T/2)g_1(t),$$
$$g_1^T(t) = p(\tau_s/2 + T/2)g_0(t) + p(-\tau_s/2 + T/2)g_1(t).$$

$g_0(t) p(\tau/2 - T/2)$

$g_1(t) p(-\tau/2 - T/2)$

$g_1(t) p(-\tau/2 + T/2)$

$g_0(t) p(\tau/2 + T/2)$

$\dfrac{\tau}{2} - \dfrac{T}{2}$ $\dfrac{\tau}{2} + \dfrac{T}{2}$
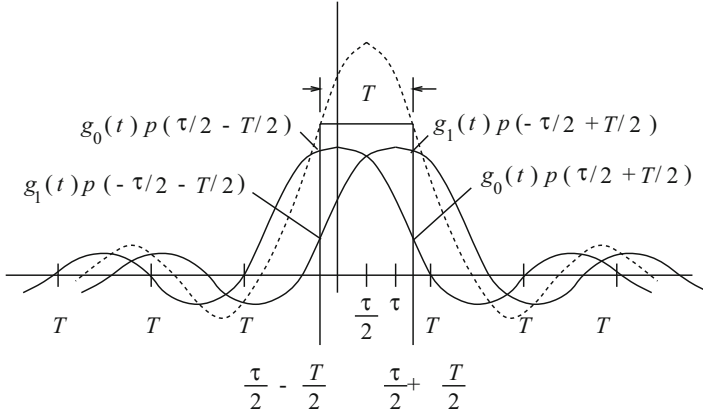
Fig. 2.49 Generation symbol-spaced channel taps

Hence,
$$\mathbf{A} = \begin{bmatrix} p(\tau_s/2 - T/2) \ p(-\tau_s/2 - T/2) \\ p(\tau_s/2 + T/2) \ p(-\tau_s/2 + T/2) \end{bmatrix}.$$

Now suppose that the combination of the transmitter and receiver filter is a raised cosine pulse,[4]

$$p(t) = \mathrm{sinc}(t/T) \cdot \frac{\cos(\pi \beta t/T)}{1 - 4\beta^2 t^2/T^2} \tag{2.287}$$

with roll-off factor $\beta = 0.35$, and $\tau_s = T/4$. Then we have

$$\mathbf{A} = \begin{bmatrix} p(-3T/8) \ p(-5T/8) \\ p(5T/8) \quad p(3T/8) \end{bmatrix} = \begin{bmatrix} 0.7717 \ 0.4498 \\ 0.4498 \ 0.7717 \end{bmatrix}$$

2.6   Shadowing

We have seen earlier in (2.24) that the received envelope power is

$$\Omega_{\mathrm{p}} = \mathrm{E}[|g(t)|^2] = \sum_{n=1}^{N} C_n^2, \tag{2.288}$$

---

[4]See Chap. 4 for a discussion of raised cosine pulse shaping.

where C_n depends on the cross-sectional area of the nth local scatterer. In practice, the local mean is calculated by computing the time average

$$\hat{\Omega}_p = \frac{1}{T} \int_T |g(t)|^2 dt, \tag{2.289}$$

where the time interval T is chosen to correspond to a spatial averaging interval that is large enough to average over the envelope fades. In practice, this corresponds to a spatial averaging distance of about 20 wavelengths. Note that the required averaging interval T will depend on velocity. The averaging interval must be small enough so that the $\{C_n\}$ do not change over the averaging interval. The location area is defined as the largest volume of space where this condition will hold true. Sometimes Ω_p is called the local mean because it is computed within a location area. If the receiver moves outside the location area, the $\{C_n\}$ will change due to the presence of large terrain features such as hills, valley, and buildings. Therefore, the local mean Ω_p (or $\hat{\Omega}_p$) changes with location in a process known as shadowing. The same statements can also be made for the mean envelope $\Omega_v = \mathrm{E}[|g(t)|]$ and its time average

$$\hat{\Omega}_v = \frac{1}{T} \int_T |g(t)| dt. \tag{2.290}$$

Empirical studies have shown that Ω_v and Ω_p have the log-normal distributions

$$p_{\Omega_v}(x) = \frac{2}{x \sigma_\Omega \xi \sqrt{2\pi}} \exp \left\{ -\frac{\left(10\log_{10}\{x^2\} - \mu_{\Omega_v \ (\mathrm{dBm})} \right)^2}{2\sigma_\Omega^2} \right\}, \tag{2.291}$$

$$p_{\Omega_p}(x) = \frac{1}{x \sigma_\Omega \xi \sqrt{2\pi}} \exp \left\{ -\frac{\left(10\log_{10}\{x\} - \mu_{\Omega_p \ (\mathrm{dBm})} \right)^2}{2\sigma_\Omega^2} \right\}, \tag{2.292}$$

where

$$\mu_{\Omega_v \ (\mathrm{dBm})} = 30 + 10\mathrm{E}[\log_{10}\{\Omega_v^2\}], \tag{2.293}$$

$$\mu_{\Omega_p \ (\mathrm{dBm})} = 30 + 10\mathrm{E}[\log_{10}\{\Omega_p\}], \tag{2.294}$$

σ_Ω is the shadow standard deviation in decibel units, and $\xi = \ln(10)/10$. The mean values $\mu_{\Omega_v \ (\mathrm{dBm})}$ and $\mu_{\Omega_p \ (\mathrm{dBm})}$ are sometimes called the area mean because they correspond to an extended location area defined as the largest volume of space where the $\{C_n\}$ can be characterized as stationary random variables and N is a constant. Within an extended location area, the mean envelope power $\mu_{\Omega_p} = \mathrm{E}[\Omega_p]$ and mean envelope $\mu_{\Omega_v} = \mathrm{E}[\Omega_v]$ are constant. These quantities will depend on the propagation path loss between the transmitter and receiver, so that the path loss is constant within the extended location area.

Using a transformation of random variables, it can be shown that $\Omega_{v \text{ (dBm)}} = 30 + 10\log_{10}\{\Omega_v^2\}$ and $\Omega_{p \text{ (dBm)}} = 30 + 10\log_{10}\{\Omega_p\}$ have the respective Gaussian densities

$$p_{\Omega_{v \text{ (dBm)}}}(x) = \frac{1}{\sqrt{2\pi}\sigma_\Omega}\exp\left\{-\frac{\left(x - \mu_{\Omega_{v \text{ (dBm)}}}\right)^2}{2\sigma_\Omega^2}\right\}, \qquad (2.295)$$

$$p_{\Omega_{p \text{ (dBm)}}}(x) = \frac{1}{\sqrt{2\pi}\sigma_\Omega}\exp\left\{-\frac{\left(x - \mu_{\Omega_{p \text{ (dBm)}}}\right)^2}{2\sigma_\Omega^2}\right\}. \qquad (2.296)$$

Note that the logarithm of the log-normal random variable yields a normal random variable.

Some confusion may arise when reading the literature because some authors [100, 101, 185] treat the mean envelope Ω_v as being log-normally distributed with shadow standard deviation σ_Ω, while other authors [163, 180, 214] treat the mean square envelope Ω_p as being log-normally distributed with the same value of σ_Ω. Clearly, the mean envelope and mean square envelope are not the same, and we question whether the same shadow standard deviation should be used in each case. It is shown in Appendix 3 that the shadow standard deviation σ_Ω is indeed the same in each case. However, with Ricean fading the means differ by

$$\mu_{\Omega_{p \text{ (dBm)}}} = \mu_{\Omega_{v \text{ (dBm)}}} + 10\log_{10}\{C(K)\}, \qquad (2.297)$$

where

$$C(K) = \frac{4\mathrm{e}^{2K}(K+1)}{\pi_1 F_1^2(3/2, 1; K)} \qquad (2.298)$$

and $_1F_1(\cdot, \cdot; \cdot)$ denotes the confluent hypergeometric function.

The shadow standard deviation σ_Ω ranges from 5 to 12 dB with 8 dB being a typical value for macrocellular applications. The shadow standard deviation increases slightly with frequency (0.8 dB higher at 1,800 MHz than at 900 MHz), but has been observed to be nearly independent radio path length, even for distances that are very close to the transmitter [180]. The shadow standard deviation that is observed in microcells varies between 4 and 13 dB [33, 113, 115, 171, 181, 223]. Mogensen [181] has reported $\sigma_\Omega = 6.5$ to 8.2 dB at 900 MHz in urban areas, while Mockford et. al. [180] report a value of 4.5 dB for urban areas. Berg [33] and Goldsmith and Greenstein [115] report that σ_Ω is around 4 dB for a spatial averaging window of 20 wavelengths and BS antenna heights of about 10 m. Several studies suggest that σ_Ω decreases with an increase in the degree of urbanization or density of scatters. For example, the results presented by Mockford et. al. [180] suggest that σ_Ω is 1.3 to 1.8 dB higher in a suburban environment than in an urban environment.

2.6.1 Shadow Simulation

One of the challenges when constructing a shadow simulator is to account for the spatial correlation of the shadows. Several studies have investigated the spatial correlation of shadows [121, 122, 129, 133, 171]. One simple model has been suggested by Gudmundson [122], where log-normal shadowing is modeled as a Gaussian white noise process that is filtered by a first-order low-pass filter. With this model,

$$\Omega_{k+1 \text{ (dBm)}} = \zeta \Omega_{k \text{ (dBm)}} + (1 - \zeta) v_k, \tag{2.299}$$

where $\Omega_{k \text{ (dBm)}}$ is the mean envelope or mean squared envelope, expressed in decibels, that is experienced at index k, ζ is a parameter that controls the spatial correlation of the shadows, and v_k is a zero-mean Gaussian random variable with $\phi_{vv}(n) = \tilde{\sigma}^2 \delta(n)$. It can be shown that the spatial autocorrelation function of $\Omega_{k \text{ (dBm)}}$ as generated by (2.299) is

$$\phi_{\Omega_{(\text{dBm})}\Omega_{(\text{dBm})}}(k) = \frac{1 - \zeta}{1 + \zeta} \tilde{\sigma}^2 \zeta^{|k|}. \tag{2.300}$$

Since the shadow variance is

$$\sigma_\Omega^2 = \phi_{\Omega_{(\text{dBm})}\Omega_{(\text{dBm})}}(0) = \frac{1 - \zeta}{1 + \zeta} \tilde{\sigma}^2, \tag{2.301}$$

we can express the autocorrelation of Ω_k as

$$\phi_{\Omega_{(\text{dBm})}\Omega_{(\text{dBm})}}(k) = \sigma_\Omega^2 \zeta^{|k|}. \tag{2.302}$$

This approach generates shadows that decorrelate exponentially with distance. It is interesting to note that Mandayam et. al. [169] have shown through an extreme value analysis that log-normal shadows cannot decorrelate exponentially with distance. Nevertheless, in the absence of a better solution, Gudmundson's model in (2.299) is still useful and effective.

While shadows decorrelate spatially, simulations are usually conducted in discrete time. Therefore, to use the simulator in (2.299), we must relate the spatial decorrelation parameter ζ to the simulation index k. Suppose that we wish to model the shadows that are experienced by a MS that is traveling with velocity v. The envelope (or squared envelope) is sampled every T seconds. In kT seconds the MS moves a distance vkT. Let ζ_D be the shadow correlation between two points separated by a distance of D m. Then the time autocorrelation of shadowing is

$$\phi_{\Omega_{(\text{dBm})}\Omega_{(\text{dBm})}}(k) \equiv \phi_{\Omega_{(\text{dBm})}\Omega_{(\text{dBm})}}(kT) = \sigma_\Omega^2 \zeta_D^{(vT/D)|k|}. \tag{2.303}$$

Comparing (2.302) and (2.303) we see that $\zeta = \zeta_D^{(vT/D)}$. For typical suburban propagation at 900 MHz, it has been experimentally verified by Gudmundson [120] that $\sigma_\Omega \approx 7.5$ dB and $\zeta_{100} = 0.82$. For typical microcellular propagation at 1,700 MHz, Gudmundson has also reported $\sigma_\Omega = 4.3$ dB and $\zeta_{10} = 0.3$.

2.6.2   Composite Shadowing-Fading Distributions

Sometimes it is desirable to obtain the composite envelope distribution due to shadowing and multipath fading. Such a composite distribution is relevant in cases where the MSs are slowly moving or stationary. In this case, the fading rate may be so slow that entire codewords are either faded completely or not at all regardless of the interleaving depth that is used, and the code fails. In this case, the composite shadow-fading distribution is useful for evaluating system coverage, that is, the fraction of the service area having an acceptable quality of service.

Two different approaches have been suggested in the literature for obtaining the composite distribution. The first approach is to express the envelope (or squared envelope) as a conditional density, conditioned on Ω_v (or Ω_p), and then integrate over the density of Ω_v (or Ω_p) to obtain the composite distribution. This results in the composite squared envelope distribution

$$p_{\alpha_c^2}(x) = \int_0^\infty p_{\alpha^2|\,\Omega_p}(x|w) p_{\Omega_p}(w) dw. \tag{2.304}$$

For the case of Rayleigh fading, at any time t_1

$$\Omega_p = \mathrm{E}[\alpha^2(t_1)] = 2b_0 \tag{2.305}$$

and, hence,

$$p_{\alpha^2|\,\Omega_p}(x|w) = \frac{x}{w} e^{-x/w}. \tag{2.306}$$

The composite squared envelope distribution with Rayleigh fading and log-normal shadowing is

$$p_{\alpha_c^2}(x) = \int_0^\infty \frac{1}{w} e^{-x/w} \times \frac{1}{w\sigma_\Omega \xi \sqrt{2\pi}} \exp\left\{ -\frac{\left(10\log_{10}\{w\} - \mu_{\Omega_p \text{ (dBm)}}\right)^2}{2\sigma_\Omega^2} \right\} dw,$$

$$\tag{2.307}$$

where $\xi = \ln(10)/10$. Unfortunately, this distribution does not exist in closed form, but can be efficiently evaluated using Gauss–Hermite quadrature integration.

The second approach, originally suggested by Lee and Yeh [155], expresses the composite received envelope as the product of the envelope due to multipath fading and shadow fading. Using this approach, the envelope of the composite signal has the product form

$$\hat{\alpha}_c(t) = \alpha(t) \cdot \Omega_v(t), \tag{2.308}$$

while the squared envelope of the composite signal has the product form

$$\hat{\alpha}_c^2(t) = \alpha^2(t) \cdot \Omega_p(t). \tag{2.309}$$

Under the assumption that the fading and shadowing are independent random processes, we now show that both approaches lead to identical results. The composite envelope in (2.309) is the product of two random variables at any time t_1. Hence, the corresponding density function can be obtained using a bivariate transformation and then integrating to obtain the marginal density. This leads to the density

$$p_{\hat{\alpha}_c^2}(x) = \int_0^\infty \frac{1}{w} p_{\alpha^2}\left(\frac{x}{w}\right) p_{\Omega_p}(w) dw. \tag{2.310}$$

Again, consider the case of log-normal shadowing and Rayleigh fading. Using (2.50) and (2.291) gives

$$p_{\hat{\alpha}_c^2}(x) = \int_0^\infty \frac{1}{\Omega_p w} \exp\left\{-\frac{x}{\Omega_p w}\right\}$$

$$\times \frac{1}{w\sigma_\Omega \xi \sqrt{2\pi}} \exp\left\{-\frac{\left(10\log_{10}\{w\} - \mu_{\Omega_p \, (\text{dBm})}\right)^2}{2\sigma_\Omega^2}\right\} dw. \tag{2.311}$$

Observe that (2.307) and (2.311) are related by

$$p_{\alpha_c}(x) = \Omega_p p_{\hat{\alpha}_c}\left(\Omega_p x\right). \tag{2.312}$$

Hence, if we assume that the faded envelope $\alpha(t)$ in the second approach has $\text{E}[\alpha(t)^2] = \Omega_p = 1$, then α_c^2 and $\hat{\alpha}_c^2$ will have the exact same composite distribution. Although the above result may not matter much for analysis, it does have implications for software simulation. When simulating the combined effects of fading and shadowing, we can generate the composite envelope or squared envelope by generating the fading and shadowing processes separately and multiplying them together as shown in (2.308) and (2.309), respectively. To do so, the faded envelope should be generated such that $\Omega_v = 1$ or $\Omega_p = 1$ as appropriate.

2.6.2.1   Composite Gamma-Log-Normal Distribution

It is sometimes very useful to model the radio propagation environment as a shadowed Nakagami fading channel, because the Nakagami distribution is mathematically convenient and can closely approximate a Rice distribution. The composite distribution of the squared-envelope due to Nakagami fading and log-normal shadowing has the Gamma-log-normal density function

$$p_{\alpha_c^2}(x) = \int_0^\infty \left(\frac{m}{w}\right)^m \frac{x^{m-1}}{\Gamma(m)} \exp\left\{-\frac{mx}{w}\right\}$$

$$\times \frac{1}{\sqrt{2\pi}\xi\sigma_\Omega w} \exp\left\{-\frac{(10\log_{10}\{w\} - \mu_{\Omega_{p \text{ (dBm)}}})^2}{2\sigma_\Omega^2}\right\} dw, \quad (2.313)$$

where $\xi = \ln(10)/10$. As shown in Appendix 4, the composite Gamma-log-normal distribution in (2.313) can be approximated by a log-normal distribution with parameters

$$\mu_{\text{(dBm)}} = \xi^{-1}\left(\psi(m) - \ln(m)\right) + \mu_{\Omega_{p \text{ (dBm)}}}$$

$$\sigma^2 = \xi^{-2}\zeta(2,m) + \sigma_\Omega^2, \quad (2.314)$$

where $\psi(\cdot)$ is the Euler psi function and $\zeta(\cdot,\cdot)$ is Riemann's zeta function as defined in Appendix 4. When $m = 1$, the approximation is valid for $\sigma_\Omega > 6$ dB; when $m = 2$, $\sigma_\Omega > 6$ must be greater than or equal to 4 dB; when $m \geq 4$, the approximation is good for all σ_Ω [131].

The effect of Nakagami fading in (2.314) is to decrease the mean and increase the variance of the composite envelope. However, this effect decreases as the shape factor m increases (corresponding to less severe fading). For example, with $m = 1$ (Rayleigh fading) we have $\mu_{\text{(dBm)}} = \mu_{\Omega_{p \text{ (dBm)}}} - 2.50675$ and $\sigma^2 = \sigma_\Omega^2 + 31.0215$, while with $m = 8$ we have $\mu_{\text{(dBm)}} = \mu_{\Omega_{p \text{ (dBm)}}} - 0.277$ and $\sigma^2 = \sigma_\Omega^2 + 2.50972$.

2.7   Path Loss Models

Path loss is the largest and most variable quantity in a communication link budget. It depends on frequency, antenna heights, and distance and topography. A variety of theoretical and empirical path loss models exist in the literature. We start with a discussion of theoretical models followed by empirical models.

2.7.1   Free Space Path Loss

Free-space path loss (FSPL) is proportional to the square of the distance between the transmitter and receiver, and also proportional to the square of the frequency of the radio signal. The FSPL equation is

$$L_{FS} = \left(\frac{4\pi d}{\lambda_c} \right)^2.$$
(2.315)

FSPL is a combination of two effects: First, the intensity of an electromagnetic wave in free space decays with the square of the radio path length, d, such that the received power per unit area or power spatial density (in watts per meter square) at distance d is

$$\Omega_r(d) = \Omega_t \frac{1}{4\pi d^2},$$
(2.316)

where Ω_t is the total transmit power in watts. Note that this term is not frequency dependent.

The second effect is due to aperture, which determines how well an antenna picks up power from an incoming electromagnetic wave. For an isotropic antenna, we have

$$\Omega_p(d) = \Omega_r(d) \frac{\lambda_c^2}{4\pi},$$
(2.317)

where $\Omega_p(d)$ is the received power. Note that this is entirely dependent on wavelength, λ_c, which is how the frequency-dependent behavior arises.

Using (2.316) and (2.317) gives the free space propagation path loss as

$$L_{FS\ (dB)} = 10\log_{10}\left\{ \frac{\Omega_t}{\Omega_p(d)} \right\} = 10\log_{10}\left\{ \left(\frac{4\pi d}{\lambda_c} \right)^2 \right\}$$

$$= 10\log_{10}\left\{ \left(\frac{4\pi d}{c/f_c} \right)^2 \right\}$$

$$= 20\log_{10}\{f_c\} + 20\log_{10}\{d\} - 147.55\ \text{dB}.$$
(2.318)

2.7.2   Flat Earth Path Loss

The signals in land mobile radio environments do not experience free space propagation. A more appropriate theoretical model assumes propagation over a flat reflecting surface (the earth) as shown in Fig. 2.50. The length of the direct path is
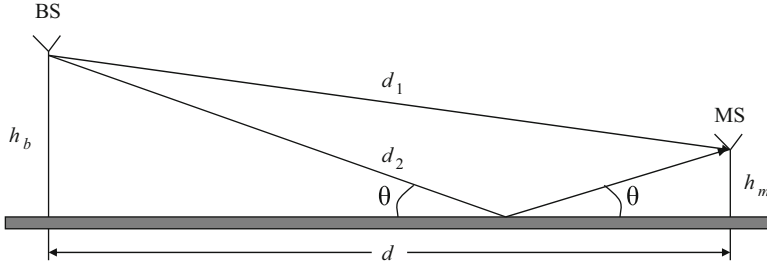
$$d_1 = \sqrt{d^2 + (h_b - h_m)^2}$$
(2.319)

Fig. 2.50 Radio propagation over a flat reflecting surface

and the length of the reflected path is

$$d_2 = \sqrt{d^2 + (h_b + h_m)^2}. \tag{2.320}$$

Given that $d \gg h_b h_m$, we have $d_1 \approx d$ and $d_2 \approx d$. However, since the wavelength is small, the direct and reflected paths may add constructively or destructively over small distances. The carrier phase difference between the direct and reflected paths is

$$\phi_2 - \phi_1 = \frac{2\pi}{\lambda_c}(d_2 - d_1). \tag{2.321}$$

Taking into account the phase difference, the received envelope power is

$$\mu_{\Omega_p} = \Omega_t \left(\frac{\lambda_c}{4\pi d}\right)^2 \left|1 + a e^{-jb} e^{j(\phi_2 - \phi_1)}\right|^2, \tag{2.322}$$

where a and b are the amplitude attenuation and phase change introduced by the flat reflecting surface. If we assume a perfect specular reflection, then $a = 1$ and $b = \pi$ for small θ and

$$\mu_{\Omega_p} = \Omega_t \left(\frac{\lambda_c}{4\pi d}\right)^2 \left|1 - e^{j(\frac{2\pi}{\lambda_c}\Delta_d)}\right|^2$$

$$= 4\Omega_t \left(\frac{\lambda_c}{4\pi d}\right)^2 \sin^2\left(\frac{\pi}{\lambda_c}\Delta_d\right), \tag{2.323}$$

where $\Delta_d = (d_2 - d_1)$. Given that $d \gg h_b$ and $d \gg h_m$, and applying the approximation $\sqrt{1+x} \approx 1 + x/2$ for small x to (2.319) and (2.320), we have

$$\Delta_d \approx \frac{2h_b h_m}{d}. \tag{2.324}$$

Fig. 2.51 Propagation path loss with distance over a flat reflecting surface; $h_b = 7.5$ m, $h_m = 1.5$ m, $f_c = 1,800$ MHz
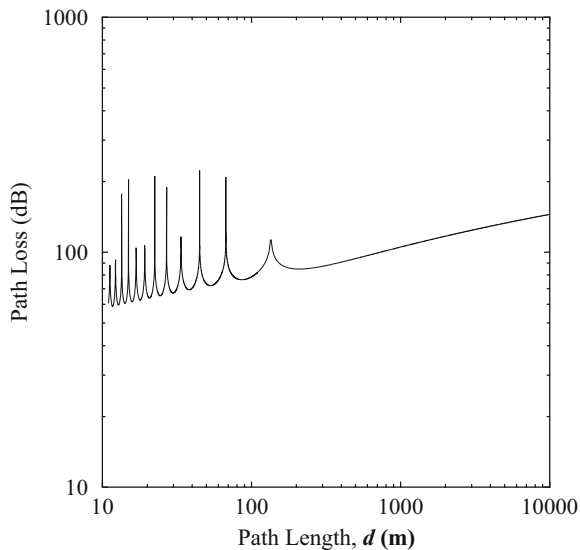
Finally, the received envelope power is

$$\mu_{\Omega_p} \approx 4\Omega_t \left(\frac{\lambda_c}{4\pi d} \right)^2 \sin^2 \left(\frac{2\pi h_b h_m}{\lambda_c d} \right), \qquad (2.325)$$

where h_b and h_m are the heights of the BS and MS antennas, respectively. Under the condition that $d \gg h_b h_m$, (2.325) reduces to

$$\mu_{\Omega_p} \approx \Omega_t \left(\frac{h_b h_m}{d^2} \right)^2, \qquad (2.326)$$

where we have invoked the small angle approximation $\sin x \approx x$ for small x. Observe that when $d \gg h_b h_m$, the propagation over a flat reflecting surface differs from free space propagation in two ways. First, the path loss is not frequency dependent and, second, the envelope power decays with the fourth power of the distance rather than the square of the distance. Finally, the model in (2.326) shows how changes in the BS and MS antenna heights will affect the path loss.

Figure 2.51 plots the flat Earth path loss (FEPL)

$$L_{\text{FE (dB)}} = 10\log_{10}\left\{ \frac{\Omega_t}{\mu_{\Omega_p}} \right\} = -10\log_{10}\left\{ 4\left(\frac{\lambda_c}{4\pi d} \right)^2 \sin^2\left(\frac{2\pi h_b h_m}{\lambda_c d} \right) \right\} \text{dB}$$

$$(2.327)$$

against the distance d. Notice that the path loss and, hence, the received envelope power have alternate minima and maxima when the path length is small. This property has been noted in experiments by Milstein et. al. [178]. The last local maxima in the path loss occurs when

$$\frac{2\pi h_{\mathrm{b}} h_{\mathrm{m}}}{\lambda_{\mathrm{c}} d} = \frac{\pi}{2}.$$

2.7.3 Empirical Path Loss Models

Several highly useful empirical models for macrocellular systems have been obtained by curve fitting experimental data. Two of the more useful models for 900 MHz cellular systems are Hata's model [197] based on Okumura's prediction method [129], and Lee's model [153].

### 2.7.3.1 Okumura–Hata and CCIR Models

Hata's empirical model [129] is probably the simplest to use and can distinguish between man-made structures. The empirical data for this model was collected by Okumura [197] in the city of Tokyo. The Okumura–Hata model is expressed in terms of the carrier frequency $150 \leq f_{\mathrm{c}} \leq 1{,}000\,(\mathrm{MHz})$, BS antenna height $30 \leq h_{\mathrm{b}} \leq 200\,(\mathrm{m})$, the MS antenna height $1 \leq h_{\mathrm{m}} \leq 10\,(\mathrm{m})$, and the distance $1 \leq d \leq 20\,(\mathrm{km})$ between the BS and MS. Note the units of the parameters that are used in the model. The model is known to match the experimental data from which is formed to within 1 dB for distances ranging from 1 to 20 km. With the Okumura–Hata model, the path loss between two isotropic BS and MS antennas is:

$$L_{\mathrm{p\,(dB)}} = \begin{cases} A + B\log_{10}\{d\} & \text{for urban area} \\ A + B\log_{10}\{d\} - C & \text{for suburban area} \\ A + B\log_{10}\{d\} - D & \text{for open area} \end{cases}, \qquad (2.328)$$

where

$$A = 69.55 + 26.16\log_{10}\{f_{\mathrm{c}}\} - 13.82\log_{10}\{h_{\mathrm{b}}\} - a(h_{\mathrm{m}}),$$
$$B = 44.9 - 6.55\log_{10}\{h_{\mathrm{b}}\},$$
$$C = 5.4 + 2\left(\log_{10}\{f_{\mathrm{c}}/28\}\right)^2,$$
$$D = 40.94 + 4.78\left(\log_{10}\{f_{\mathrm{c}}\}\right)^2 - 18.33\log_{10}\{f_{\mathrm{c}}\}. \qquad (2.329)$$

Fig. 2.52 Path loss obtained from the Okumura–Hata model; $h_b = 70$ m, $h_m = 1.5$ m, $f_c = 900$ Mhz
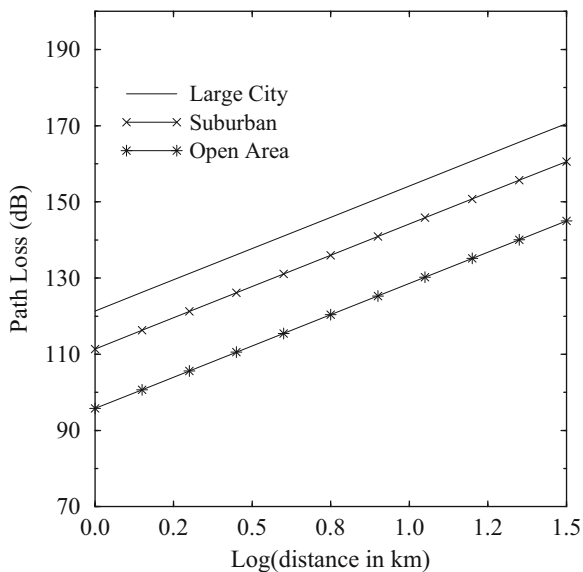
and

$$
a(h_m) = \begin{cases}
(1.1\log_{10}\{f_c\} - 0.7)h_m - (1.56\log_{10}\{f_c\} - 0.8) \\
\qquad\qquad\qquad\qquad\qquad \text{for medium or small city} \\[2ex]
\begin{cases}
8.28\,(\log_{10}\{1.54h_m\})^2 - 1.1 & \text{for } f_c \leq 200\,\text{MHz} \\
3.2\,(\log_{10}\{11.75h_m\})^2 - 4.97 & \text{for } f_c \geq 400\,\text{MHz} \\
\qquad\qquad \text{for large city}
\end{cases}
\end{cases}
\tag{2.330}
$$

Typical values from the Okumura–Hata "large city" model are plotted in Fig. 2.52, for a BS height of 70 m, a MS antenna height of 1.5 m, and a carrier frequency of 900 MHz. The reader is cautioned that, due to a lesser degree of urbanization, the path losses for Japanese suburban areas do not match North American suburban areas very well. The latter are more like the quasi-open areas in Japan. In addition, the North American urban areas have path losses more like the Japanese suburban areas.

To account for varying degrees of urbanization, the Comité International des Radio-Communication, now ITU-R (CCIR) developed an empirical model for the path loss as:

$$
L_{p\,\text{(dB)}} = A + B\log_{10}\{d\} - E,
\tag{2.331}
$$

where A and B are defined in (2.329) with $a(h_m)$ being the medium or small city value in (2.330). The parameter E accounts for the degree of urbanization and is given by

$$E = 30 - 25\log_{10}\{\% \text{ of area covered by buildings}\}, \qquad (2.332)$$

where $E = 0$ when the area is covered by approximately 16% buildings.

2.7.3.2 Lee's Area-to-Area Model

Lee's area-to-area model [153] is used to predict a path loss over flat terrain. If the actual terrain is not flat, for example, hilly, there will be large prediction errors. Two parameters are required for Lee's area-to-area model; the power at a 1 mile (1.6 km) point of interception, $\mu_{\Omega_p}(d_o)$, and the path-loss exponent, β. The received signal power at distance d can be expressed as

$$\mu_{\Omega_p}(d) = \mu_{\Omega_p}(d_o)\left(\frac{d}{d_o}\right)^{-\beta}\left(\frac{f}{f_o}\right)^{-n}\alpha_0 \qquad (2.333)$$

or in decibel units

$$\mu_{\Omega_p \text{ (dBm)}}(d) = \mu_{\Omega_p \text{ (dBm)}}(d_o) - 10\beta\log_{10}\left\{\frac{d}{d_o}\right\} - 10n\log_{10}\left\{\frac{f}{f_o}\right\} + 10\log_{10}\{\alpha_0\}, \qquad (2.334)$$

where d is in units of kilometers and $d_o = 1.6$ km. The parameter α_0 is a correction factor used to account for different BS and MS antenna heights, transmit powers, and antenna gains. The following set of *nominal* conditions are assumed in Lee's area-to-area model:

- Frequency $f_o = 900$ MHz
- BS antenna height $= 30.48$ m
- BS transmit power $= 10$ W
- BS antenna gain $= 6$ dB above dipole gain
- MS antenna height $= 3$ m
- MS antenna gain $= 0$ dB above dipole gain

If the actual conditions are different from those listed above, then we compute the following parameters:

$$\alpha_1 = \left(\frac{\text{BS antenna height (m)}}{30.48 \text{ m}}\right)^2,$$

$$\alpha_2 = \left(\frac{\text{MS antenna height (m)}}{3 \text{ m}}\right)^\kappa,$$

$$\alpha_3 = \frac{\text{transmitter power}}{10 \text{ W}},$$

$$\alpha_4 = \frac{\text{BS antenna gain with respect to } \lambda_c/2 \text{ dipole}}{4},$$

$$\alpha_5 = \text{different antenna-gain correction factor at the MS.} \qquad (2.335)$$

Table 2.2 Parameters for Lee's area-to-area model in various propagation environments, from [153]

Terrain	$\mu_{\Omega_{\text{p (dBm)}}}(d_o)$	β
Free space	-45	2
Open area	-49	4.35
North American suburban	-61.7	3.84
North American urban (Philadelphia)	-70	3.68
North American urban (Newark)	-64	4.31
Japanese urban (Tokyo)	-84	3.05

From these parameters, the correction factor α_0 is

$$\alpha_0 = \alpha_1 \cdot \alpha_2 \cdot \alpha_3 \cdot \alpha_4 \cdot \alpha_5. \tag{2.336}$$

The parameters β and $\mu_{\Omega_{\text{p}}}(d_o)$ have been found from empirical measurements and are listed in Table 2.2.

Experimental data suggest that n in (2.334) ranges between 2 and 3 with the exact value depending upon the carrier frequency and the geographic area. For $f_{\text{c}} < 450\,\text{MHz}$ in a suburban or open area, $n = 2$ is recommended. In an urban area with $f_{\text{c}} > 450\,\text{MHz}$, $n = 3$ is recommended. The value of κ in (2.335), also determined from empirical data, is

$$\kappa = \begin{cases} 2 \text{ for a MS antenna height } > 10\,\text{m} \\ 3 \text{ for a MS antenna height } < 3\,\text{m} \end{cases}. \tag{2.337}$$

The path loss $L_{\text{p (dB)}}$ is the difference between the transmitted and received envelope power, $L_{\text{p (dB)}} = \mu_{\Omega_{\text{p (dBm)}}}(d) - \mu_{\Omega_{\text{t (dBm)}}}$. To compare directly with the Okumura–Hata model in Fig. 2.52, we assume an isotropic BS antenna with $0\,\text{dB}$ gain, so that $\alpha_4 = -6\,\text{dB}$. Then using the same parameters as in Fig. 2.52, $h_{\text{b}} = 70\,\text{m}$, $h_{\text{m}} = 1.5\,\text{m}$, $f_{\text{c}} = 900$ MHz, a nominal BS transmitter power of $40\,\text{dBm}$ (10 W), and the parameters in Table 2.2 for $\mu_{\Omega_{\text{p (dBm)}}}(d_o)$ and β, the following path losses are obtained:

$$L_{\text{p (dB)}} = \begin{cases} 85.74 + 20.0\log_{10}\{d\} & \text{Free Space} \\ 84.94 + 43.5\log_{10}\{d\} & \text{Open Area} \\ 98.68 + 38.4\log_{10}\{d\} & \text{Suburban} \\ 107.31 + 36.8\log_{10}\{d\} & \text{Philadelphia} \\ 100.02 + 43.1\log_{10}\{d\} & \text{Newark} \\ 122.59 + 30.5\log_{10}\{d\} & \text{Tokyo} \end{cases}. \tag{2.338}$$

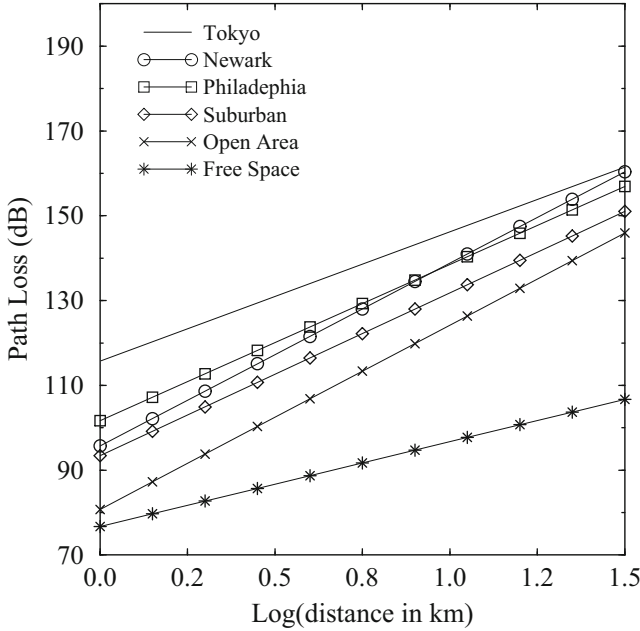These typical values from Lee's area-to-area model are plotted in Fig. 2.53.

Fig. 2.53 Path loss obtained using Lee's method; $h_b = 70$ m, $h_m = 1.5$ m, $f_c = 900$ MHz, and an isotropic BS antenna

2.7.3.3   COST231–Hata Model

The COST231–Hata model is based on the proposal by Mogensen [181] et. al. to extend the Okumura–Hata model for use in the 1,500–2,000 MHz frequency range, where it is known that the Okumura–Hata model underestimates the path loss. The COST231–Hata model is expressed in terms of the carrier frequency $1,500 \leq f_c \leq 2,000$ (MHz), BS antenna height $30 \leq h_b \leq 200$ (m), MS antenna height $1 \leq h_m \leq 10$ (m), and distance $1 \leq d \leq 20$ (km). Note again that the parameters must be used with the proper units in the model. The path loss predicted by the COST231–Hata model is [65]

$$L_{p \text{ (dB)}} = A + B\log_{10}\{d\} + C, \tag{2.339}$$

where

$$A = 46.3 + 33.9\log_{10}\{f_c\} - 13.82\log_{10}\{h_b\} - a(h_m),$$

$$B = 44.9 - 6.55\log_{10}\{h_b\},$$

$$C = \begin{cases} 0 & \text{medium city and suburban areas} \\ & \quad \text{with moderate tree density} \\ 3 & \text{for metropolitan centers} \end{cases}.$$

Although both the Okumura and Hata and the COST231–Hata models are limited to BS antenna heights greater than 30 m, they can be used for lower BS antenna heights provided that the surrounding buildings are well below the BS antennas. They should not be used to predict path loss in urban canyons. The COST231–Hata model is good down to a path length of 1 km. They should not be used for smaller ranges, where path loss becomes highly dependent upon the local topography.

2.7.3.4   COST231–Walfish–Ikegami Model

The COST231–Walfish–Ikegami model was developed for microcellular systems and distinguishes between LoS and NLoS propagation. The model is accurate for carrier frequencies in the range $800 \leq f_c \leq 2000$ (MHz), and path distances in the range $0.02 \leq d \leq 5$ (km).

LoS propagation

For LoS propagation in a street canyon, the path loss is

$$L_{\text{p (dB)}} = 42.6 + 26\log_{10}\{d\} + 20\log_{10}\{f_c\}, \quad d \geq 20\,\text{m}, \tag{2.340}$$

where the first constant is chosen so that L_p is equal to the FSPL at a distance of 20 m. The model parameters are the distance d (km) and carrier frequency f_c (MHz).

NLoS propagation

As defined in Fig. 2.54, the path loss for NLoS propagation is expressed in terms of the following parameters:

$$d = \text{distance (m)},$$

$$h_b = \text{BS antenna height over street level, } 4 \leq h_b \leq 50 \ (\text{m}),$$

$$h_m = \text{MS antenna height over street level, } 1 \leq h_m \leq 3 \,(\text{m}),$$

$$h_{\text{Roof}} = \text{nominal roof height of buildings (m)},$$

$$\Delta h_b = h_b - h_{\text{Roof}} = \text{height of BS relative to rooftops (m)},$$

$$\Delta h_m = h_{\text{Roof}} - h_m = \text{height of MS relative to rooftops (m)},$$

$$w = \text{width of streets (m)},$$

$$b = \text{building separation (m)},$$

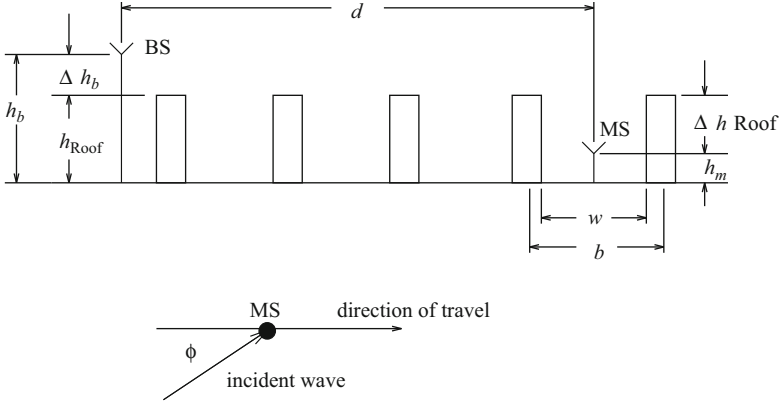$$\phi = \text{angle of incident wave with respect to street (degrees)}.$$

Fig. 2.54 Definition of parameters used in the COST231–Walfish–Ikegami model

If no data on the structure of the buildings and roads are available, the following default values are recommended, $b = 20\ldots50\,(\text{m})$, $w = b/2\,(\text{m})$, $\phi = 90^\circ$, and $h_{\text{Roof}} = 3 \times$ number of floors $+$ roof$\,(\text{m})$, where roof $= 3\,(\text{m})$ pitched and $0\,(\text{m})$ flat.

The NLoS path loss is composed of three terms, viz.,

$$L_{\text{p (dB)}} = \begin{cases} L_o + L_{\text{rts}} + L_{\text{msd}}, & \text{for } L_{\text{rts}} + L_{\text{msd}} \geq 0 \\ L_o, & \text{for } L_{\text{rts}} + L_{\text{msd}} < 0 \end{cases}, \qquad (2.341)$$

where

$$L_o = \text{free-space loss} = 32.4 + 20\log_{10}\{d\} + 20\log_{10}\{f_c\},$$

$$L_{\text{rts}} = \text{roof-top-to-street diffraction and scatter loss},$$

$$L_{\text{msd}} = \text{multiscreen diffraction loss}.$$

Note that the expression for free-space loss differs from (2.318) because here the units of d are in kilometers and the units of f_c are in megahertz. The roof-top-to-street diffraction and scatter loss represent the coupling of the wave propagation along the multiscreen path into the street where the MS is located, and is given by

$$L_{\text{rts}} = -16.9 - 10\log_{10}\{w\} + 10\log_{10}\{f_c\} + 20\log_{10}\{\Delta h_{\text{m}}\} + L_{\text{ori}}, \qquad (2.342)$$

where

$$L_{\text{ori}} = \begin{cases} -10 + 0.354(\phi), & 0 \leq \phi \leq 35^\circ \\ 2.5 + 0.075(\phi - 35^\circ), & 35^\circ \leq \phi \leq 55^\circ \\ 4.0 - 0.114(\phi - 55^\circ), & 55^\circ \leq \phi \leq 90^\circ \end{cases} \qquad (2.343)$$

is a street orientation loss.

The multiscreen diffraction loss is

$$L_{\text{msd}} = L_{\text{bsh}} + k_a + k_d \log_{10}\{d\} + k_f \log_{10}\{f_c\} - 9\log_{10}\{b\}, \qquad (2.344)$$

where

$$L_{\text{bsh}} = \begin{cases} -18\log_{10}\{1 + \Delta h_b\}, & h_b > h_{\text{Roof}} \\ 0, & h_b \le h_{\text{Roof}} \end{cases} \qquad (2.345)$$

is the shadowing gain (negative loss) for cases when the BS antenna is above the rooftops. The parameters k_a and k_d depend on the path length, d, and base station elevation with respect to the rooftops, Δh_b. The term k_a accounts for the increase in path loss when the BS antennas are situated below the roof tops of adjacent buildings, and is given by

$$k_a = \begin{cases} 54, & h_b > h_{\text{Roof}} \\ 54 - 0.8\Delta h_b, & d \ge 0.5\,\text{km and } h_b \le h_{\text{Roof}} \\ 54 - 0.8\Delta h_b d/0.5, & d < 0.5\,\text{km and } h_b \le h_{\text{Roof}} \end{cases} \qquad (2.346)$$

The terms k_d and k_f control the dependency of the multiscreen diffraction loss on the distance and frequency, respectively, and are given by

$$k_d = \begin{cases} 18, & h_b > h_{\text{Roof}} \\ 18 - 15\Delta h_b/h_{\text{Roof}}, & h_b \le h_{\text{Roof}} \end{cases}, \qquad (2.347)$$

$$k_f = -4 + \begin{cases} 0.7(f_c/925 - 1), & \text{medium city and suburban} \\ 1.5(f_c/925 - 1), & \text{metropolitan area} \end{cases}. \qquad (2.348)$$

The COST231–Walfish–Ikegami model works best for $h_b \gg h_{\text{Roof}}$. Large prediction errors can be expected for $h_b \approx h_{\text{Roof}}$. The model is poor for $h_b \ll h_{\text{Roof}}$ because the terms in (2.346) do not consider wave guiding in street canyons and diffraction at street corners.

2.7.3.5   Street Microcells

For ranges less than 500 m and antenna heights less than 20 m, some empirical measurements have shown that the received signal strength for LoS propagation along city streets can be described by the two-slope model [119, 128, 137, 214, 270, 282]

$$\mu_{\Omega_p} = \frac{k\Omega_t}{d^a(1 + d/g)^b}, \qquad (2.349)$$

where Ω_t is the transmitted power, k is a constant of proportionality and d (m) is the distance. For small path length distances, free space propagation will prevail so that $a = 2$. The parameter g is called the break point and ranges from 150 to

Table 2.3 Two-slope path
loss parameters obtained by
Harley, from [128]

Base antenna height (m)	a	b	Break point g (m)
5	2.30	−0.28	148.6
9	1.48	0.54	151.8
15	0.40	2.10	143.9
19	−0.96	4.72	158.3

Fig. 2.55 The corner effect
in a street microcell
environment
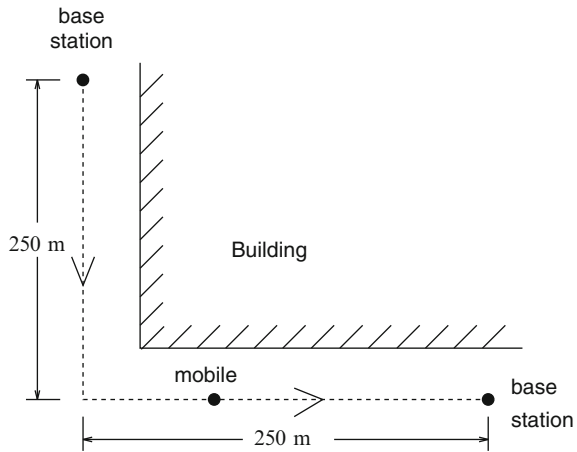
300 m [119, 128, 137, 282]. At larger distances, an inverse-fourth to -eighth power
law is experienced so that b ranges from 2 to 6 [128]. The model parameters that
were obtained by Harley are listed in Table 2.3. Xia [289] has demonstrated that
the break-point occurs where the Fresnel zone between the transmit and receive
antennas just touches the ground assuming a flat surface. This distance is

$$g = \frac{1}{\lambda_c} \sqrt{(\Sigma^2 - \Delta^2)^2 - 2(\Sigma^2 + \Delta^2)\left(\frac{\lambda_c}{2}\right)^2 + \left(\frac{\lambda_c}{2}\right)^4}, \qquad (2.350)$$

where $\Sigma = h_b + h_m$ and $\Delta = h_b - h_m$. For high frequencies, this distance can be
approximated as $g = 4h_b h_m / \lambda_c$, which is the same distance as the last local maxima
in the flat reflecting surface model in Sect. 2.7.2. Notice that the break-point is
dependent on frequency, with the break-point at 1.9 GHz being about twice that
for 900 MHz.

Street microcells may also exhibit NLoS propagation when a MS rounds a street
corner as shown in Fig. 2.55. In this case, the average received signal strength can
drop by as much as 25–30 dB over distances as small as 10 m for low antenna heights
in an area with multistory buildings [51, 164, 186, 226, 257], and by 25–30 dB over
distances of 45–50 m for low antenna heights in a region with only one- or two-story
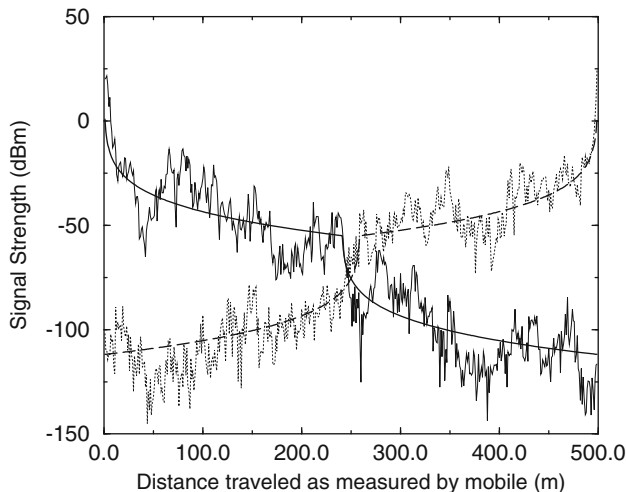buildings [226]. This phenomenon is known as the corner effect.

Fig. 2.56 Received signal strength for the street microcell environment in Fig. 2.55. *Solid lines* show the area mean signal strength, while the *dashed lines* account for shadowing and fading as well. For this latter case, $\sigma_\Omega = 6$ dB and $\phi_{\Omega_{p\ (dBm)}\Omega_{p\ (dBm)}}(d) = 0.1\sigma_\Omega^2$ at $d = 30$ m. For each BS, the received signal strength is shown when the MS is connected to that particular BS and the MS moves along the route in Fig. 2.55

Grimlund and Gudmundson [119] have proposed an empirical street corner path loss model. Their model assumes LoS propagation until the MS reaches a street corner. The NLoS propagation after rounding a street corner is modeled by assuming LoS propagation from a virtual transmitter that is located at the street corner having a transmit power equal to the received power at the street corner from the serving BS. That is, the received signal strength (in dBm) is given by

$$\mu_{\Omega_p} = \begin{cases} \frac{k\Omega_t}{d^a(1+d/g)^b} & d \le d_c \\ \frac{k\Omega_t}{d_c^a(1+d_c/g)^b} \cdot \frac{1}{(d-d_c)^a(1+(d-d_c)/g)^b} & d > d_c \end{cases}, \tag{2.351}$$

where d_c (m) is the distance between the serving BS and the corner. For the scenario depicted in Fig. 2.55, the received signal strength with this model is shown in Fig. 2.56. The heavy curves show the average received signal strength from the two BSs as the MS traverses the dashed path shown in Fig. 2.55. These curves were obtained using $a = 2$, $b = 2$, $g = 150$ m, and $d_c = 250$ m in (2.351), and assuming that $\mu_{\Omega_p} = 1$ dBm at $d = 1$ m. The dotted curves superimposed on the heavy lines in Fig. 2.56 show the received signal strength with the combined effects of path loss, log-normal shadowing, and multipath fading. The latter two were obtained using the simulators described in Sects. 2.6.1 and 2.5.2.2.

Table 2.4 Path loss exponents and shadow standard deviations for several different types of buildings, from [12]

Building	Frequency (MHz)	β	σ_Ω (dB)
Retail stores	914	2.2	8.7
Grocery stores	914	1.8	5.2
Office, hard partition	1,500	3.0	7.0
Office, soft partition	900	2.4	9.6
Office, soft partition	1,900	2.6	14.1

2.7.3.6 Path Loss in Indoor Microcells

The path loss and shadowing characteristics for indoor microcells vary greatly from one building to the next. Typical path loss exponents and shadow standard deviations are provided in Table 2.4 for several different types of buildings.

For multistory buildings, the signal attenuation between floors is important. Measurements have shown that the greatest floor loss occurs when the transmitter and receiver are separated by a single floor. Typically, the floor loss is 15–20 dB for one floor and an additional 6–10 dB per floor up to a separation of four floors. For five or more floors of separation, the overall floor loss will increase only a few decibels for each additional floor. This effect is thought to be caused by signals diffracting up the sides of the building and signals scattering off the neighboring buildings. Also important for the deployment of indoor wireless systems is the building penetration loss. This loss depends on the frequency and height of the building. Turkmani et. al. [256] have shown that the building penetration losses decrease with increasing frequency, in particular they are 16.4, 11.6, and 7.6 dB at 441 MHz, 896.5 MHz, and 1,400 MHz, respectively. In general, the building penetration loss for signals propagating into a building tends to decrease with height, the reason being that an LoS path is more likely to exist at increased height. The building penetration loss decreases by about 2 dB per floor from ground level up to about 9–15 floors and then increases again [271]. Windows also have a significant effect on penetration loss. Plate glass provides an attenuation of about 6 dB, while lead-lined glass provides an attenuation anywhere from 3 to 30 dB.

Appendix 1: COST 207 Channel Models

Teh COST 207 study has specified typical realizations for the power-delay profile in the following environments: typical urban (TU), bad urban (BA), reduced TU, reduced BU, rural area (RA), and Hilly Terrain (HT) [64]. The models below are identical to the COST 207 models, except that fractional powers have been normalized so as to sum to unity, that is, the envelope power is normalized to unity.

Table 2.5 COST 207 typical urban (TU) ($\sigma_\tau = 1.0\,\mu$s) and bad urban (BU) ($\sigma_\tau = 2.5\,\mu$s) power-delay profiles, from [64]

Delay μs	Typical urban fractional power	Doppler category	Delay μs	Bad urban fractional power	Doppler category
0.0	0.092	CLASS	0.0	0.033	CLASS
0.1	0.115	CLASS	0.1	0.089	CLASS
0.3	0.231	CLASS	0.3	0.141	CLASS
0.5	0.127	CLASS	0.7	0.194	GAUS1
0.8	0.115	GAUS1	1.6	0.114	GAUS1
1.1	0.074	GAUS1	2.2	0.052	GAUS2
1.3	0.046	GAUS1	3.1	0.035	GAUS2
1.7	0.074	GAUS1	5.0	0.140	GAUS2
2.3	0.051	GAUS2	6.0	0.136	GAUS2
3.1	0.032	GAUS2	7.2	0.041	GAUS2
3.2	0.018	GAUS2	8.1	0.019	GAUS2
5.0	0.025	GAUS2	10.0	0.006	GAUS2

Table 2.6 COST 207 reduced typical urban (TU) ($\sigma_\tau = 1.0\,\mu$s) and reduced bad urban (BU) ($\sigma_\tau = 2.5\,\mu$s) power-delay profiles, from [64]

Delay μs	Typical urban fractional power	Doppler category	Delay μs	Bad urban fractional power	Doppler category
0.0	0.189	CLASS	0.0	0.164	CLASS
0.2	0.379	CLASS	0.3	0.293	CLASS
0.5	0.239	CLASS	1.0	0.147	GAUS1
1.6	0.095	GAUS1	1.6	0.094	GAUS1
2.3	0.061	GAUS2	5.0	0.185	GAUS2
5.0	0.037	GAUS2	6.6	0.117	GAUS2

Table 2.7 COST 207 typical rural (non-hilly) area (RA) power-delay profile ($\sigma_\tau = 0.1\,\mu$s), from [64]

Delay μs	Fractional power	Doppler category
0.0	0.602	RICE
0.1	0.241	CLASS
0.2	0.096	CLASS
0.3	0.036	CLASS
0.4	0.018	CLASS
0.5	0.006	CLASS

Appendix 2: COST 259 Channel Models

The 3GPP standards group has defined three typical realizations for the COST 259 models: typical urban (TUx), rural area (RAx), and hilly terrain (HTx), where x is the MS speed in km/h, [91]. Default speeds are 3, 50, and 120 km/h for the TUx model, 120 and 250 km/h for the RAx model, and 120 km/h for the HTx model.

Table 2.8 COST 207 typical hilly terrain (HT) power-delay profile ($\sigma_\tau = 5.0\,\mu\text{s}$), from [64]

Delay μs	Fractional power	Doppler category
0.0	0.026	CLASS
0.1	0.042	CLASS
0.3	0.066	CLASS
0.5	0.105	CLASS
0.7	0.263	GAUS1
1.0	0.263	GAUS1
1.3	0.105	GAUS1
15.0	0.042	GAUS2
15.2	0.034	GAUS2
15.7	0.026	GAUS2
17.2	0.016	GAUS2
20.0	0.011	GAUS2

Table 2.9 COST 207 reduced hilly terrain (HT) power-delay profile ($\sigma_\tau = 5.0\,\mu\text{s}$), from [64]

Delay μs	Fractional power	Doppler category
0.0	0.413	CLASS
0.1	0.293	CLASS
0.3	0.145	CLASS
0.5	0.074	CLASS
15.0	0.066	GAUS2
17.2	0.008	GAUS2

Appendix 3: Derivation of Equation (2.297)

This Appendix derives an expression for the second moment of a Ricean random variable in terms of its first moment. A Ricean random variable X has probability density function, cf., (2.53)

$$p_X(x) = \frac{x}{b_0} \exp\left\{-\frac{x^2+s^2}{2b_0}\right\} I_0\left(\frac{xs}{b_0}\right) \quad x>0 \qquad (2.352)$$

and moments [217]

$$E[X^n] = (2b_0)^{\frac{n}{2}} \exp\left\{-\frac{s^2}{2b_0}\right\} \Gamma\left((2+n)/2\right) {}_1F_1\left(\frac{n+2}{2},1;\frac{s^2}{2b_0}\right), \qquad (2.353)$$

where $\Gamma(\cdot)$ is the Gamma function, and ${}_1F_1(a,\,b;\,x)$ is the confluent hypergeometric function. The first moment of X is

$$E[X] \equiv \Omega_v = (2b_0)^{\frac{1}{2}} e^{-K} \frac{\sqrt{\pi}}{2} {}_1F_1(3/2,1;K), \qquad (2.354)$$

Table 2.10 COST 259 typical urban (TU*x*) channel model, from [91]

Delay μs	Fractional power	Doppler category
0.000	0.26915	CLASS
0.217	0.17378	CLASS
0.512	0.09772	CLASS
0.514	0.09550	CLASS
0.517	0.09550	CLASS
0.674	0.07079	CLASS
0.882	0.04571	CLASS
1.230	0.02344	CLASS
1.287	0.02042	CLASS
1.311	0.01950	CLASS
1.349	0.01820	CLASS
1.533	0.01259	CLASS
1.535	0.01259	CLASS
1.622	0.01047	CLASS
1.818	0.00708	CLASS
1.836	0.00692	CLASS
1.884	0.00617	CLASS
1.943	0.00550	CLASS
2.048	0.00447	CLASS
2.140	0.00372	CLASS

Table 2.11 COST 259 rural area (RA*x*) channel model, from [91]

Delay μs	Fractional power	Doppler category
0.000	0.30200	Direct Path, $f_0 = 0.7 f_{\mathrm{m}}$
0.042	0.22909	CLASS
0.101	0.14454	CLASS
0.129	0.11749	CLASS
0.149	0.10000	CLASS
0.245	0.04898	CLASS
0.312	0.02951	CLASS
0.410	0.01413	CLASS
0.469	0.00912	CLASS
0.528	0.00575	CLASS

where $K = s^2/2b_0$ is the Rice factor. The second moment of X is

$$\mathrm{E}[X^2] \equiv \Omega_{\mathrm{p}} = 2b_0 \mathrm{e}^{-K} \,_1\mathrm{F}_1(2,1;K)$$

$$= 2b_0(K+1). \tag{2.355}$$

Substituting $2b_0$ from (2.354) into (2.355) gives

$$\Omega_{\mathrm{p}} = \frac{4\mathrm{e}^{2K}\,(K+1)}{\pi \,_1\mathrm{F}_1^2(3/2,1;K)} \; \Omega_v^2 = C(K)\,\Omega_v^2. \tag{2.356}$$

Note that $C(0) = 4/\pi$, $C(\infty) = 1$, and $4/\pi \leq C(K) \leq 1$ for $0 \leq K \leq \infty$.

Table 2.12 COST 259 hilly terrain (HTx) channel model, from [91]

Delay μs	Fractional power	Doppler category
0.000	0.43652	CLASS
0.356	0.12882	CLASS
0.441	0.09550	CLASS
0.528	0.07079	CLASS
0.546	0.06607	CLASS
0.609	0.05370	CLASS
0.625	0.05012	CLASS
0.842	0.02399	CLASS
0.916	0.01862	CLASS
0.941	0.01698	CLASS
15.000	0.01738	CLASS
16.172	0.00537	CLASS
16.492	0.00389	CLASS
16.876	0.00263	CLASS
16.882	0.00263	CLASS
16.978	0.00240	CLASS
17.615	0.00126	CLASS
17.827	0.00102	CLASS
17.849	0.00100	CLASS
18.016	0.00085	CLASS

Appendix 4: Derivation of Equation (2.314)

From (2.313), the composite distribution for the squared envelope, α_c^2, is

$$
p_{\alpha_c^2}(x) = \int_0^\infty \left(\frac{m}{w}\right)^m \frac{x^{m-1}}{\Gamma(m)} \exp\left\{-\frac{mx}{w}\right\}
$$
$$
\times \frac{1}{\sqrt{2\pi}\xi\,\sigma_\Omega w} \exp\left\{-\frac{(10\log_{10}\{w\} - \mu_{\Omega_{p\,(dB)}})^2}{2\sigma_\Omega^2}\right\} dw, \quad (2.357)
$$

where $\xi = \ln(10)/10$. The mean of the approximate log-normal distribution is

$$
\mu_{(dBm)} = \mathrm{E}[10\log_{10}\{\alpha_c^2\}]
$$
$$
= \int_0^\infty \int_0^\infty 10\log_{10}\{x\} \left(\frac{m}{w}\right)^m \frac{x^{m-1}}{\Gamma(m)} \exp\left\{-\frac{mx}{w}\right\}
$$
$$
\times \frac{1}{\sqrt{2\pi}\xi\,\sigma_\Omega w} \exp\left\{-\frac{(10\log_{10}\{w\} - \mu_{\Omega_{p\,(dB)}})^2}{2\sigma_\Omega^2}\right\} dw dx
$$
$$
= \frac{10m^m}{\sqrt{2\pi}\xi\,\sigma_\Omega \Gamma(m)} \int_0^\infty \frac{1}{w^{m+1}} \exp\left\{-\frac{(10\log_{10}\{w\} - \mu_{\Omega_{p\,(dB)}})^2}{2\sigma_\Omega^2}\right\}
$$
$$
\times \int_0^\infty \log_{10}\{x\}\, x^{m-1} \exp\left\{-\frac{mx}{w}\right\} dx\, dw. \quad (2.358)
$$

Assuming that m is an integer, the inner integral becomes [118, 4.352.2]

$$\int_0^\infty \log_{10}\{x\} x^{m-1} \exp\left\{-\frac{mx}{w}\right\} dx = \frac{\Gamma(m)w^m}{m^m \ln 10} \left(\psi(m) - \ln(m/w)\right). \qquad (2.359)$$

Then using the change of variables $x = 10\log_{10}\{w\}$, we obtain

$$\mu_{(\text{dBm})} = \xi^{-1}\left(\psi(m) - \ln(m)\right) + \mu_{\Omega_{\text{p (dB)}}}, \qquad (2.360)$$

where $\psi(\cdot)$ is the Euler psi function, and

$$\psi(m) = -C + \sum_{k=1}^{m-1} \frac{1}{k} \qquad (2.361)$$

and $C \simeq 0.5772$ is Euler's constant. Likewise, the second moment of the approximate log-normal distribution is

$$\mathrm{E}[(10\log_{10}(\alpha_c^2))^2] = \int_0^\infty \int_0^\infty (10\log_{10}\{x\})^2 \left(\frac{m}{w}\right)^m \frac{x^{m-1}}{\Gamma(m)} \exp\left\{-\frac{mx}{w}\right\}$$

$$\times \frac{1}{\sqrt{2\pi}\xi\,\sigma_\Omega w} \exp\left\{-\frac{(10\log_{10}\{w\} - \mu_{\Omega_{\text{p(dB)}}})^2}{2\sigma_\Omega^2}\right\} dw\,dx$$

$$= \frac{m^m}{\sqrt{2\pi}\xi\Gamma(m)} \int_0^\infty \frac{1}{w^{m+1}} \exp\left\{-\frac{(10\log_{10}\{w\} - \mu_{\Omega_{\text{p (dB)}}})^2}{2\sigma_\Omega^2}\right\}$$

$$\times \int_0^\infty (10\log_{10}\{x\})^2 x^{m-1} \exp\left\{-\frac{mx}{w}\right\} dx\,dw. \qquad (2.362)$$

Assuming again that m is an integer, the inner integral is [118, 4.358.2]

$$\int_0^\infty (10\log_{10}(x))^2 x^{m-1} \exp\left\{-\frac{mx}{w}\right\} dx = \frac{(m-1)!w^m}{m^m \ln 10}$$

$$\times \left((\psi(m) - \ln(m/w))^2 + \zeta(2,m)\right)$$

$$(2.363)$$

leading to

$$\mathrm{E}[(10\log_{10}\{\alpha_c^2\})^2] = \zeta^2\left((\psi(m) - \ln(m))^2 \mu_{\Omega_{\text{p (dB)}}}^2 + \zeta(2,m)\right)$$

$$+2\zeta\left(\psi(m) - \ln(m)\right)\mu_{\Omega_{\text{p (dB)}}} + \sigma^2 + \mu_{\Omega_{\text{p (dB)}}}^2, \qquad (2.364)$$

where

$$\zeta(2,m) = \sum_{k=0}^{\infty} \frac{1}{(m+k)^2} \tag{2.365}$$

is Reimann's zeta function. Finally, the variance of the approximate log-normal distribution is

$$\sigma^2 = \mathrm{E}[(10\log_{10}\{\alpha_c^2\})^2] - \mathrm{E}^2[10\log_{10}\{\alpha_c^2\}]$$
$$= \xi^{-2}\zeta(2,m) + \sigma_\Omega^2. \tag{2.366}$$

Problems

2.1. Suppose that $r(t)$ is a wide-sense stationary (WSS) band-pass random process, such that

$$r(t) = g_\mathrm{I}(t)\cos(2\pi f_c t) - g_\mathrm{Q}(t)\sin(2\pi f_c t)$$

(a) Show that the autocorrelation and cross-correlation of $g_\mathrm{I}(t)$ and $g_\mathrm{Q}(t)$ must satisfy the following conditions:

$$\phi_{g_\mathrm{I}g_\mathrm{I}}(\tau) = \phi_{g_\mathrm{Q}g_\mathrm{Q}}(\tau)$$
$$\phi_{g_\mathrm{I}g_\mathrm{Q}}(\tau) = -\phi_{g_\mathrm{Q}g_\mathrm{I}}(\tau)$$

(b) Under the conditions in part (a), show that the autocorrelation of $r(t)$ is

$$\mathrm{E}[r(t)r(t+\tau)] = \phi_{g_\mathrm{I}g_\mathrm{I}}(\tau)\cos(2\pi f_c \tau) - \phi_{g_\mathrm{I}g_\mathrm{Q}}(\tau)\sin(2\pi f_c \tau).$$

2.2. What is the maximum Doppler shift for the GSM mobile cellular system on the "downlink" from the base station to the mobile unit (935–960 MHz RF band)? What is it on the "uplink" direction, or mobile to base (890–915 MHz RF band)? Assume a high-speed train traveling at a speed of $v = 250$ km/h.

2.3. A wireless channel is characterized by the time-variant impulse response

$$g(t,\tau) = \left(1 - \frac{\tau}{T}\right)\cos\left(\Omega t + \phi_0\right), \quad 0 \le \tau \le T,$$

where $T = 0.05$ ms, $\Omega = 10\pi$, and $\phi_0 \in (-\pi, +\pi]$ is a constant.

(a) Determine the channel time-variant transfer function.
(b) Given an input signal having the complex envelope

$$\tilde{s}(t) = \begin{cases} 1, & 0 \le t \le T_s \\ 0, & \text{otherwise} \end{cases},$$

determine the complex envelope of the signal at the output of the channel, $\tilde{r}(t)$. Make sure to consider cases when $0 < T_s < T$ and $0 < T < T_s$, separately.
(c) Consider digital modulation scheme with a modulated symbol interval T_s. If the channel fading is frequency selective, specify the relation between T_s and T.

2.4. Suppose that an omnidirectional antenna is used and the azimuth AoA distribution, $p(\theta)$, is given by (2.48). Find the Doppler power spectrum $S_{gg}(f)$.

2.5. A very useful model for a non-isotropic scattering environment assumes that the azimuth AoA distribution is described by the von Mises pdf in (2.47).

(a) Assuming an isotropic receiver antenna, calculate the received Doppler power spectrum, $S_{gg}(f)$.
(b) Under what conditions are the quadrature components $g_I(t)$ and $g_Q(t)$ uncorrelated?

2.6. Determine and plot the (normalized) power spectral densities $S_{gg}(f)$ for the following cases. Assume 2D isotropic scattering:

(a) A vertical loop antenna in the plane perpendicular to vehicle motion, $G(\theta) = \frac{3}{2}\sin^2(\theta)$.
(b) A vertical loop antenna in the plane of vehicle motion, $G(\theta) = \frac{3}{2}\cos^2(\theta)$.
(c) A directional antenna of beamwidth β directed perpendicular to vehicle motion with (see Fig. 2.57a)

$$G(\theta) = \begin{cases} G_0, & |\frac{\pi}{2} - \theta| < \beta/2 \\ 0, & \text{otherwise} \end{cases}.$$

(d) A directional antenna of beamwidth β directed along vehicle motion with (see Fig. 2.57b)
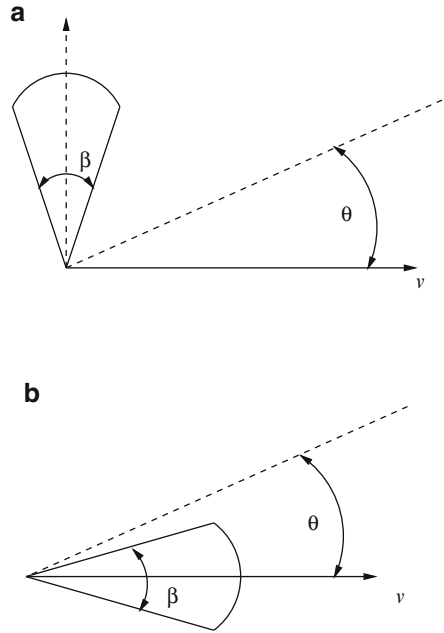
$$G(\theta) = \begin{cases} G_0, & |\theta| < \beta/2 \\ 0, & \text{otherwise} \end{cases}.$$

2.7. Consider a narrow-band channel with a 700 MHz carrier frequency. The complex channel gain at a MS is $g(t) = g_I(t) + jg_Q(t)$, such that

$$S_{g_I g_I}(f) = \begin{cases} \text{rect}\left(\frac{f}{200}\right), & |f| \le 100\,Hz \\ 0, & \text{elsewhere} \end{cases}$$

$$S_{g_I g_Q}(f) = 0.$$

Fig. 2.57 Scenario for
Prob. 2.6 parts (c) and (d)

(a) What is the speed of the mobile station?
(b) What is the cross-correlation function $\phi_{g_I g_Q}(\tau)$ of the I and Q components of the faded envelope?
(c) If antenna diversity is deployed at the mobile station, what are the possible spatial separations between the antenna elements such that the corresponding faded envelopes will be uncorrelated?
(d) Write down an expression for $\phi_{g_Q g_Q}(\tau)$.

2.8. Consider a Ricean fading channel with Rice factor K and average envelope power Ω_p. Assume that the means $m_I(t)$ and $m_Q(t)$ of the in-phase and quadrature components are given by (2.55) and (2.56), respectively. Derive an integral expression for the probability density function of the envelope phase in terms of K and Ω_p.

2.9. Consider a 2D isotropic scattering channel. Show that the psd of the received envelope $\alpha(t) = |g(t)|$ is given by (2.73).

2.10. Consider the non-isotropic scattering environment shown in Fig. 2.7. Show that the continuous portion of the psd of the received envelope $\alpha(t) = |g(t)|$ is given by (2.76).

2.11. Consider a wide-sense stationary zero-mean complex Gaussian random process $g(t)$ having the autocorrelation function $\phi_{gg}(\tau) = \phi_{g_I g_I}(\tau) + j\phi_{g_I g_Q}(\tau)$. Show that the autocorrelation and autocovariance functions of the squared-envelope $\alpha^2(t) = |g(t)|^2$ are given by (2.78) and (2.79), respectively.
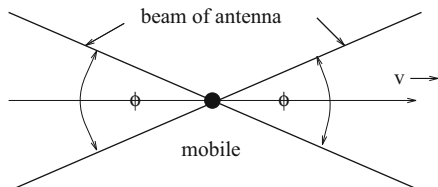
2.12. Consider a wide-sense stationary nonzero-mean complex Gaussian random
process $g(t) = g_I(t) + jg_Q(t)$, where

$$g_I(t) = \hat{g}_I(t) + m_I(t),$$
$$g_Q(t) = \hat{g}_Q(t) + m_Q(t)$$

and $m_I(t)$ and $m_Q(t)$ are the means of $g_I(t)$ and $g_Q(t)$, respectively. Show that
the autocorrelation and autocovariance functions of the squared-envelope $\alpha^2(t) = |g(t)|^2$ are given by (2.83) and (2.86), respectively.

2.13. Establish the equivalence between (2.98) and (2.99).

2.14. A flat Rayleigh fading signal at 6 GHz is received by a vehicle traveling at
80 km/h.

(a) Determine the number of positive-going zero crossings about the rms value that
occur over a 5 s interval.
(b) Determine the average duration of a fade below the rms level.
(c) Determine the average duration of a fade at a level of 20 dB below the rms value.

2.15. Consider a situation where the received envelope is Rayleigh faded ($K = 0$),
but the Doppler power spectrum $S_{gg}^c(f)$ is not symmetrical about $f = 0$, that is,
a form of non-isotropic scattering. Show that the envelope level crossing rate is
given by

$$L_R = \sqrt{\frac{b_2}{b_0} - \frac{b_1^2}{b_0^2}} \cdot \frac{\rho}{\sqrt{\pi}} e^{-\rho^2},$$

where

$$\rho = \frac{R}{\sqrt{\Omega_p}} = \frac{R}{\sqrt{2b_0}}$$

and the b_i are defined in (2.98) with $f_q = 0$.

2.16. Consider the situation in the Fig. 2.58, where the MS uses a directional
antenna with a beam width of $\phi°$. Assume a 2D isotropic scattering environment.

(a) In receiving a radio transmission at 850 MHz, a Doppler frequency of 20–60 Hz is observed. What is the beam width of the MS antenna, and how fast is the MS traveling?
(b) Suppose that the MS antenna has a beam width of 13°. What is the level crossing rate with respect to the rms envelope level, assuming that the MS is traveling at a speed of 30 km/h?

2.17. A vehicle experiences 2D isotropic scattering and receives a Rayleigh faded 900 MHz signal while traveling at a constant velocity for 10 s. Assume that the local mean remains constant during travel, and the average duration of fades 10 dB below the rms envelope level is 1 ms.

(a) How far does the vehicle travel during the 10 s interval?
(b) How many fades is the envelope expected to undergo that are 10 dB below the rms envelope level during the 10 s interval?

2.18. A vehicle receives a Ricean faded signal where the specular component is at the frequency f_c and scatter component is due to 2D isotropic scattering.

(a) Compute the average duration of fades that 10 dB below the rms envelope level for $K = 0, 7, 20$, and a maximum Doppler frequency of $f_m = 20$ Hz.
(b) Suppose that data are transmitted using binary modulation at a rate of 1 Mbps, and an envelope level that is 10 dB below the rms envelope level represents a threshold between "error-free" and "error-prone" conditions. During error-prone conditions, bits are in error half the time. Assuming that the data are transmitted in 10,000-bit packets, how many bits errors (on the average) will each transmitted packet contain?

2.19. Show that for wide-sense stationary (WSS) channels

$$\phi_H(f, m; v, \mu) = \psi_H(f, m; v)\delta(v - \mu),$$
$$\phi_S(\tau, \eta; v, \mu) = \psi_S(\tau, \eta; v)\delta(v - \mu).$$

That is the channel correlation functions $\phi_H(f, m; v, \mu)$ and $\phi_S(\tau, \eta; v, \mu)$ have a singular behavior with respect to the Doppler shift variable. What is the physical interpretation of this property?

2.20. Show that for uncorrelated scattering (US) channels

$$\phi_g(t, s; \tau, \eta) = \psi_g(t, s; \tau)\delta(\eta - \tau),$$
$$\phi_S(\tau, \eta; v, \mu) = \psi_S(\tau; v, \mu)\delta(\eta - \tau).$$

That is the channel correlation functions $\phi_g(t, s; \tau, \eta)$ and $\phi_S(\tau, \eta; v, \mu)$ have a singular behavior with respect to the time delay variable. What is the physical interpretation of this property?

2.21. Given the channel input signal $\tilde{s}(t)$ and the channel delay-Doppler spread function $S(\tau, \nu)$, show that the channel output signal is

$$\tilde{r}(t) = \int_{-\infty}^{\infty} \int_{-\infty}^{\infty} \tilde{s}(t-\tau) S(\tau, \nu) e^{-j2\pi f\tau} \, d\nu \, d\tau.$$

How do you interpret the channel function $H(\tau, \nu)$?

2.22. Suppose that the spaced-time spaced-frequency correlation function of a WSSUS channel has the following form:

$$\phi_T(\Delta f; \Delta t) = \exp\{-b|\Delta t|\} \frac{1}{a + j2\pi\Delta f}.$$

(a) Find the corresponding channel correlation function $\psi_g(\Delta t; \tau)$.
(b) Find the corresponding scattering function $\psi_S(\nu; \tau)$.
(c) What is the average delay spread, μ_τ, and rms delay spread σ_τ?

2.23. The scattering function for a WSSUS scattering channel is given by the following:

$$\psi_S(\tau, \nu) = \Omega_p \cdot \frac{2a}{a^2 + (2\pi\nu)^2} \cdot be^{-b\tau} u(\tau).$$

(a) What is the spaced-time spaced-frequency correlation function?
(b) What is the average delay?
(c) What is the rms delay spread?

2.24. Consider a linear time-invariant channel consisting of two equal rays

$$g(t, \tau) = \delta(\tau) + \delta(\tau - \tau_1).$$

(a) Derive an expression for magnitude response of the channel $|T(f,t)|$ and sketch showing all important points.
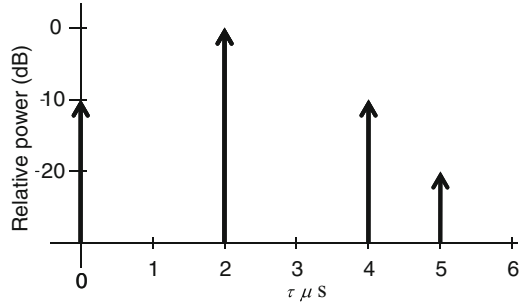(b) Repeat for the phase response of the channel $\angle T(f,t)$.

2.25. The power delay profile of a WSSUS channel is given by

$$\phi_g(\tau) = e^{-\tau/T}, \quad \tau \geq 0.$$

Assuming that $T = 10\,\mu s$, determine

(a) The average delay
(b) The rms delay spread
(c) The coherence bandwidth of the channel

Fig. 2.59 Power delay
profile for Prob. 2.27

2.26. The power delay profile of a WSSUS channel is given by

$$\phi_g(\tau) = \begin{cases} 0.5[1+\cos(2\pi\tau/T)], & 0 \le \tau \le T/2 \\ 0, & \text{otherwise} \end{cases}.$$

(a) Find the channel frequency correlation function.
(b) Calculate the mean delay, the multipath delay spread, and the coherence
    bandwidth.
(c) If $T = 0.1$ ms, determine whether the channel exhibits frequency-selective
    fading to the GSM system.

2.27. Consider the power delay profile shown in Fig. 2.59. Calculate the
following:

(a) Mean delay
(b) rms delay spread
(c) If the modulated symbol duration is $40\,\mu$s, is the channel frequency selective?
    Why

2.28. Consider a WSSUS channel with scattering function

$$\psi_S(\tau, v) = \psi_1(\tau) \cdot \psi_2(v),$$

where

$$\psi_1(\tau) = \begin{cases} 1, & 0 \le \tau \le 100\,\text{ms} \\ 0, & \text{otherwise} \end{cases}$$

$$\psi_2(v) = \begin{cases} \frac{1}{f_m}[1-(v/f_m)^2], & 0 \le |v| \le f_m \\ 0, & \text{otherwise} \end{cases}.$$

Assume $f_m = 10\,\text{Hz}$. Find:

(a) The delay psd
(b) The Doppler power spectrum
(c) The mean delay and the rms delay spread
(d) The maximum Doppler frequency, the mean Doppler frequency, the rms Doppler frequency
(e) The coherence bandwidth and the coherence time of the channel

2.29. Consider the COST-207 TU and BU power delay profiles shown in Fig. 2.42 of the text with delays and fractional powers given in Table 2.5.

(a) Calculate the average delay, μ_τ
(b) Calculate the rms delay spread, σ_τ
(c) Calculate the approximate values of W_{50} and W_{90}
(d) If the channel is to be used with a modulation that requires an equalizer whenever the symbol duration $T < 10\sigma_\tau$, determine the maximum symbol rate that can be supported without requiring an equalizer

2.30. The scattering function $\psi_S(\tau, v)$ for a multipath fading channel is nonzero for the range of values $0 \le \tau \le 1\,\mu\text{s}$ and $-40 \le \lambda \le 40\,\text{Hz}$. Furthermore, $\psi_S(\tau, v)$ is uniform in the two variables τ and v.

(a) Find numerical values for the following parameters:

  • The average delay, μ_τ, and rms delay spread, σ_τ.
  • The Doppler spread, B_d
  • The approximate coherence time, T_c
  • The approximate coherence bandwidth, B_c

(b) Given the answers in part (a), what does it mean when the channel is:

  • Frequency-nonselective
  • Slowly fading
  • Frequency-selective

2.31. Suppose that a fading simulator is constructed by low-pass filtering white Gaussian noise as shown in Fig. 2.31. Assume that the white Gaussian noise generators that produce $g_I(t)$ and $g_Q(t)$ are uncorrelated and have power density spectrum $\Omega_p/2\,\text{W/Hz}$. The low-pass filters that are used have the transfer function

$$H(f) = \frac{A}{1 + j2\pi\beta f}.$$

(a) What is the Doppler power spectrum $S_{gg}(f)$ and autocorrelation function $\phi_{gg}(\tau)$?
(b) Find A such that the envelope power is equal to Ω_p.
(c) What is the joint probability density function of the output $g(t)$ and $g(t + \tau)$?

2.32. Suppose that a fading simulator is constructed using low-pass filtered white Gaussian noise as shown in Fig. 2.31. Assume that the white Gaussian noise generators that produce $g_I(t)$ and $g_Q(t)$ are uncorrelated. The low-pass filters that are used have the transfer function

$$H(f) = \frac{1}{\sqrt{B}} \text{rect}\left(\frac{f}{B}\right).$$

(a) What is the Doppler power spectrum $S_{gg}(f)$?
(b) For the $S_{gg}(f)$ in part (a), derive an expression for the envelope level crossing rate.

2.33. Consider Jakes' method in (2.228) and (2.229).

(a) With the choice that $\alpha = 0$ and $\beta_n = \pi n/(M+1)$ show that

$$< g_I(t)g_Q(t) > = 0$$
$$< g_Q^2(t) > = (M+1)/(2M+1)$$
$$< g_I^2(t) > = M/(2M+1).$$

(b) Rederive the time averages in part (a) for the choice $\alpha = 0$ and $\beta_n = \pi n/M$.

2.34. (**Computer exercise**) You are to write a software fading simulator that uses Jakes' method and plot typical sample functions of the faded envelope. By scaling $g_I(t)$ and $g_Q(t)$ appropriately, generate a Rayleigh faded envelope having the mean-squared envelope $\Omega_p = 1$. Plot a sample function of your faded envelope assuming a maximum Doppler frequency of $f_m T = 0.1$, where T is the simulation step size.

Note that Jakes' simulator is nonstationary. Therefore, you may not necessary get a plot that is identical to Fig. 2.34. In fact, it would be good if you could observe the nonstationary behavior of the simulator, that is, the pdf of the envelope distribution changes with time.

2.35. (**Computer exercise**) In this problem you are to generate a Ricean faded envelope $\hat{g}(t) = \hat{g}_I(t) + j\hat{g}_Q(t)$ by making appropriate modifications to Jakes' method such that

$$\hat{g}_I(t) = m_I(t) + g_I(t),$$
$$\hat{g}_Q(t) = m_Q(t) + g_Q(t),$$

where $g_I(t)$ and $g_Q(t)$ are defined in (2.228) and (2.229), respectively. Assume that the means $m_I(t)$ and $m_Q(t)$ are generated according to Aulin's model in (2.55) and (2.56). For $f_m T = 0.1$, $\Omega_p = 1$ and $K = 0, 4, 7$, and 16, plot the following:

(a) The envelope $\hat{\alpha}(t) = \sqrt{\hat{g}_I^2(t) + \hat{g}_Q^2(t)}$
(b) The wrapped phase $\phi(t) = \text{Tan}^{-1}\left(\hat{g}_Q(t)/\hat{g}_I(t)\right)$, mod 2π

2.36. (**Computer exercise**) This problem uses the fading simulator you developed in Problem 2.35. We now want to compute an estimate of the mean-squared envelope $\Omega_p = \mathrm{E}[\hat{\alpha}^2(t)]$ from samples of $\hat{g}_I(kT)$ and $\hat{g}_Q(kT)$, where T is the sample spacing in seconds. The estimate is computed by forming the empirical average

$$\hat{\Omega}_p = \frac{1}{N} \sum_{i=1}^{N} \left(\hat{g}_I^2(iT) + \hat{g}_Q^2(iT) \right),$$

where NT is the window averaging length in seconds. Assuming a constant velocity, the distance MS moves (in units of wavelengths) in a time of NT seconds is

$$\frac{d}{\lambda_c} = N f_m T.$$

(a) For $K = 0, 4, 7$, and 16, generate 1,000 estimates of the of Ω_p using non-overlapping averaging windows of size $N = 50, 100, 150, 200, 250, 300$. Construct a graph that plots, for each K, the sample variance of the Ω_p estimate on the ordinate and the window size on the abscissa.
(b) Can you draw any qualitative conclusions from part (a)?

Note: Estimates of the local mean Ω_p are used in resource management algorithms such as handoff algorithms.

2.37. Suppose that we have available two complex faded envelopes $g_i(t) = g_i^I(t) + jg_i^Q(t)$, $i = 1, 2$, such that

$$\mu_\mathbf{g} = \mathrm{E}[\mathbf{g}(t)] = \mathbf{0},$$

$$\Phi_\mathbf{g}(\tau) = \frac{1}{2}\mathrm{E}[\mathbf{g}(t)\mathbf{g}^H(t+\tau)] = \Omega J_0(2\pi f_m \tau),$$

where

$$\mathbf{g}(t) = (g_1(t), g_2(t)),$$

$$\Omega = \begin{bmatrix} \Omega_1 & 0 \\ 0 & \Omega_2 \end{bmatrix}.$$

We now generate a third faded envelope $g_3(t)$ that is correlated with $g_1(t)$ and $g_2(t)$ according to

$$g_3(t) = \alpha g_1(t) + (1 - \alpha)g_2(t), \qquad 0 \le \alpha \le 1.$$

(a) Compute the values of

$$\phi_{g_1 g_3}(\tau) = \frac{1}{2}E[g_1(t)g_3^*(t+\tau)],$$

$$\phi_{g_2 g_3}(\tau) = \frac{1}{2}E[g_2(t)g_3^*(t+\tau)],$$

$$\phi_{g_3 g_3}(\tau) = \frac{1}{2}E[g_3(t)g_3^*(t+\tau)].$$

(b) What is the envelope distribution of $g_3(t)$?

2.38. Suppose that the two $\tau = T/4$ spaced taps in Example 2.1 do not have equal magnitude. In particular, suppose that $|g_0(t)|^2 = |g_1(t)|^2/2$. Once again, we wish to generate a T-spaced channel model such that the two T-spaced taps capture the maximum possible total energy.

(a) Find the optimal sampler timing instant
(b) Determine the corresponding matrix **A** for $\beta = 0.35$

2.39. By starting with the Gaussian density for the local mean envelope power in (2.296), derive the log-normal density in (2.292).

2.40. (**Computer exercise**) In this problem we want to generate variations in the local mean Ω_p due to shadowing. The shadows are generated according to the state equation in (2.299).

(a) Suppose that the simulation step size is $T = 0.1$ s and the MS velocity is $v = 30$ km/h. We want a shadow decorrelation of 0.1 at a distance of 30 m. Find ζ.
(b) Using the value of ζ obtained in part (a) and a shadow standard deviation of $\sigma_\Omega = 8$ dB, plot a graph of $\Omega_{p \text{ (dB)}}$ against the *distance* traveled. Scale your plot so the distance traveled goes from 0 to 100 m.

2.41. The measured path loss at a distance of 10 km in the city of Tokyo is 160 dB. The test parameters used in the experiment were the following:

- BS antenna height $h_b = 30$ m
- MS antenna height $h_m = 3$ m
- Carrier frequency $f_c = 1,000$ MHz
- Isotropic BS and MS antennas

Compare the measured path loss with the predicted path loss from Okumura and Hata's model and Lee's model.
Note: If any model parameters are undefined, then use the default values.

2.42. Suppose that the received power from a transmitter at the input to a receiver is 1 microwatt at a distance of 1 km. Find the predicted power at the input to the same receiver (in dBm) at distances of 2, 3, and 5 km from the transmitter for the following path loss models:
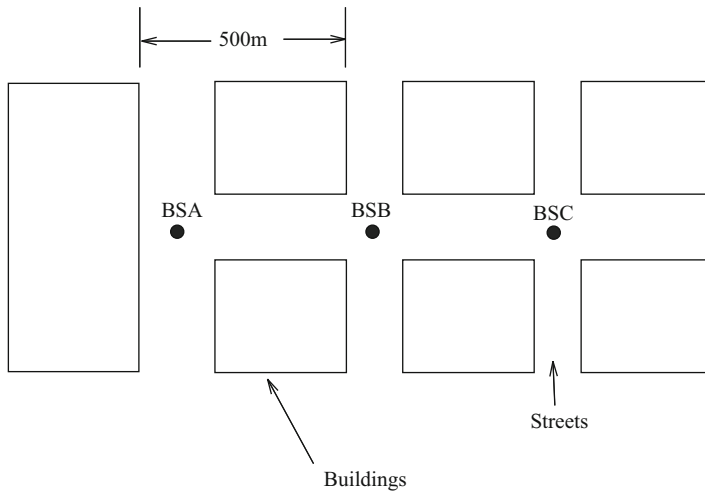
Fig. 2.60 Base station and street layout for Prob. 2.43

(a) Free space
(b) 2-ray ground reflection
(c) Model described by

$$\mu_{\Omega_{\text{p (dBm)}}}(d) = \mu_{\Omega_{\text{p (dBm)}}}(d_o) - 10\beta \log_{10}(d/d_o) \quad \text{(dBm)}$$

where $\beta = 3.5$
(d) COST231–Hata model (medium city)

In all cases assume that $f_c = 1,800\,\text{MHz}$, $h_b = 40\,\text{m}$, $h_m = 3\,\text{m}$, $G_T = G_R = 0\,\text{dB}$. Tabulate your results.

2.43. Consider Fig. 2.60 and the following data:

- The symbol transmission rate is 24,300 symbols/s with 2 bits/symbol
- The channel bandwidth is 30 kHz
- The propagation environment is characterized by an rms delay spread of $\sigma_\tau = 1\,\text{ns}$

An MS is moving from base station A (BSA) to base station B (BSB). Base station C (BSC) is a co-channel base station with BSA.

Explain how you would construct a computer simulator to model the received signal power at the MS from (BSA) and (BSC), as the MS moves from BSA to BSB. Clearly state your assumptions and explain the relationship between the propagation characteristics in your model.

Principles of Mobile Communication
Stüber, G.L.
2012, XXII, 797 p. 358 illus., Hardcover
ISBN: 978-1-4614-0363-0